University of Southampton

Faculty of Natural and Environmental Sciences
School of Ocean and Earth Sciences
National Oceanography Centre Southampton

A combined laboratory and modelling analysis of the evolution of fluid overpressure and fluid escape structures in the Mediterranean Salt Giant Basin

by

Michael Stanley Dale

ORCID ID [0000-0002-5890-2627]

Thesis for the degree of Doctor of Philosophy

[April, 2023]

This thesis is dedicated to my wife Naima,
daughter Anabella, and son Noah.
Thank you for your years of support,
from commencement to completion
of this highly enjoyable PhD

University of Southampton

Abstract

Faculty of Natural and Environmental Sciences
School of Ocean and Earth Science
National Oceanography Centre Southampton
Doctor of Philosophy

A combined laboratory and modelling analysis of the evolution of fluid overpressure and fluid escape structures in the Mediterranean Salt Giant Basin

by

Michael Stanley Dale

The Messinian Salinity Crisis (5.97 to 5.33 Ma) led to rapid deposition and loading of thick evaporite units below what is now the Mediterranean Sea. Observations of large-scale methane venting, visible in the form of eruptive pockmark features in the paleo-seabed topography, indicate that high pore fluid overpressures were generated during that period fracturing the sediments, including the evaporites, of the Mediterranean basin. In this thesis, I present a quantitative assessment that links sea level fall, salt deposition, fluid overpressure development, and generation of fluid escape structures in the Mediterranean Salt Giant Basin. This thesis is divided into three scientific studies: (i) overpressure development from basin inception to present-day for basin-centre and marginal basins in the Western Mediterranean, (ii) quantification of gas overpressure and sea-level fall that triggered a possible fluid escape at the onset of the Messinian Salinity Crisis (MSC) in the Eastern Mediterranean, and (iii) laboratory investigation of effective pressure controls on the elastic and hydromechanical properties relations in evaporites. These studies use new data for evaporites from laboratory experiments performed in this thesis including permeability measurements from pore pressure transmission (PPT), mercury injection porosimetry, elastic wave and resistivity measurements in brine injection experiments, and 3-D X-Ray micro-CT (XCT) imaging.

Evaporites have long been recognised as impermeable seals that create some of the world's highest subsalt reservoir pressures. However, studies show that salts can retain open pore spaces and connected pore-fluid pathways. To reduce uncertainty on fluid properties of evaporites and increase the predictive ability of overpressure models applied to salt basins, I undertook laboratory measurements of evaporite properties (density, porosity and permeability) on seven high quality, high purity, and intact, and two fractured salt rock core sample covering Pre-Cambrian to Miocene evaporite basins across the globe (Pakistan, Tunguska Basin, Russia, NW Lancashire, UK, Sicily, Italy). These properties were measured for confining pressure ranging from 5 to 50 MPa, representing shallow and deep loading states of stress, equivalent to ~236 to 2395 m below ground. The results for intact salt rock show low absolute porosity below 1.2 %, permeability strongly influenced by stress state, and permeability below 10^{-20} m^2 once cracks close.

Fluid overpressure modelling is applied in the Liguro-Provençal and Algero-Balearic basins of the Western Mediterranean, and the Levant Basin of the Eastern Mediterranean. For the Western Mediterranean, I show that rapid sediment loading of low permeability evaporites from the MSC generated high overpressure up to 11.2 MPa within the evaporites and throughout pre-Messinian sequences. The high overpressure within the evaporites would have been sufficient to hydro fracture them and generate vertical fluid release features. The connection between the formation of the observed pockmarks in the Eastern Mediterranean and gas overpressure is uncertain. Hence, I test if the large crater pockmarks observed at the base of the Messinian evaporites may have been caused by fluid migration from methane gas accumulates in Miocene sediment towards the seafloor, triggered by sea-level drop at the beginning of the MSC. Our results show that the pockmarks were most likely caused by tensile fracturing of shallow Miocene sediment and subsequent gas migration when sea-level fell between 50 to 400 m, compatible with the observed enhanced erosion observed in the deep water canyons of the Levant margin. At a basin scale, this discharge of gas may have led to major emissions into the atmosphere.

The presence of structural discontinuities is an important factor that may lead to uncontrolled dissolution events during caverning, important for underground hydrogen (energy) storage (UHS) in salt formations. I designed laboratory based dissolution tests on intact and fractured salt rock to demonstrate with geophysical signature that even small structural discontinuities may significantly impact the dissolution patterns. Our results show that pre-existing fractures can give rise to rapid dissolution irrespective of fluid pore pressure or confining pressure.

.

Abstract

Contents

List of Tables

List of Figures

Research Thesis: Declaration of Authorship

Print name: Michael Stanley Dale

Title of thesis: A combined laboratory and modelling analysis of the evolution of fluid overpressure and fluid escape structures in the Mediterranean Salt Giant Basin

I declare that this thesis and the work presented in it are my own and has been generated by me as the result of my own original research.

I confirm that:

1. This work was done wholly or mainly while in candidature for a research degree at this University;
2. Where any part of this thesis has previously been submitted for a degree or any other qualification at this University or any other institution, this has been clearly stated;
3. Where I have consulted the published work of others, this is always clearly attributed;
4. Where I have quoted from the work of others, the source is always given. With the exception of such quotations, this thesis is entirely my own work;
5. I have acknowledged all main sources of help;
6. Where the thesis is based on work done by myself jointly with others, I have made clear exactly what was done by others and what I have contributed myself;
7. Parts of this work have been published as: -

Dale, M. S., Marín-Moreno, H., Falcon-Suarez, I. H., Grattoni, C., Bull, J. M., & McNeill, L. C. (2021). The Messinian Salinity Crisis as a trigger for high pore pressure development in the Western Mediterranean. Basin Research, 33(4), 2202-2228. doi:https://doi.org/10.1111/bre.12554

Dale, M.S., Falcon-Suarez, I.H., Marín-Moreno, H., 2021a. Geophysical response to dissolution of undisturbed and fractured evaporite rock during brine flow, EGU General Assembly 2021, online, pp. EGU21-15572.

Signature: .... Date: ....

Research Thesis: COVID impact

The global pandemic greatly impacted my research during the period from March 2020 to March 2021. The beginning of my PhD research was positive, from commencement of research on the 16th October 2018 and thereafter for the following 17 months when I met with my supervisors and gained opportunities to attend technical training courses on Geology of the Mediterranean in Palermo and Trieste, Italy and Salamanca, Spain. From March 2020 life and research changed with England entering 3 national lockdowns in under a year that affected both my family and research. During this time my family and I were thrust into a situation of multiple lockdowns, primary schools and nurseries were shut-down, National Oceanography Centre (NOC)/ University of Southampton buildings closed, conferences cancelled, and the impacts of the recommendation to work from home while raising and home-schooling both my 18-month old son and 7 years old daughter. All of this disrupted my research, online meetings, and quality of life. Added to this was the disruption to laboratory testing and planned secondments (required as part of the Marie Curie programme in my PhD as part of my research. Initially, secondments were planned at the Istituto Nazionale di Oceanografia e di Geofisica Sperimentale (OGS) in Trieste, Italy and Volcanic Basin Petroleum Research Centre, Norway, to study various topics on the Mediterranean using confidential datasets from those institutions. Once lockdowns commenced in the UK, these secondments (e.g., OGS 3-month secondment from April 2020) were cancelled. To manage this, I approached supervisors working on the Mediterranean from the University of Oxford who fortunately were willing to undertake an online secondment, discuss and plan a new research topic and gain permission to use confidential data remotely. Here, to contact a new institution and formulate and progress a new topic and perform this online took considerably more time. Regarding laboratory work, the laboratory at NOC was initially closed during the start of COVID-19. When open, the laboratory operated on a restricted basis, giving priority to people with imminent deadlines, and I was unfortunately not one of these people. Here, initial concept testing, sample preparation, understanding of rig equipment and extended testing were all undertaken during restricted (sporadic days and weeks) time periods.

Acknowledgements

This PhD was supported by funding from the European Union's Horizon 2020 research and innovation programme under the Marie Skłodowska-Curie grant agreement No 765256. The PhD sits within work package #3 on drilling hazards with aim 'to develop a mechanistic and quantitative understanding of early salt deformation and sub-salt overpressure development that can be used by the oil industry to mitigate the risks associated with drilling in salt-capped hydrocarbon provinces'. Work package 3 includes projects by Early Stage Researcher's (ESR) on Mediterranean Salt Structures (ESR 10), Salt Tectonics in the Levantine Basin (ESR 11), Overpressure development in rapidly deposited salt basins (ESR 12; this study), and Analogue modelling of combined crustal and Messinian salt deformation in Mediterranean (ESR 13).

From the University of Southampton and National Oceanography Centre, I would like to thank my supervisory team Dr Hector Marin-Moreno, Dr Ismael Himar Falcon-Suarez, Professor Jonathan Bull and Professor Lisa McNeill, and panel chair Professor Tim Henstock.

I thank the Earth Science Department at Oxford University for hosting the primary author during his secondment. I thank the Bremen Core Repository, the Knauf Group, Italkali S.p.A. and ICL Boulby for providing evaporite core samples for experimental testing. I also thank the Instituto Nazionale di Oceanografia e di Geofisica Sperimentale and GALSI S.p.A for providing access to seismic reflection data on the Western Mediterranean.

Chapter 1 Introduction

1.1 Rational – Overpressure in evaporite basins

Evaporites are one of the worlds most effective sedimentary seals for trapping of hydrocarbon deposits and also artificially for storage of gas in salt caverns. Drilling through and around salt structures can pose significant risks to safety primarily from the wide ranges of stress and overpressure conditions that may exist (Dusseault, et al., 2004). In the Mediterranean during the Messinian Salinity Crisis (MSC; 5.97 to 5.33 Ma), dramatic climatic changes and isolation from the Atlantic Ocean from ~5.97 led to desiccation of the Mediterranean Basin and formation of a Salt Giant deposit >2000 m thick (Roveri et al., 2014). As a consequence of uncertainties in stress, overpressure and borehole instability, few boreholes have intersected and drilled below the MSC in search of hydrocarbon and to better understand the evolution of this geological system. Supporting these concerns, occurrences of gas in salt mines also show that evaporites such as salt rock can retain fluid within the pores with fluid pressure capable of increasing to lithostatic pressures (Ehgartner et al., 1998). In this thesis, I attempt to better understand the impact of the MSC, with significant sea-level falls and evaporite deposition, on overpressure formation and fluid flow across Western and Eastern Mediterranean Basins.

Halite, also known as Salt rock, is composed of Sodium Chloride (NaCl). Halite has a cubic crystal shape, and can be found in massive granular or fibrous habit (Gevantman, et al., 1981). Evaporites are rocks precipitated from saturated brine driven by solar evaporation (White, et al., 2018). Evaporite salts such as anhydrite, carnallite, gypsum and sylvite precipitate later during saline stages of higher brine concentration (White, et al., 2018). Halite displays low permeability, high entry pressure and ductility, making it an effective sedimentary seal (White, et al., 2018). Several studies, including this thesis, indicate salt rock has intact permeabilities in the range of 10^{-21} to 10^{-24} m^2 (Beauheim and Roberts 2002). In comparison, claystone sedimentary seals show permeabilities between 10^{-17} to 10^{-23} m^2 (Neuzil, 1994).

Salt rock has previously been considered as an impermeable barrier to fluid flow (Bertoni, et al., 2015). Assuming a connected pore system existed, these pores would close until the salt is near impermeable and pores are disconnected. However, observed gas release from salt into mines and caverns confirms that salt contains pressurised gas, with pore pressure of this trapped gas in intercrystalline boundaries potentially reaching lithostatic pressures (Ehgartner et al., 1998). Laboratory experiments on salt rock also show that a dilatancy boundary for creep of salt rock exists. If mechanical stresses exceed a critical limit deformation, dilatancy and opening of microcracks can occur (Popp et al., 1998). Here, from the transition of non-dilatant to dilatant deformation, microcracks cause damage to the microstructure and increase permeability of the salt rock (Popp et al., 1998).

Several mechanisms have been proposed for overpressure generation in global sedimentary basins (e.g. Neuzil, 1995; Osborne and Swarbrick 1997; Kumar, 2015) including: undercompaction (disequilibrium compaction), aquathermal expansion, chemical reactions (hydrocarbon generation and mineral transformations), tectonic compression, and lateral transfer.

In this thesis, I deal dominantly with modelling pore fluid overpressure generation in evaporite and clastic rocks due to the disequilibrium compaction mechanism. I also model fluid-related fracturing caused by gas overpressure, due in part to a combination of the presence of a biogenic petroleum system and sea-level fall. Other mechanisms generating overpressure are discussed in this thesis including the dehydration reactions gypsum-anhydrite as well as tectonic compression. The overpressure mechanisms considered are briefly introduced below.

1.1.1 Disequilibrium Compaction

Overpressure due to disequilibrium compaction occurs by an imbalance between increasing compressive stress during sediment burial and ability of the sediment to expel fluid (Tingay et al., 2009). During slow burial (normal compaction) as vertical load increases, pore-volume decreases and pore fluid is expelled from the sediment allowing an equilibrium between overburden and reducing pore-volume to be maintained (Osborne et al., 1997). However, during rapid burial as vertical load increases, if accompanied by fluid that cannot be expelled rapidly, part of the load will be supported by the pore fluid resulting in pore fluid pressure increasing above hydrostatic (a process called disequilibrium compaction; e.g., Osborne et al., 1997). The magnitude and time evolution of overpressure depends on the balance between sediment loading and compressibility, pore fluid dissipation controlled by permeability, and drainage (dissipation) distance.

In this thesis, I evaluate overpressure and hydro fracture of sediment induced by the disequilibrium compaction mechanism in the Liguro-Provençal, Algero-Balearic and Levant basins of the Mediterranean, focused on time evolution of overpressure from Oligocene to present day.

1.1.2 Gypsum to anhydrite dehydration

Overpressure can be caused by fluid expansion from mineral transformations such as smectite dehydration to illite, or in evaporite basins, the gypsum to anhydrite and carnellite to sylivite transition. Gypsum and anhydrite are common sulfate minerals that occur in evaporitic rocks, interrelated by reversible dehydration reactions (Mirwald, 2008). Monoclinic Gypsum ($CaSO_4.2H_2O$) is a hydrous mineral, while orthorhombic anhydrite ($CaSO_4$) is H_2O free (Mirwald, 2008). Due to gypsum to anhydrite conversion, the transition upon burial and heating is potentially accompanied by an increase in rock volume in the subsurface of 18.3 % (Kushnir, 1988), 30-50 % (Pettijohn, 1975), 64.9 % (Gorbunova, 1977), and 30-67 % (Ford, 1989), as described in (Klimchouk,1996). The thermodynamic stability and solubility of gypsum and anhydrite is dependant on Pressure (P) and Temperature (T) (Figure 1).

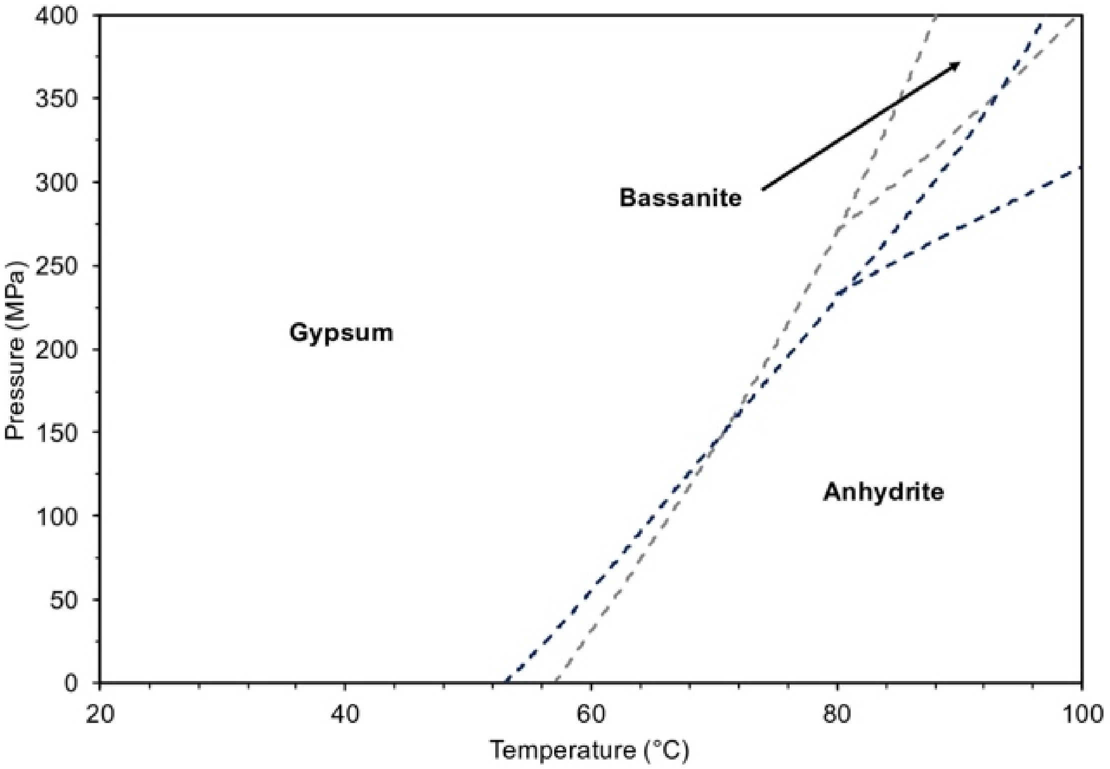

Figure 1: Phase boundaries of gypsum-bassanite-anhydrite with temperature and pressure.

Anhydrite originates primarily due to the dehydration of gypsum and effects of temperature and pressure (Klimchouk,1996). However, other factors contributing to the effect of dehydration are suggested including early diagenesis at shallow depths by interaction with brines of Na, Mg, or Ca chlorides (Klimchouk,1996). Mechanisms and rates of the anhydrite to gypsum conversion also depend on factors of water-bearing properties of surrounding sediment, local and regional flow regimes, and tectonics (e.g., uplift to shallower depths).

In this thesis I evaluate overpressure induced by the gypsum to anhydrite dehydration process at the base of the Emile Baudot Escarpment in the Algero-Balearic basin, based on presence of polygonal faults in upper evaporites of the MSC that suggest possible past fluid expulsion and migration events. To understand if gypsum dehydration occurred here, I evaluate P and T conditions of the Upper Unit Gypsum considering thickness variations of the gypsum and overburden units, and ranges of possible heat flow and thermal conductivity.

1.1.3 Tectonic Compression

Overpressure generated by tectonic activity can occur at local and regional scales by folding and faulting, gravity sliding, movement of plate boundaries, earthquakes, and movement from diapirs of salts and claystone (Chilingar et al. 2002). The magnitude of overpressure generated in tectonically active areas depends on the rate of tectonic strain, which produces a reduction in pore volume (change in porosity) and permeability, and the rate of fluid flow. Salt bodies in particular play an important role in stress and pore pressure, with salt-sediment interactions locally perturbed and patterns of stress and pore pressure varying from different salt flow patterns and driving mechanisms (Luo, G et al., 2017). Thus, understanding and estimating pore pressure in salt basins where a component of tectonic compression exists can be difficult. In addition, activation and opening of faults that act as conduits for fluid migration can also give rise to various pressure changes and hydraulically connect different pressure systems (Luo, et al., 2003).

In this thesis I reduce the impact of compression on our 1-D models in the Western Mediterranean by undertaking our study in areas of laterally extensive horizontal layers. I also consider long-term tectonic compression unlikely in our Eastern Mediterranean study area, considering lack of continued pockmark formation and distance of our modelled pockmark area from faults and folds, as observed on regional seismic data.

1.2 Aims of the PhD

In this thesis I aim to understand one of the largest salt deposits on Earth, that of the Mediterranean Salt Giant. Specifically, the aims of the thesis are to use numerical and analytical modelling, and laboratory experiments to:

1. Understand, quantify and assess the time evolution and role of pore fluid overpressure on the Western Mediterranean.

2. Test if the crater pockmarks observed at the base of the Messinian evaporites may have been caused by fluid migration from overpressured methane gas accumulates in Miocene sediment towards the seafloor, triggered by sea-level drop at the beginning of the Messinian Salinity Crisis (MSC). Aims 1 and 2 use data from laboratory experiments performed in this thesis to constrain input parameters for the modelling.
3. Analyse the hydromechanical properties of salt rocks in general to develop relationships between their elastic and hydromechanical properties. A secondary aim was to investigate the effect of rock heterogeneities on dissolution using geophysical responses.

1.3 Geological setting

1.3.1 Evolution of the Western Mediterranean

During the Late Cretaceous, convergence of the African and Eurasian plates commenced (Olivet, 1996), with convergence of plate boundaries between the northern margin of the African plate and the Iberian Peninsula from the Late Eocene to Early Oligocene (~35 to 30 Ma) (Jolivet et al., 1996). Following subduction of the Tethyan oceanic lithosphere and roll-back of the Apennines-Maghrebides subducting plate towards the north-east, south-east and south, extensional tectonics commenced in back-arc basins around the Eocene to Oligocene boundary (~34 Ma) (Carminati et al., 2011). The roll-back created microplate movements in the Western Mediterranean, developing a clockwise rotation of the Balearic promontory relative to Iberia that opened the Valencia Trough, and a counter-clockwise rotation of Corsica and Sardinia relative to Eurasia, leading to rifting of the Balearic and Ligurian extensional centres (Schettino et al., 2006).

The Liguro-Provencal basin comprises present day areas of the Gulf of Lion, Ligurian Sea and Mediterranean Sea between Corsica and Sardinia to the east of Menorca (Carminati et al., 2011). Continental rifting commenced during the latest Eocene to Early Oligocene with active extension in the oceanic portion of the basin continuing until the late Aquitanian to late Burdigalian (~21 to 16 Ma) (Carminati et al., 2011). The origin and age of the Algerian basin is poorly constrained, with ages from about 25 to 10 Ma proposed (Carminati et al., 2011). One proposal for tectonic evolution of the area is extension terminating in the Liguro-Provençal basin and beginning in the Algerian basin during the Langhian (Mauffret et al., 2004), supported by Alger-1 well chronostratigraphy on the Algerian margin (Burollet et al., 1978).

For all Western Mediterranean basins (excluding the Tyrrhenian basin), basin extension ended by the Late Serravallian to Tortonian (Jolivet et al., 1996).

The onset of the MSC in the Mediterranean basin at 5.97 Ma (CIESM., 2008; Roveri et al., 2014) was initiated by tectonic and glacio-eustatic processes progressively isolating the Mediterranean Sea from the world ocean. During this period, basin water volume decreased, partial desiccation occurred and evaporite minerals were precipitated (Krijgsman et al., 1999; Lozar et al., 2018). MSC events of the Late Miocene are grouped into three stages: Stage 1 (5.97 to 5.6 Ma) is the first evaporitic stage; Stage 2 (5.6 to 5.55 Ma) includes the peak of the crisis and evaporite precipitation in deep depocentres (Roveri et al., 2014); and Stage 3 (5.55 to 5.33 Ma) is the final evaporitic stage and Zanclean flooding (5.33 Ma) - the end of the MSC and return to marine conditions in the Mediterranean basin (Roveri et al., 2014). Since the Pliocene, the Western Mediterranean basin is reconnected to the world ocean through the strait of Gibraltar (Jolivet et al., 1996). During deposition of Messinian and post-Messinian sediment in the Liguro-Provençal basin, gravity sliding, and sediment deformation occurs in the deep basin, caused by differential compaction of overburden in areas of basement structures (Maillard et al., 2003). In the Algero-Balearic basin, gravity sliding and deformation also occur in the deep basin from the late Tortonian to present, coincident with tectonic compression/uplift on the Algerian margin (Mourad et al., 2014).

1.3.2 Evolution of the Levant Basin, Eastern Mediterrranean

The offshore Levant Basin may be described as a polyphase basin, developed from numerous tectono-sedimentological evolution stages (Needham et al., 2017). Early Mesozoic rifting opened the Levant Basin, a remnant of the Neotethys Ocean (Dewey et al., 1973; Robertson and Dixon, 1984). During the Late Early Cretaceous to Eocene, passive thermal subsidence occurred (Bein & Gvirtzman, 1997; Gardosh et al., 2010). From the Mid-Late Cretaceous, the Levant Basin began to close, with intense deformation on the northern margins, associated with the collision of Arabian-African with Eurasia (Ben-Avraham, 1989; Garfunkel, 1998; Robertson, 1998). A second compressional event occurred in the late Paleogene (second stage of Syrian Arc deformation) with further inversion of the Levant Basin (Frizon de Lamotte et al., 2011; Walley, 1998).

The Senonian to Eocene represented a period of non-deposition and erosion on the slope, while submarine canyons developed after the Oligocene, namely the Afiq (Beer-Sheva), El Arish and Ashdod (Palmahim) Canyons (Druckman et al., 1995, Buchbinder and Zilberman, 1997; Fig. 2). The shelf area underwent tectonic uplift during the early Miocene and became intermittently emergent (Buchbinder and Zilberman, 1997); clastic sediment increased (Druckman et al., 1995) and submarine canyons extended to the shelf area through headward erosion (Buchbinder and Zilberman, 1997).

Collision was followed by rifting from the Early Oligocene and Miocene, decoupling marginal and basinal depositional settings leading to deposition of thick Cenozoic units in the Levant basin (in Barabasch et al. (2019) based on Hawie et al., 2015). Increase in salinity and rapid precipitation of a >1 km thick evaporite sequence took place during the MSC (5.97 to 5.33 Ma) at the end of the Miocene (Hsü, et al., 1973; CIESM., 2008; Roveri et al., 2014; Lofi, 2018; Camerlenghi, et al., 2020). Dramatic sea-level falls (up to 2070 m) have been suggested based on lowstand shorelines offshore the Western Desert, Egypt, with the Levant Margin undergoing extensive erosion and canyon incision (Bertoni & Cartwright, 2006; Al-Balushi et al., 2016). Evidence of incised canyons at base-salt also exist in the west Nile Deep Sea Fan and Herodotus Basin (Mousouliotis et al., 2020; Kirkham et al., 2022). In the deep Levant Basin, craters filled by Messinian evaporites exist in the clastic sediments that immediately predate the MSC (Bertoni et al., 2013). In the Plio-Pleistocene, widespread reflooding of the Mediterranean Basin led to reestablishment of marine conditions and deposition of siliciclastic sediments interbedded with marl, chalk, and limestone in the Levant Basin (Nader (2014) taken from Barabasch et al. (2019)).

1.4 Datasets

The evaporite core samples acquired as part of this thesis (Figures 2 & 3) include:

Four gypsum samples of Messinian age were obtained from drillholes DSDP Site 372 and Letymbou-E Let 1, Cyprus in the Eastern and Western Mediterranean. Core samples were evaluated to constrain density (bulk and grain), porosity (connected), and permeability, as input parameters in our modelling of MSC Stage 3 (Upper Unit Gypsum) in the Western Mediterranean.

Ten 'salt rock' core samples were collected for analysis at various stages of study.

1. Three samples of Messinian age were obtained from the Realmonte mine in Sicily. Samples were initially collected to constrain hydrogeological input parameters in our overpressure modelling of MSC Stage 2 (Mobile Unit) in the Western Mediterranean. However, all three samples after coring showed prevalent cracks throughout, providing density (bulk and grain), porosity (connected), and permeability information for

fractured samples only. This dataset was used to guide some of the boundary ranges for sensitivity analysis of our overpressure model to halite properties.

2. Seven samples of Pre-Cambrian to Miocene age were tested to provide information for stress dependency and elastic-permeability relationships of salt rock at high pressure of confinement. Five of the samples from Pakistan (agricultural samples), Russia (Cambrian age), UK (Triassic age), and Sicily (Miocene age) showed visibly undamaged salt rock after coring. An additional two sample from Pakistan (agricultural sample) showed visible fractures after coring. This dataset was used for modelling overpressure in the salt basin of the Levant, Eastern Mediterranean.
3. Two agricultural samples were obtained from Likit salt lick bricks (SLB) (www.likit.co.uk/). One sample with visible fractures and the other visibly intact were evaluated for experimental, concept testing to evaluate the impact of dissolution on the geophysical properties of intact (non-fractured) and fractured salt rock samples.

X-Ray micro-CT (XCT) imaging was undertaken on one halite core plug from the Caltanissetta basin, Sicily. Imaging was undertaken to identify if any pore network existed within salt rock. One kainite and one polyhalite sample of Messinian age were obtained from the Caltanissetta Basin in Sicily and DDSP 374 in the Central Mediterranean, respectively. These sulfate samples were obtained alongside gypsum and halite samples to constrain their density (bulk and grain), porosity (connected), and permeability parameters, as possible evaporite mineral/ lithology alternatives in modelling of MSC Stage 2 (Mobile Unit) and Stage 3 (Upper Unit). The properties obtained for kainite and polyhalite were disregarded from modelling, as both minerals were considered unlikely across our model areas and typically in thinner layers than our thick layers modelled.

Nine anhydrite samples of Permian and Messinian age were obtained from the Boulby Mine, UK and DDSP Site 371 in the Western Mediterranean, respectively. Core samples were evaluated to constrain density (bulk and grain), porosity (connected), and permeability, as possible input parameters in our modelling of MSC Stage 3 (Upper Unit) in the Western Mediterranean. The properties obtained were disregarded from modelling in our study area as pressure and temperature conditions of the Upper Unit gypsum relative to the boundaries of the gypsum dehydration to anhydrite reaction were considered unlikely.

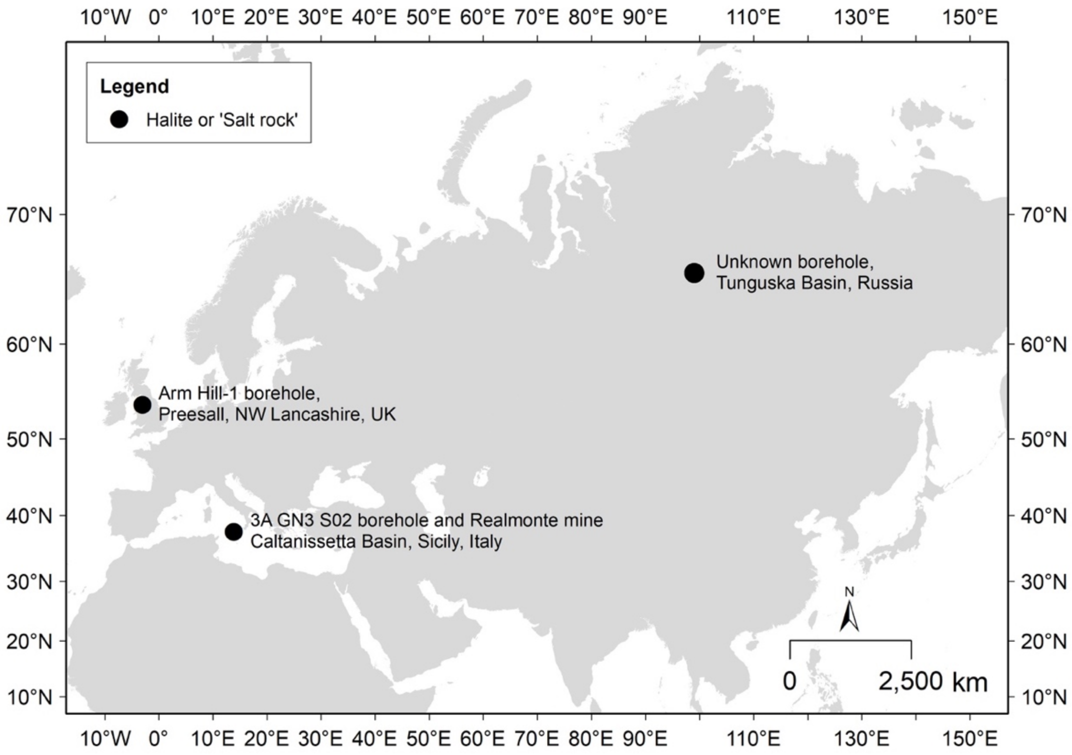

Figure 2: Core samples of salt rock obtained for study across Europe and Russia

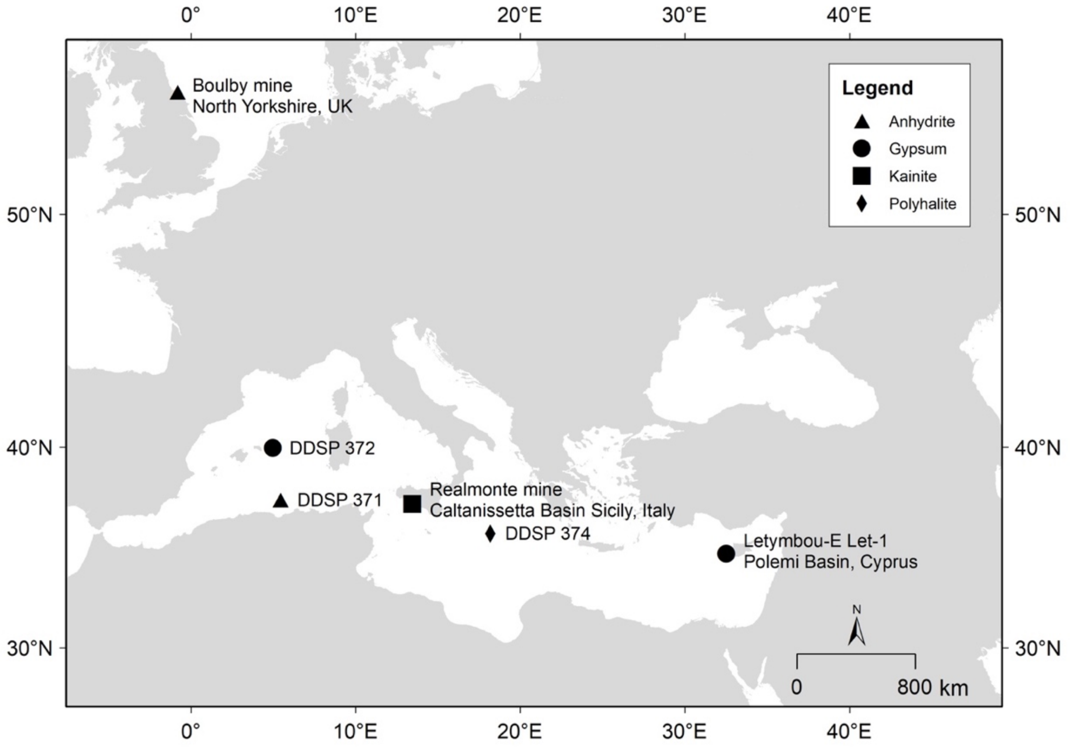

Figure 3: Core samples of Anhydrite, Gypsum, Kainite and Polyhalite, obtained for study across the Mediterranean and UK

The collection of seismic data undertaken as part of this thesis include:

1) 2D SALTFLU multichannel seismic reflection data (e.g., E12-SF 03) was acquired by GALSI S.p.A in 2012. Seismic and VRMS velocity data provided by the Instituto Nazionale di Oceanografia e di Geofisica Sperimentale was used for interpretation of structures, estimation of present-day seismic derived thicknesses (time and depth), and to understand if gypsum dehydration occurs in the Algero-Balearic basin.
2) 2D Mediterranean Sea (MS) multichannel seismic reflection data (e.g., MS-39) was acquired by the Italian National Institute of Oceanography and Experimental Geophysics (OGS) in 1972. Seismic data provided by the Instituto Nazionale di Oceanografia e di Geofisica Sperimentale was used for interpretation of structures and estimation of present-day seismic derived time thicknesses.
3) 2D seismic profile EMED-00-062A was acquired by Spectrum in 2000 and PSTM reprocessed in 2011, and broadband reprocessed in 2017. Seismic data was examined to ascertain present-day seismic derived time thicknesses of the Miocene (pre-Messinian and Messinian) and evaluate seismic facies around our crater pockmark modelling area in the Levant Basin, Eastern Mediterranean.

1.5 Thesis overview

Chapter 2 is a numerical modelling study on pore pressure evolution in the Western Mediterranean basin. In this chapter I tackle the question: ***What is the magnitude of overpressure generated from basin inception to present-day and within Messinian evaporites for the Liguro-Provençal and Algero-Balearic basins?*** Here I consider 1D models, brine as the only pore fluid and overpressure due to the disequilibrium compaction mechanism. To constrain some of the hydrogeological properties of evaporites as input parameters in our modelling, I performed laboratory experiments on nineteen samples representing a range of evaporate lithologies (anhydrite, gypsum, halite, kainite, polyhalite) in the Mediterranean basin. I also undertook further laboratory testing to constrain input parameters of salt rock at high confining pressure, that are limited in literature.

In Chapter 3 I continue the study on overpressure by undertaking a modelling study to test if crater pockmarks observed at the base of the Messinian evaporites in the Eastern Mediterranean may be caused by venting of methane gas accumulations towards the seafloor, triggered by sea-level fall at the onset of the Messinian Salinity Crisis. In this chapter I tackle two questions: ***(i) Was the field of pockmarks triggered by sea-level fall of 10s to a few 100s m or sea-level***

fall > 1000 m? and ***(ii) Did seal failure likely occur from Middle to Late Miocene or deep Early Miocene sands?*** Here I use a 1D analytical model of chimney formation caused by gas overpressure.

In Chapter 4 I deviate from modelling studies to undertake a standalone laboratory testing component to quantify changes in elastic and hydromechanical properties at different effective pressures and during dissolution of salt rock by migration of brine. In this chapter I tackle two questions: ***(i) Can we infer changes in hydromechanical properties from changes in geophysical properties at different effective pressures in evaporites?*** and ***(ii) What is the impact of dissolution on geophysical properties of intact (non-fractured) and fractured salt rock?*** Investigation into the impact of dissolution on geophysical properties was terminated when failure of the rig equipment occurred under high pressure of confinement.

In Chapter 5, I discuss the links between laboratory testing and modelling studies. I describe how the uncertainty of the overpressure models was progressively reduced through the various studies by quantifying elastic and hydromechanical properties of salt rock. From our various modelling scenarios in the Western and Eastern Mediterranean, I also discuss timing and overpressure magnitudes of three possible fluid expulsion events during the MSC. Finally, I discuss limitations of each of the studies and possible future work.

Chapter 2 The Messinian Salinity Crisis as a trigger for high pore pressure development in the Western Mediterranean

Evaporites are typically described as impermeable seals that create some of the world's highest reservoir pressures beneath the salt seal. However, several laboratory studies demonstrate that evaporites can retain open pore spaces that hydraulically connect the sediments above and below them in sedimentary basins. During the Messinian Salinity Crisis (5.97 to 5.33 Ma), up to 2400 m thickness of evaporites were rapidly deposited in the Western Mediterranean, which may have generated high pore fluid overpressure in the basin sediments. Here we use one-dimensional numerical modelling to quantify the temporal evolution of overpressure at two distinct locations of the Western Mediterranean, the Liguro-Provençal and Algero-Balearic basins, from the Miocene to Present. We reconstruct the sedimentation history of the basin, considering disequilibrium compaction as an overpressure mechanism and constraining model parameters (such as permeability and porosity) using laboratory experiments and the literature. In the Liguro-Provençal basin the highest overpressure of 11.2 MPa occurs within the halite during deposition of Pliocene to Quaternary sediment, while in the Algero-Balearic basin at the base of the Emile Baudot Escarpment, the highest overpressure of 3.1 MPa also occurs within the halite but during stage 3 of the Messinian Salinity Crisis (5.55 to 5.33 Ma). In the Algero-Balearic basin an overpressure of 3.1 MPa could have been sufficient to hydro fracture the sediments, which agrees with the development of fluid escape features observed on seismic reflection profiles. In general, our models with evaporite deposition rates above 20 m kyr^{-1} and permeabilities below 10^{-18} m^2, suggest that high overpressure, approaching lithostatic, can be generated in salt basins.

2.1 Introduction

The Messinian Salinity Crisis (MSC) has been described as an ecological crisis, generated by geodynamic and climate drivers (Roveri et al., 2014) including processes from plate convergence associated crustal deformation, mantle-resisted slab dragging and tearing, to isostatic responses of salt loads, possibly causing the Atlantic-Mediterranean gateway closure (Capella et al. 2019). The MSC led to the rapid sedimentation of thick layers of halite and other evaporite minerals in the Mediterranean. Evaporites are impermeable seals that create some of the world's highest reservoir pressures beneath the salt seal (Warren, 2016). However, several laboratory studies demonstrate that evaporites can have porosities of 0.5 to <10% (e.g., Casas et al. 1989; Kröhn et al. 2015, 2017; this study) and that pore fluid flow with permeabilities from 10^{-11} to $<10^{-21}$ m^2 can occur through them by cracks and/or dilatancy of grain boundaries (e.g., Popp et al., 2001; Urai et al., 2019; Zhang et al., 2020; this study). At basin scale, this laboratory observation suggests that, despite their low permeability, evaporites are able to transmit pore fluid pressure through them. Hence, evaporite sedimentation can potentially generate overpressure within the evaporites and in the sediments below them, ultimately affecting the mechanical properties and pore fluid flow of sediments during the geological evolution of a basin.

This work contributes to the Marie Skłodowska Curie Innovative Training Network "SALTGIANT" which aims to understand the Mediterranean Salt Giant, one of the largest salt deposits on Earth (https://www.saltgiant-etn.com/). Here we provide insights into the pore pressure evolution in the Western Mediterranean (WM) basin, where up to 1000 m of thick well-preserved halite were deposited over a period of less than 50 kyr during the MSC (Dal Cin et al. 2016). Fluid flow and overpressure has been previously studied in WM sediments (e.g., Bertoni et al. 2015; Arab et al., 2016), although the impact of the overpressure on the hydrodynamics of the basin has primarily been addressed in Pliocene to Pleistocene sediment or areas (e.g., West Alboran Basin) where evaporites are absent (e.g. Revil et al. 1999; Lafuerza et al. 2009; Fernandez-Ibanez et al. 2017). Previous studies in the WM show that overpressure associated with the presence of methane gas can exist in unconsolidated shallow sediment (depths <350 m below seabed), with fluid overpressure observed to return towards hydrostatic below the overpressure zones (e.g., in ODP Site 975; Revil et al. 1999). At these shallow depths, the likely cause of overpressure is in-situ microbial degradation of organic matter that generate free gas, gas exsolution during sea-level lowering, and disequilibrium compaction (Revil et al. 1999; Lafuerza et al. 2009). In contrast, studies in the Eastern Mediterranean (EM) basin have focused on fluid flow where evaporites are present, in a remnant area of the Neo-Tethyan oceanic basin that opened in the Early Mesozoic, and in an area known for being a prolific gas province (e.g., Bertoni et al. 2015; Eruteya et al., 2015; Al-Balushi et al., 2016). Focused dominantly on pipe structures in the Levant Basin, Eruteya et al., (2015) proposed their formation from i) dissolution of Messinian evaporites (western group pipes) that predates deformation of the overburden, and ii) differential loading during late Pliocene deformation that elevated pressure within MSC evaporites (eastern group pipes). Other modelling on the petroleum system of the Levant Basin also suggest that both instantaneous drop in sea-level and evaporite loading impacted subsurface pressures (Al-Balushi et al., 2016). Quantification of overpressure from basin inception to present day and estimates of overpressure magnitude triggering fluid expulsion events during the Messinian has not been the dominant focus of previous studies in the WM. We use numerical modelling to quantify and assess the time evolution and role of pore fluid overpressure in two WM basins, the Liguro-Provençal and Algero-Balearic basins (Figure 4). We propose that in the WM evaporite deposition during the MSC caused high overpressure that likely continues to exist within the MSC evaporites and pre-Messinian sediments, and may explain some of the fluid escape features observed on seismic data.

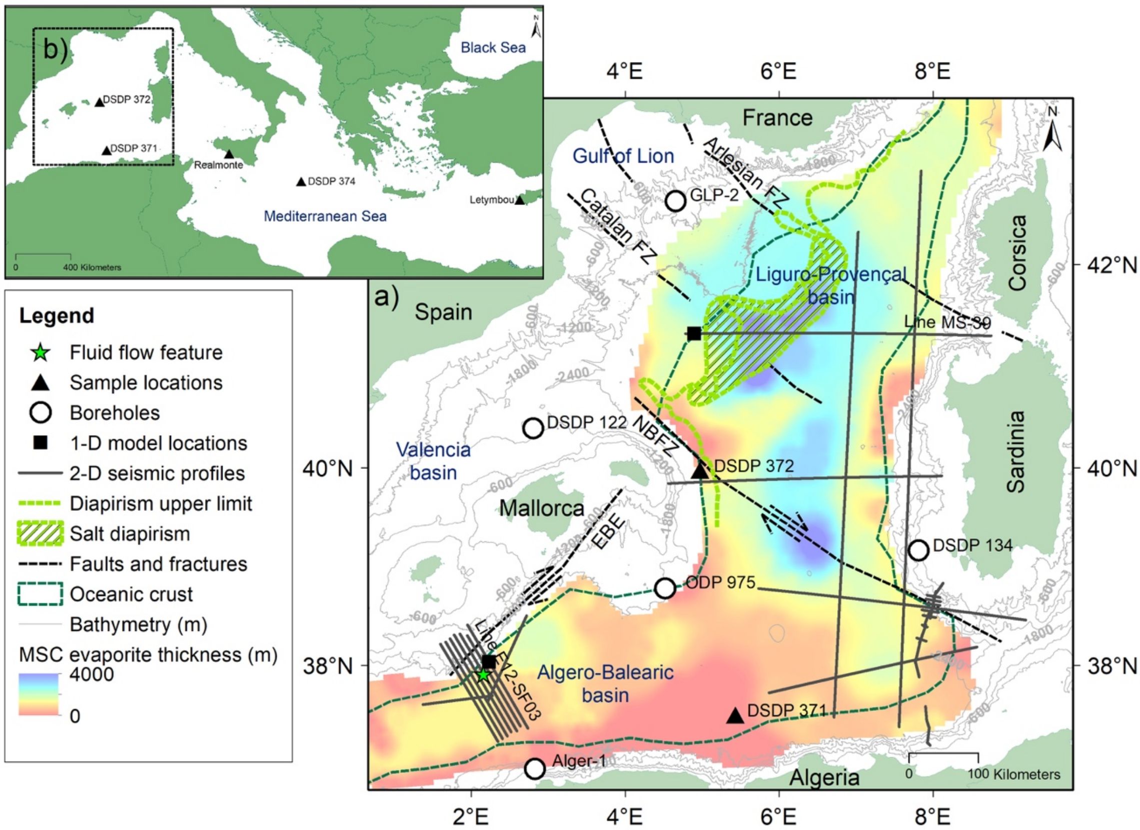

Figure 4: Tectonic and geographic setting of the study area. a) Map of the Western Mediterranean (black box in b)) showing the location of seismic profiles including those used in this study (dark grey lines), modified and smoothed distribution of evaporite thickness taken from Haq et al. (2020), Emile Baudot Escarpment (EBE) and North Balearic Fracture Zone (NBFZ) taken from Dal Cin et al. (2016; dashed black lines), Arlesian Fracture Zone (ArFZ) and Catalan Fracture Zone (CFZ) taken from Maillard et al. (2003), boundary of oceanic crust taken from Sabat et al. (2018; dashed dark green lines), and bathymetric contours (light grey lines) from the European Marine Observation and Data Network (EMODnet; https://portal.emodnet-bathymetry.eu/). The extent of the oceanic crust and NBFZ are used in this study to separate basin boundaries. Black squares indicate the location of 1-D overpressure models. Green star shows the location of possible evaporite diagenesis and a fluid flow feature from Bertoni et al. (2015). Green hatched area indicates a salt diapir province and piercement at seabed, taken from seismic profiles and bathymetric data from the National Oceanic and Atmospheric Administration (NOAA; https://maps.ngdc.noaa.gov/viewers/bathymetry/), and diapirism upper limit taken from Maillard et al. (2003; dashed green line). b) Location of Messinian evaporite samples evaluated in this study.

2.2 Stratigraphic framework

Depositional environments and stratigraphic lithologies of the WM have been established using borehole, outcrop and seismic facies analysis, with limited stratigraphic correlation between onshore successions and deep offshore basins (e.g., Driussi et al. 2015). The stratigraphic framework includes Oligocene to Miocene pre-Messinian successions, the three stage stratigraphic model for the Messinian, followed by Pliocene to Quaternary successions.

The Oligocene to Miocene deposits show significant facies variability from continental to brackish to marine environments (Cherchi et al. 2008). In the Gulf of Lion margin, drilled successions comprise shallow-water limestone to clastic deposits (Cherchi et al. 2008). Syn-rift Oligocene to Miocene successions from the Sardinia graben comprise similar lithologies of shallow-water limestones to clastics and hemipelagic marlstone deposits, interbedded locally with volcanic deposits, while post-rift Miocene successions comprise hemipelagic marly-silt with turbidite deposits (Cherchi et al. 2008). In the WM, Oligocene to Miocene pre-Messinian successions are characterised in general by transparent, non-reflective acoustic facies (Carminati et al, 2011).

The first stage of the MSC from Sicily for instance, is characterised by deposits of marine marlstone, alternating with diatomites and evaporites of limestone, gypsum and halite, interpreted as a deep peripheral basin (Krijgsman et al., 2008; Roveri et al., 2014), while deep basins without deep well calibration are inferred to contain deposits of organic shale and/or dolostone (Manzi et al., 2013). The second stage follows widespread desiccation of the WM basin and erosion in marginal basins, leading to deposition of primary halite, clastic deposits and resedimented evaporites in deep basins (Manzi et al., 2013). The third stage is characterised by variable evaporite deposition from primary evaporitic facies (selenite, laminar gypsum and halite cumulate) to clastic evaporitic facies (gypsrudites, gypsarenites and gypsum siltites), as well as fresh to brackish water deposits of the Lago Mare event (Roveri et al., 2014; Krijgsman et al., 2008). From the Pliocene to Quaternary (P-Q), overburden sediments are dominated by deposition of marlstone with variable amounts of claystone and siltstone, intercalated locally with sandstone and volcanic deposits (Hsü et al., 1978; Ryan et al., 1973; Burollet et al., 1978; Leroux et al., 2017). In the WM, the Lower Pliocene successions are characterised by semi-transparent reflections, becoming more reflective in the Upper Pliocene to Quaternary (Dal Cin et al., 2016).

In the deep basin of the WM, the MSC has also been described as a trilogy of seismic units defined as the Lower Unit (LU), Mobile Unit (MU) and Upper Unit (UU) (Roveri et al., 2014). On seismic data, the LU is characterised in general by high amplitude reflections, the MU is characterised by transparent acoustic facies of halite, while the UU is characterised by high amplitude reflectors of gypsum alternating with transparent layers of halite (Roveri et al., 2014). The stratigraphic model applied in this study integrates both these seismic stratigraphic units and the three stages of the MSC; Stage 1 corresponds to the Lower Unit (LU; 5.97 to 5.6

Ma), Stage 2 to the Mobile Unit (MU; 5.6 to 5.55 Ma), and Stage 3 to the Upper Unit (UU; 5.55 to 5.33 Ma) ().

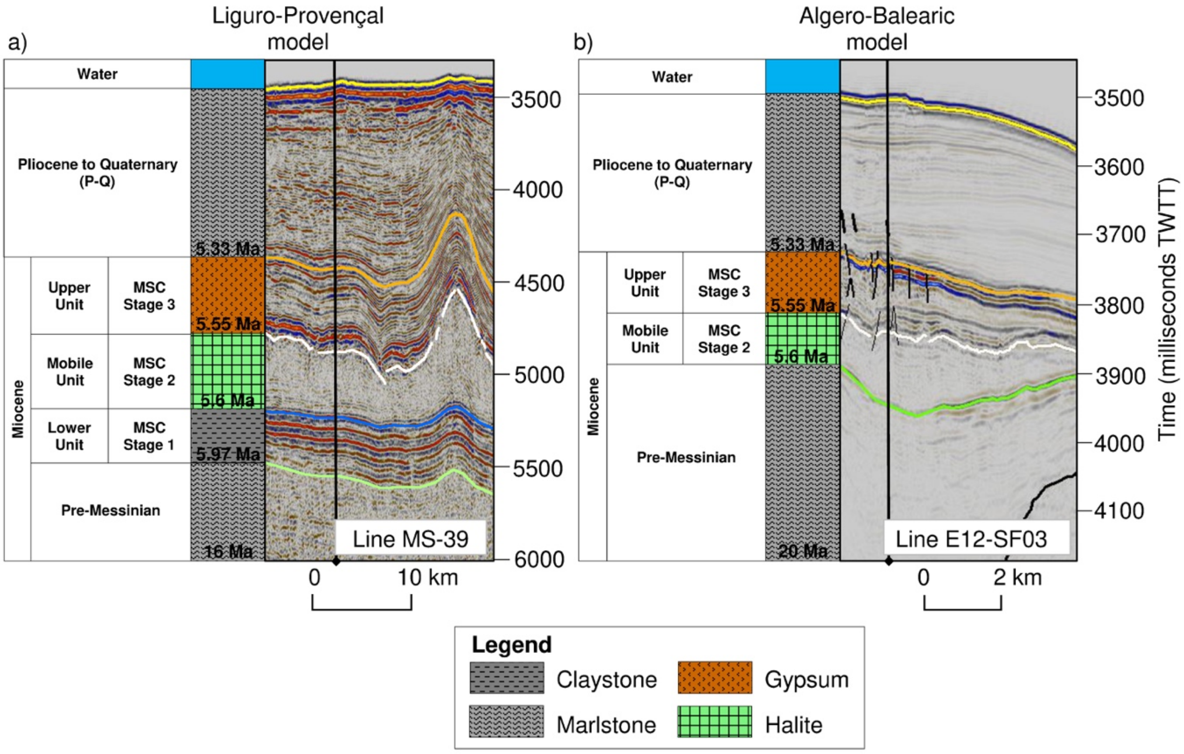

Figure 5: Seismic profiles for (a) the Liguro-Provençal basin (central oceanic location within the basin) and (b) Algero-Balearic basin (at the base of the Emile Baudot Escarpment) models. Images show the seismic stratigraphic units and lithology modelled on the left. Seismic line locations are shown in Figure 4.

2.3 Data

2.3.1 Boreholes, samples and seismic sections

To constrain the lithology of our modelled units, we reviewed seismic data and six boreholes in the WM. Lithology for the pre-Messinian succession was determined using data from boreholes Alger-1, on the Algerian shelf, and GLP-2, on the Gulf of Lion mid-slope (Burollet et al., 1978; Leroux et al., 2017). Late Miocene Messinian Upper Unit and the Pliocene to Quaternary were determined using Deep Sea Drilling Project (DSDP) Sites 122, 134, 371, 372 and Ocean Drilling Program (ODP) Site 975 (Ryan et al., 1973; Hsü, et al., 1978; Comas et al., 1996). Further details of primary lithologies assigned to each modelled unit are given in Section 4.3. A limited amount of geophysical log and core-based physical property data were available from offset wells GLP-2, (DSDP) Sites 371, 372 and (ODP) Site 975, with no data available in the basin-centre. Sonic log estimates of claystone porosity with depth were available from GLP-2 (Leroux et al., 2017), with density data and porosity estimates available at shallow depths for the Pliocene to Quaternary in (DSDP) Sites 371, 372 and (ODP) Site 975 (Hsü, et al., 1978). Data for the IODP expeditions can be accessed from Expedition Science Operators at (http://web.iodp.tamu.edu/OVERVIEW/) and (https://mlp.ldeo.columbia.edu/logdb/).

We used evaporite core samples in our laboratory experiments to constrain some of the hydrogeological properties of evaporites in the Mediterranean and North Sea basins, prior to lithology assignment of our modelled units. Evaporite cores include Permian and Messinian Upper Unit anhydrite (Boulby, UK and DSDP Site 371), Messinian Upper Unit gypsum (DSDP Site 372 and Letymbou-E Let 1, Cyprus), Messinian Mobile Unit equivalent halite and kainite (Realmonte mine, Sicily) and Messinian Upper Unit polyhalite (DSDP Site 374). Lithological descriptions of the cores are provided in (Tables 1 and 2).

Age	**Evaporite mineral**	**Location**	**Lithological description**	**Pore radius (µm)**	**Connected porosity (%)**	**Bulk/ Grain density (g cm^{-3})**	**Permeability (m^2); P_c = 1.5 MPa**	**Permeability (m^2); P_c = 17.2 MPa**
Messinian Stage 3 (Upper evaporites)	Anhydrite (n=1)	DSDP Site 371, Western Mediterranean	Milky white anhydrite masses with thin seams of black organic material (1)	0.005 - 0.091	2.2	2.85/ 2.91		7.9x10^{-21}
	Gypsum (n=1)	DSDP Site 372, Western Mediterranean	Laminated with a coarse mosaic of gypsum crystals and infilling by fine grained micritic carbonate and gypsum crystal sublamina (1)	0.026 - 1.498	2.5	2.26/ 2.31		3.15x10^{-17}
	Polyhalite (n=1)	DSDP Site 374, Central Mediterranean		0.009 - 2.146	3.6	2.45/ 2.54		2.07x10^{-18}
	Gypsum (n=4)	Polemi basin, Cyprus	Massive greyish saccharoidal gypsum to laminated greyish gypsum with fine interbedded marlstone	0.036 - 1.92	2.3±0.8	2.27±0.03/2.325 ±0.005	1.2x10^{-17} ± 0.4x10^{-17}	1.1x10^{-17} ± 0.5x10^{-17}
Messinian Stage 2 (Peak of MSC)	Halite (n=3)	Caltanissetta basin, Sicily	White with contraction cracks prevalent throughout (2)	0.002 - 2.268	1.5±0.53	2.11±0.02/ 2.15±0.02	1.0^{-13}	10^{-15} ± 1.2x10^{-16}
	Kainite (n=1)	Caltanissetta basin, Sicily		0.002 - 3.619	0.5	2.12/ 2.13		

Table 1: Hydrogeological parameters for evaporites of the Messinian Salinity Crisis obtained from laboratory testing. References: (1) Garrison et al., 1978; (2) Lugli et al., 1999. Note that connected porosity estimates were determined using mercury injection porosimetry. P_c, confining pressure.

Period	Formation	Evaporite mineral	Location	Lithological description	Absolute porosity (%)	Bulk density (g cm^{3})	Permeability (m^{2}); P_c = 1.5 MPa	Permeability (m^{2}); P_c = 6.0 MPa
Permian	Upper Anhydrite	Anhydrite (n=2)	Boulby, UK	Pale cream to brown colour, and comprises a strong mixture of fine grained anhydrite, halite crystals and fine grained siltstone inclusions. Zoned appearances of veins filled with halite and sylvinite have been interpreted	1.2 ±1.05	2.9 ±0.3	$6.6\text{x}10^{-18} \pm 4\text{x}10^{-18}$	10^{-20}
Permian	Fordon Evaporite	Anhydrite (n=2)	Boulby, UK	Blue to grey saccharoidal anhydrite with intermixed fine grained halite and feathered pseudomorphs. Speckled outer surface texture with leaching.	9.7 ±3.6	2.55 ±0.15	$4.6\text{x}10^{-13} \pm 2.3\text{x}10^{-13}$	
Permian	Billingham main	Anhydrite (n=4)	Boulby, UK	White to grey saccharoidal anhydrite	1.4 ±1	2.85 ±0.08	$7.2\text{x}10^{-18} \pm 3.6\text{x}10^{-18}$	

Table 2: Hydrological parameters for Permian evaporites, obtained from laboratory testing. Note that absolute porosity estimates were determined using helium pycnometer. P_c, confining pressure.

Seismic profiles MS-39 and E12-SF 03 (Figure 6) were examined to ascertain thicknesses of pre-salt, Messinian and supra-salt units, and to identify locations where present-day sediment thicknesses may represent the thickest deposition in the ancient basin prior to any effects of lateral deformation, essential to conform with our 1-D vertical fluid flow modelling assumption described in Section 4 Modelling approach. The MS-39 multichannel seismic reflection data were acquired by the Italian National Institute of Oceanography and Experimental Geophysics (OGS) in 1972 as part of a regional exploration project to understand the Mediterranean tectono-stratigraphy and characterise crustal settings (Finetti et al., 2005). The SALTFLU multichannel seismic reflection data (including profile E12-SF 03) were acquired in 2012 to provide detailed pre- and post-stack time migration data and RMS velocity data over the continental slope, particularly the Emile Baudot escarpment, and deformed sequences of the Algero-Balearic abyssal plain (Wardell et al., 2014). See Figure 7 and Figure 8 for regionally extensive and uninterpreted seismic profiles MS-39 and E12-SF 03.

We used well and seismic velocity data from the literature and project company GALSI S.p.A to convert seismic time thickness units to depth. 2D ultra-high resolution multichannel seismic velocity data were available from GALSI S.p.A providing high quality velocities for Pliocene to Quaternary (P-Q) and MSC Stage 3 (Upper Unit) seismic units along the GALSI (Gas Pipeline – Algeria via Sardinia to Italy) route acquired from 2007 to 2008. Below the Upper Unit (UU), seismic velocities are considered to be of poor quality. Refer to Section 4.3 for information on velocities data used in this study.

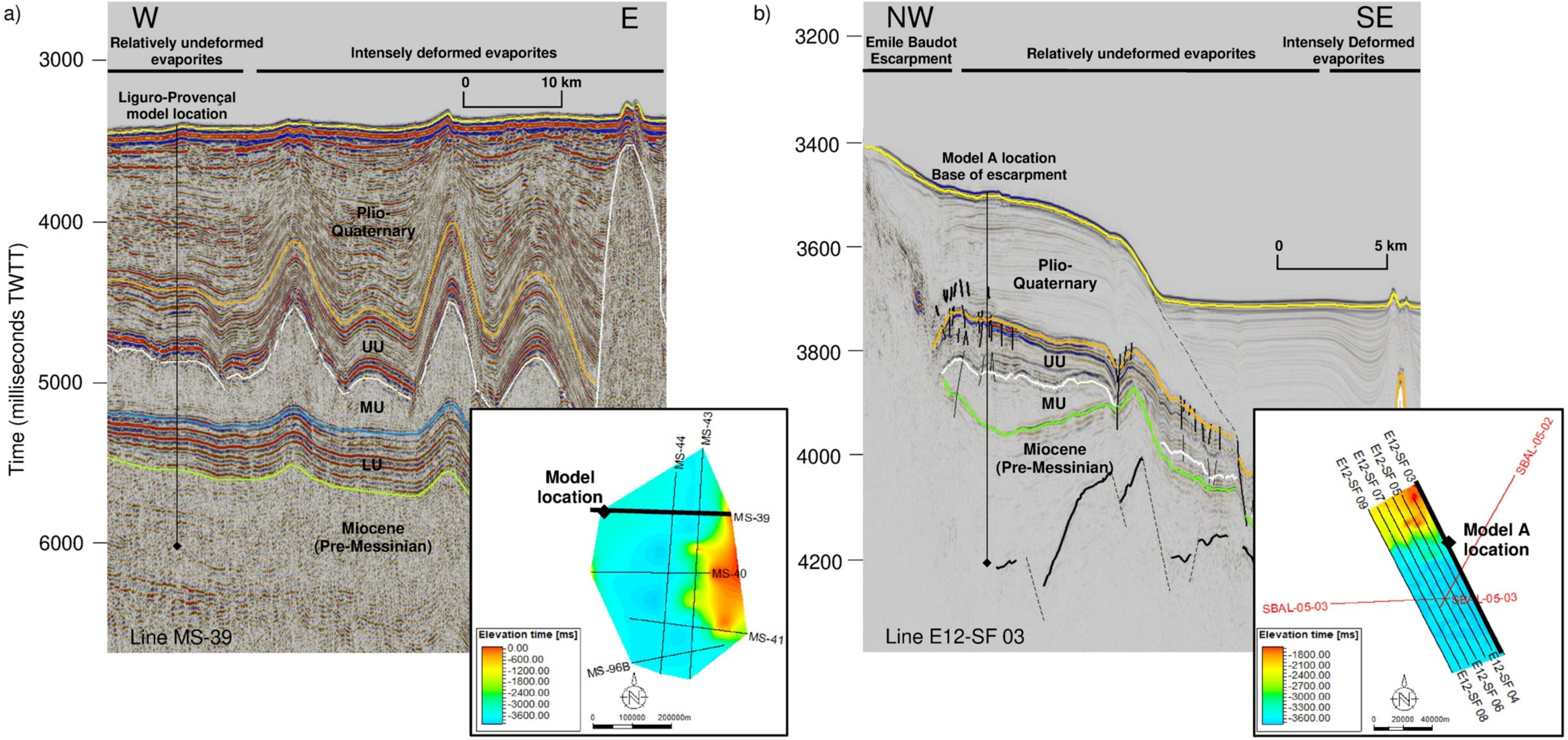

Figure 6: Seismic profiles for (a) MS-39 line and (b) E12-SF 03 line showing location of 1-D overpressure model, and interpreted horizons and faults. Note that the Lower Unit (LU) is absent in this location. Insets show the locations of Liguro-Provençal and Algero-Balearic seismic profiles (black lines) and 1-D overpressure models evaluated in this study. Seismic line locations are also shown in *Figure 4*.

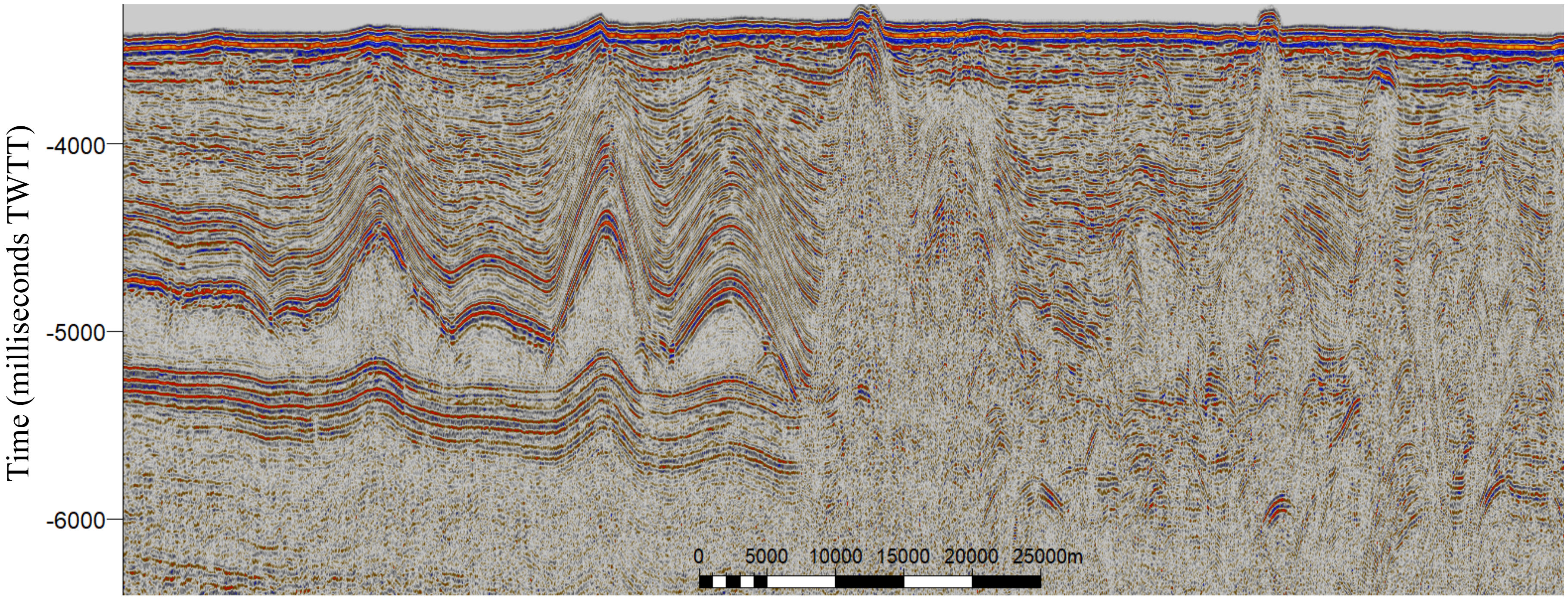

Figure 7: Seismic profile MS-39 (scale 1:600,000), extended over intensely deformed evaporites, and uninterpreted. Seismic line location is shown in Figure 4 and Figure 6.

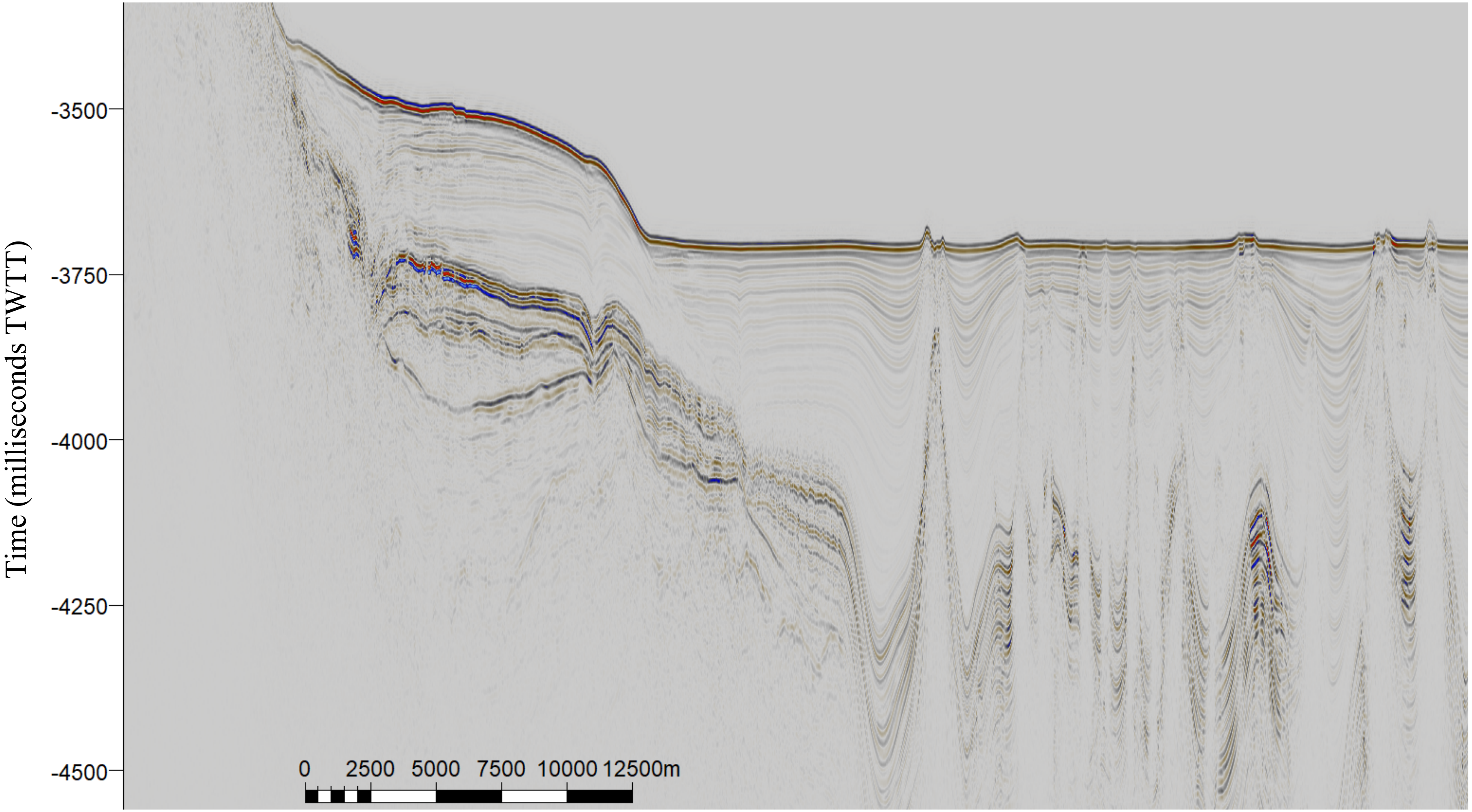

Figure 8: Seismic profile E12-SF 03 (scale 1:300,000), extended over intensely deformed evaporites, and uninterpreted. Seismic line location is shown in Figures 1 and 4 of the main manuscript.

2.3.2 Laboratory experiments

Seventeen sediment cores were used, and from each of these, a total of twenty smaller core plugs were cored, and cut and their ends ground flat. This resulted in nineteen discrete samples for porosity and permeability determinations, and one for X-ray CT-scan image analysis. Cores were selected to represent a range of evaporite lithologies and avoid impurities (e.g., claystone), while core plugs were selected on texture variation and to avoid fractures where possible.

2.3.2.1 Porosity and permeability determination

A set of 1.1-2 cm height and 2.5 cm diameter cores samples were used for high pressure (17.2 MPa and 1.38-4.83 MPa of confining and pore pressure) permeability to helium and Hg-injection porosimetry (Micromeritics AutoporeTM IV 9520 system) determinations at the University of Leeds. A second set of ~2 cm height, 5 cm diameter samples were used for absolute porosity estimates with helium pycnometer and absolute permeability with N_2 at the National Oceanography Centre (NOC) in Southampton. Further details of primary lithologies assigned to each modelled unit are given in Section 2.4.3.

Porosity and permeability were measured at room temperature (~20 °C), at atmospheric pressure conditions for porosity and under a minimum hydrostatic confining pressure of 1.5 MPa for permeability to ensure rig sealing during gas flow-through. The gas permeability to N_2 was estimated using steady state flow (SSF) and pore pressure transmission (PPT) methods (e.g., Falcon-Suarez et al., 2017), depending on the sample permeability. For all the samples, we first attempted to measure permeability using the SSF, based on Darcy's law, the most widespread method for high to moderate permeability media (above 10^{-16} m^2). For those samples with permeability below 10^{-17} m^2, we used the PPT method instead, an alternative based on transient states of the pore pressure. The PPT method was proposed by Metwally and Sondergeld (2011) based on the pulse decay method introduced by Brace et al. (1968), which consists of inducing pore pressure disequilibria in the rock and determining the permeability through the evolution of pore pressure–time decay curves towards the original steady state. For further details on the SSF and PPT methods refer to e.g., Metwally and Sondergeld (2011) and Falcon-Suarez et al. (2017).

In all the permeability determinations, Klinkemberg's correction was applied to correct the deviation resulting from slippage effect of the gas (Klinkenberg, 1941), and transform the apparent permeability into absolute permeability.

2.3.2.2 Mercury injection porosimetry

The porosity of a selection of the core plug samples was also analysed using mercury injection porosimetry with the Micromeritics AutoporeTM IV 9520 system. This model has four low pressure ports and two high pressure chambers. As mercury is a non-wetting fluid, the pressure must build up before mercury intrudes into a certain pore size and the interface crosses the throat between pore bodies. The balance between internal and external forces or pressures acting on an interface can be described by the Young-Laplace equation. The samples are cut into suitable size depending on their porosity and the penetrometer to be used. Clean and dry samples, of known weight, are then loaded into a penetrometer and evacuated. The penetrometer is automatically backfilled with mercury. The pressure is then increased to 25 psi (0.17 MPa) in the low pressure port, and up to 60,000 psi (413 MPa) in the high pressure chamber following pre-selected pressures. After reaching each pressure increment the volume of mercury intruded is recorded. Each penetrometer has been individually calibrated, therefore, the volume of mercury needed to fill the penetrometer at ambient conditions is used to calculate the bulk volume of the sample. The total volume of mercury injected is recorded assuming that at 60,000 psi all the pore volume has been filled. The grain volume is the difference between the sample bulk volume and mercury injected volume. Then the grain density can also be obtained. The pore throat size distribution and other properties can be calculated from this information (ASTM D4404-84, 2004). If necessary, a manual volume conformance and other corrections can be applied during data interpretation. All results presented here have been conformance corrected.

2.3.2.3 X-Ray Computed Tomography

X-Ray micro-CT (XCT) imaging was carried out on one halite core plug to fully understand anomalous results of permeability. To improve the signal to noise ratio, the core plug was cored and cut down to a core size of 14 mm diameter with 20 mm height. A scan image to 10.1 µm voxel resolution was achieved. The scan was conducted using a micro-focus Custom Nikon HMX ST Scanner at the University of Southampton (e.g., Callow et al., 2018). The settings used on the HMX are as follows: a source to object of 40.4 mm, source to detector of 797.9 mm, 200 kVp peak voltage, no pre-filtration of the beam, 134 ms exposure time, 3142 projections (2 frames per projection) and voxel size of 0.01 mm.

2.3.2.4 Hydrogeological parameters of the Mediterranean and North Sea basins

Tables 1 and 2 and Figure 9 show the results of permeability and porosity measurements on 19 evaporite samples. Although, the measured permeability range is wide (10^{-13} to 10^{-20} m^2), most of the anhydrite sample permeability are between 10^{-17} to 10^{-18} m^2 and have similar absolute porosity of 2.4 to 2.93% at hydrostatic confining pressure (*Pc*) of 1.5 MPa. The permeability of the anhydrite is stress dependant, decreasing to ~10^{-21} m^2 when *Pc* increases above 6.0 MPa. Two anhydrite samples show anomalously high permeability (about 10^{-13} m^2), and absolute porosity (6.1 and 13.3%), likely caused by their irregular speckled outer surface texture having prevented adequate rig sealing. The five gypsum samples show similar permeabilities in the range of 10^{-17} to 10^{-18} m^2 and connected porosity from 1.5 – 3.1%, within the *Pc* range 1.5 – 17.2 MPa, indicating low stress dependence for both properties. In contrast, the three halite samples of similar origin showed anomalously high permeability of up to 10^{-13} m^2 at *Pc* of 1.5 MPa, and high stress dependence, as this value decreased to 10^{-16} m^2 at 17.2 MPa. X-ray computed tomography on the halite shows the presence of fractures and isolated pore spaces (Figure 9). All halite samples show low connected porosity of 1.0 – 2.0%. Testing on the samples of kainite and polyhalite showed low connected porosity of 0.5 and 3.6%, respectively. We used the results of dry density and porosity for gypsum and halite, and permeability of gypsum as input parameters in our modelling. The measured halite permeabilities were disregarded from modelling as they are significantly lower than most values reported in the literature (Figure 9), likely because of pre-existing micro fracturing in the samples. Hence, undisturbed halite permeabilities from literature were used (e.g., Beauheim et al. 1991; Brodsky, 1994). The measured anhydrite permeability and porosity results were also disregarded from modelling, as anhydrite was considered unlikely across our model areas. Further details on gypsum dehydration to anhydrite results are provided in Section 2.5.

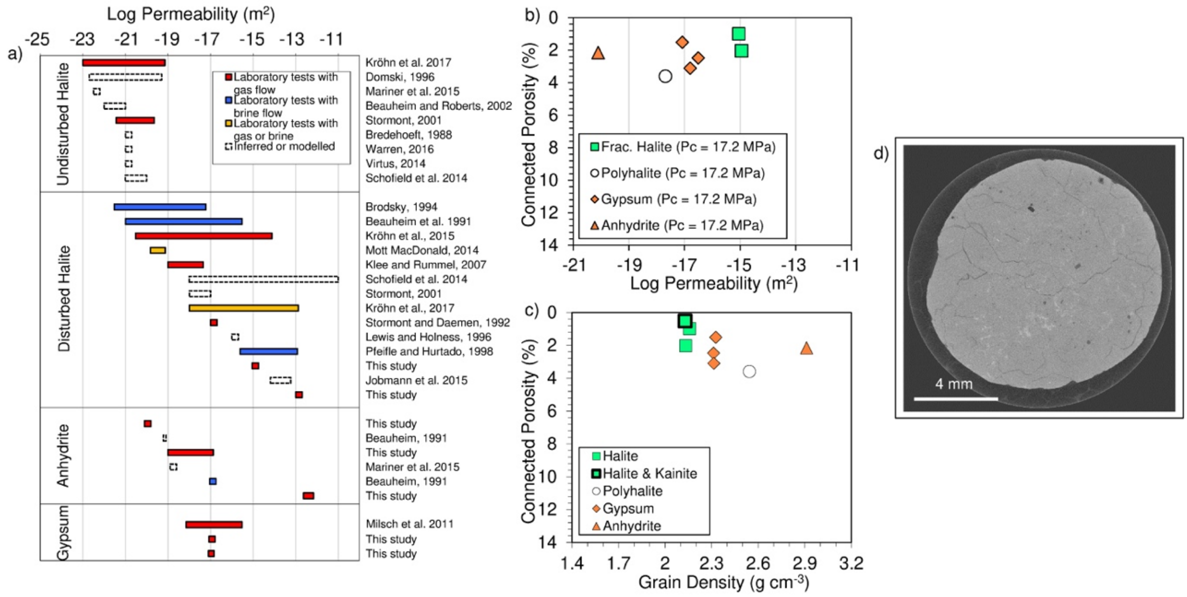

Figure 9: Physical property data compilation for evaporites. a) Global permeability ranges of evaporites including this study's laboratory results of permeability obtained for Permian and Miocene anhydrite, Miocene gypsum and fractured Miocene halite. Boundary of undisturbed/ undamaged subsurface halite <10^{-21} m^2 (Stormont, 1997; Warren, 2016) with disturbed halite permeability taken from Stormont, 1997. b) Permeability and connected porosity measurements for Miocene evaporites from this study. c) Grain density and connected porosity measurements for Miocene evaporites from this study. d) X-ray computed tomographic scan undertaken on Miocene halite with 10 µm resolution, showing the presence of fractures and isolated pore spaces (black areas).

2.4 Modelling Approach

2.4.1 1-D Disequilibrium Compaction model

Pore fluid overpressure generation in our 1-D models considers brine as the only pore fluid and overpressure due to the disequilibrium compaction mechanism. Sea level changes do not affect overpressure in sediments saturated with a near incompressible fluid such as water (e.g., Liu et al., 2009). Hence, the >1500 m sea level fall in the WM (e.g., Hsü, et al., 1977) is not considered here. Note that in this work the porosity includes any type of connected void such as intergranular pores or micro fractures along grain boundaries. Based on seismic data interpretation, we apply our 1-D models in areas with sufficient laterally extensive horizontal layers and limited tectonic compression, so horizontal fluid flow is assumed to be negligible. We account for water viscosity and density changes with variations in temperature, pore pressure and salinity.

The detailed description of the mathematical and numerical models are given in Marin-Moreno et al. (2013), and here we only provide the main equations (Table 3). To describe the mechanical compaction of sediments we consider that the change in porosity is a function of vertical effective stress (eq. 1), where depth change is controlled by eq. (2). The change in lithostatic pressure with time is expressed in terms of sediment thickness h (eq. 3). The stress compaction factor β in eq. (1) can be related to the depth compaction factor (Sclater and Christie, 1980) using eq. (4). Here we assume the empirical compaction factor β is equivalent to the bulk compressibility of the saturated sediment, as described by Hart et al. (1995). To describe fluid flow, we use Darcy's relationship (eqs. 5 and 6) and assume that changes in permeability depend on changes in porosity caused by changes in effective stress (eq. 7). Finally, combining the above equations the disequilibrium compaction model is given in eq. 8.

Equation	Equation description	Equation number	Notation
$\phi=\phi_0\exp[-\beta\sigma'_{zz}]$	Porosity change with vertical effective stress	(1)	β = Stress compaction factor γ = Parameter controlling the change in permeability with porosity μ = Viscosity ρ = Sediment density ρ_f = Fluid density σ'_{zz} = Vertical effective stress ϕ = Porosity ϕ_0 = Initial porosity at seabed conditions $\boldsymbol{K}$ = Permeability tensor K_{zz} = Vertical permeability k_i = Permeability k_{i0} = Initial permeability at seabed conditions c = Depth compaction factor g = Gravitational acceleration h = Sediment thickness at seabed conditions P = Total pore pressure P^* = Overpressure P_L = Lithostatic pressure P_h = Hydrostatic pressure t = Time $\mathbf{v}$ = Fluid velocity tensor z = Depth
$\sigma'_{zz} = \int_0^z (\rho-\rho_f)g\,dz - P^* = P_L - (P_h + P^*) = P_L - P$	Vertical effective stress definition	(2)	
$\frac{DP_L}{Dt} = \rho g \frac{Dh}{Dt}$	Time evolution in lithostatic pressure with sediment thickness	(3)	
$\beta = \frac{c}{(\rho-\rho_f)g}$	Depth compaction factor to stress compaction factor conversion	(4)	
$\rho_f \mathbf{v}\phi = \frac{-\boldsymbol{K}}{g}.\nabla(\mathrm{P}-\rho_f g z)$	Darcy's relationship	(5)	
$K_{zz} = \frac{k_i, \rho_f, \mathrm{g}}{\mu}$	Vertical permeability definition	(6)	
$k_i = k_{i0}\exp\,[\gamma(\phi^2-{\phi_0}^2)]$	Permeability versus porosity relationship	(7)	
$\frac{DP}{Dt} = \nabla.\left(\frac{1-\phi}{\phi\beta\rho_f g}\boldsymbol{K}.\nabla(P-\rho_f g z)\right) + \rho g \frac{Dh}{Dt}$	Disequilibrium compaction model	(8)	

Table 3: Governing equations for the 1-D disequilibrium compaction as described by Marin-Moreno et al. 2013

2.4.2 Modelling strategy and scenarios

Our modelling strategy (Figure 10) commences with a set of rock hydrogeological properties for each unit from laboratory experiments performed in this study and the literature (Table 1 and Figure 9). We then run our 1-D disequilibrium compaction model using these rock properties and estimates of sedimentation rate from pre-compacted thickness and sedimentation time for each unit. Pre-compacted thicknesses are determined applying a percentage increase above present-day thicknesses estimated from seismic data. If the present-day modelled compacted thicknesses and present-day seismic-derived thicknesses are similar, within a 5% tolerance, we assume the calculated present-day pore pressure, bulk density, porosity, compressibility and permeability depth profiles represent those in-situ. Otherwise, we re-evaluate input parameters, considering their inherent uncertainties, and re-run the model until the observed and calculated thicknesses are within tolerance. A corollary of this approach for model validation is the assumption that the hydrodynamic and compaction history generated by the model represent those of our study area.

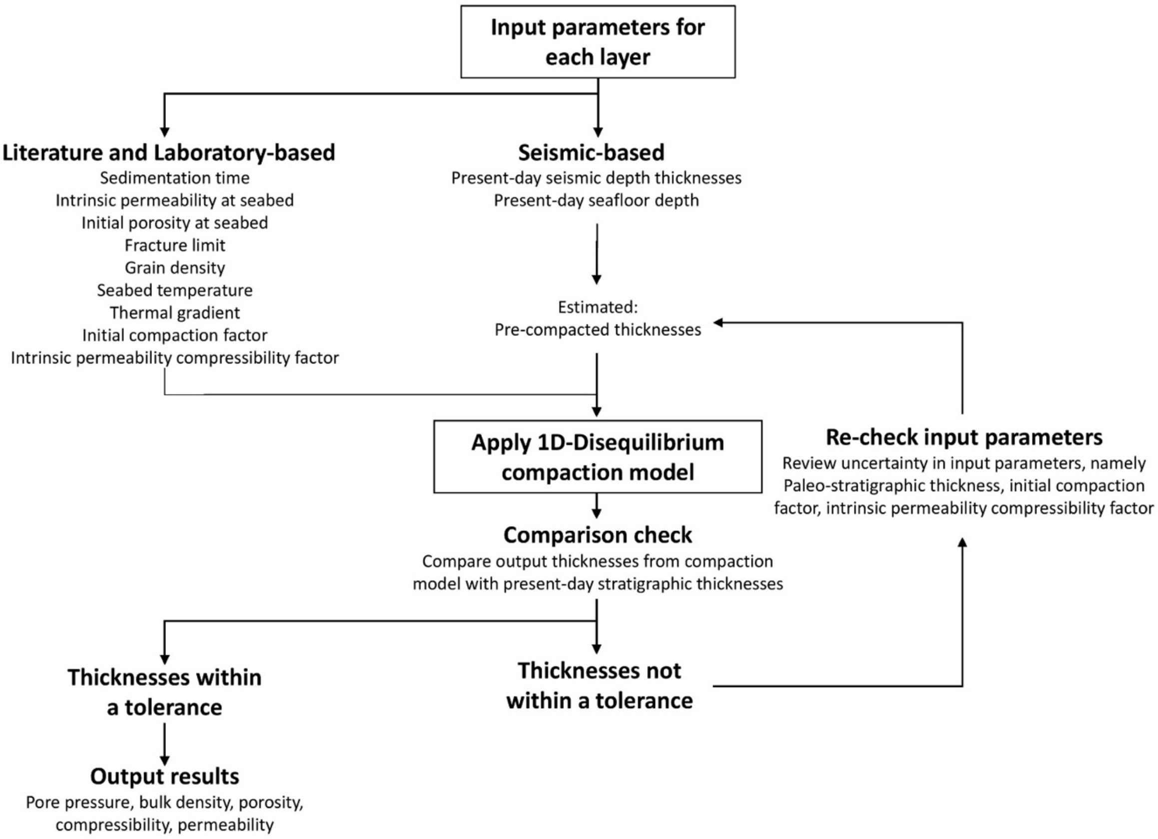

Figure 10. Modelling workflow. See text for detailed description.

For both the Liguro-Provençal basin and the Algero-Balearic basin at the base of the Emile Baudot Escarpment, our approach has been to model three scenarios incorporating low, most likely and high estimates of overpressure, which cover the full range of possible variations in fracture limit and permeability. Here we define the fracture limit as the ratio of overpressure to vertical effective stress under hydrostatic conditions, sometimes defined in the geoscience literature as λ*, above which vertical fractures can occur. To represent changes in fluid flow due to the generation and propagation of vertical fractures, on a numerical cell-by-cell basis, we assume that once overpressure exceeds the fracture limit the permeability increases by two orders of magnitude. This increase in permeability is related to a threshold value above which permeability does not influence our results (see Section 2.5 for further discussion). In areas without significant tectonic compression and with sufficiently extensive horizontal strata, the major principal stress is vertical and the intermediate and minor stresses are in the horizontal plane. Hence, here we assume that fractures propagate vertically and open horizontally and with fracture limits of 0.8±0.1 (e.g., Nikolinakou et al., 2014; Luo et al., 2017). In-situ fracture pressure measurements (e.g., traditional and extended leak-off test data) were only available from wells on the basin margin, limiting our ability to constrain fracture limits in the deeper basin-centre. As no data exists for the basin-centre halite, the simplest model we could assume was a horizontal to vertical effective stress ratio of 0.8, taken from initial stresses applied in other modelling projects near a salt diapir under hydrostatic conditions (Nikolinakou et al., 2014). The relatively high λ* implicitly accounts for the additional overpressure required to also overcome the tensile strength of the material. As we apply 1D modelling, the magnitude of the two horizontal stress components do not influence our results.

We positioned our Liguro- Provençal model in the south of the basin between the North Balearic and Catalan transverse fracture zones, an area also referred to in the literature as the North Balearic Basin (Figure 4; black box) where undeformed to mildly deformed sediment on seismic data (e.g., seismic profile SPBal-15 & SPBal-27) progressively deepens from the North Balearic fracture zone towards the Gulf of Lion (Maillard et al., 2003 & 2020). In comparison, the Gulf of Lion slope between the Catalan and Arlesian transverse fracture zones (Figure 4) tilts towards the southeast with listric faults in the upslope, salt anticlines and translation in the mid-slope and contraction and diapirs in the downslope area (Maillard et al., 2003). An extensive region with relatively undeformed sediment also exists on seismic reflection data across the basin plain in the Gulf of Lion (Mianaekere et al., 2020). To the east of our Liguro-Provençal model, salt diapirs exist restricted to a northeast to southwest boundary of the deep basin where steps in top basement reside (Figure 4; Maillard et al., 2003). Two limitations of our method for the WM are that it is only applicable for sediments that are relatively undeformed laterally and that we do not account for the overprint in overpressure generated during formation of a diapir. Our Liguro-Provencal model is located ~6 km from the synclinal axis of a salt diapir. If we had considered repositioning the model ~8 km further west of its current location (total of 14 km from the synclinal axis of the diapir), unit thicknesses (pre-kinematic) would be similar and so overpressure estimates would remain similar to our 1-D model results.

The most likely scenario uses a fracture limit of 0.8 and permeability at seabed for gypsum and halite of 10^{-18} and 10^{-20} m^2, respectively. The low scenario uses a fracture limit of 0.7 and permeability of gypsum and halite of 10^{-17} and 10^{-19} m^2, respectively. The high scenario uses a fracture limit of 0.9 and permeability of gypsum and halite of 10^{-19} and 10^{-21} m^2, respectively. See Table 4 for a summary of the non-default parameters used in the low and high scenarios. Four additional scenarios are presented that evaluate the sensitivity of overpressure to common halite properties (porosity and permeability), to understand the impact of downward fluid migration on our models, to ground truth whether mineral dehydration is plausible at our model locations in the Algero-Balearic basin, and to determine timing of fluid expulsion in the WM. Sensitivity of overpressure to halite properties was modelled using halite permeabilities of 10^{-16} - 10^{-22} m^2 and initial seabed porosity of 0.1 - 4.0%. For timing of fluid expulsion events, conservative values for fracture limit of 0.7, permeability for gypsum and halite of 10^{-19} and 10^{-21} m^2, respectively, and a Lower Unit package thickness of gypsum of 1405 m are used. The sensitivity of the model overpressure to downward fluid flow into basement rock, was modelled using ranges in pre-Messinian claystone permeabilities of 10^{-17} - 10^{-22} m^2 at porosities of 2 - 14% for a 4000 m subsurface depth. To ground truth mineral dehydration as an overpressure mechanism in the region, heat flow of 80 - 120 m W m^{-2} (Carballo et al., 2015), thermal conductivities for marlstone of 1.5 - 3.0 W m^{-1} K m^{-1} (Erickson et al., 1978), thermal conductivities for gypsum of 1.0 - 1.3 W m^{-1} K m^{-1} (Robertson, 1988; Elif et al., 2017), thick basin-ward units and seabed temperature are used to estimate the thermal structure of the 1D sediment column. Combining these temperature data with pressure data we estimate the P-T conditions of the Algero-Balearic Upper Unit Gypsum relative to the boundaries of the dehydration reaction. Here we assume that present-day thicknesses adequately represent maximum burial depth of the sediment. Location of the basin-ward thicknesses on the lowermost slope of the continental rise is given in Section 2.6. See Table 4 for a summary of the non-default parameters used in each of the additional scenarios.

Property	Units	Dominant lithology	1-D Model range		Reference
			Low	High	
Compressible initial porosities at seabed	%	Halite	0.1	4.0	this study
Fracture Limit	Decimal	All	0.7	0.9	this study
Heat flow	W m^{-2}	All	80	120	Carballo et al., 2015
Permeability at seabed	m^2	Gypsum	10^{-17}	10^{-19}	this study
Permeability at seabed	m^2	Halite	10^{-16}	10^{-22}	this study
Thermal conductivity	W m^{-1} K m^{-1}	Gypsum	1.0	1.3	Robertson, 1988; Elif et al., 2017
Thermal conductivity	W m^{-1} K m^{-1}	Marlstone	1.5	3.0	Erickson et al., 1978

Table 4: Non-default physical property parameters used in uncertainty analysis of each model or sensitivity analysis of additional scenarios.

2.4.3 Modelling parameters and boundary conditions

Our seismic stratigraphic model extends to 4 km below the seabed and comprises five seismic stratigraphic units, three of which represent the Messinian Salinity Crisis. Seismic units were interpreted on PSTM data with thicknesses in time for each unit converted to depth using a range of velocities from well and seismic velocity analysis over the Mediterranean (Table 5). Present-day thicknesses were selected from the mid-range of thicknesses calculated for each unit, except where high quality seismic velocity data existed from the GALSI project. We use the GALSI data to calculate the thicknesses of Pliocene to Quaternary (P-Q) and MSC Stage 3 (Upper Unit) of the Liguro-Provençal deep basin model.

Unit	Velocity range (m/s)	Remarks
Pliocene to Quaternary (P-Q)	2000 – 3150	• 2000 m/s is reported from the Q5 to seafloor surface (top P-Q layer) around the Gulf of Lion using an average of velocities derived from various datasets (1). • In the deep basin of the Western Mediterranean, we expect an average velocity of 2930 m/s using velocities from 2D Ultra-high resolution Multichannel Seismic data over the Algeria to Sardinia basin centre (2). • 3150 m/s is reported from the P11 to PXX surface (base P-Q layer) around the Gulf of Lion mid-slope GLP-2 well (1).
Messinian Upper Unit (UU)	3100 – 3500	• 3100 m/s is reported from seismic velocity analysis of profile MS-39 in the Western Mediterranean (3).

		• In the deep basin of the Western Mediterranean, we expect an average velocity of 3300 m/s using velocities from 2D Ultra-high resolution Multichannel Seismic data over the Algeria to Sardinia basin centre (2). • 3500 m/s is reported from velocity observation in the Gulf of Lion (4).
Messinian Mobile Unit (MU)	4200 – 5100	• The Messinian salt velocity is reported from 4200 m/s in the Herodotus Basin to 4300 m/s in the Levant basin (5). • 5100 m/s is reported from seismic velocity analysis of profile MS-39 in the Western Mediterranean (3).
Messinian Lower Unit (LU)	3500 – 4200	• 3500 m/s is reported from velocity observation in the Gulf of Lion (4). • 4200 m/s is reported from seismic velocity analysis of profile MS-39 in the Western Mediterranean (3).
Early to Late Miocene (Pre-Messinian)	2700 – 5300	• 2700 m/s is a starting velocity in locations of carbonate build-up (5). • 5300 m/s is reported based on gradual increase in velocity from 4800 – 5300 m/s between Expanding Spread Profiles (ESP) 202 and 203 (1).

Table 5: Velocity range for Pre-Messinian, Messinian Salinity Crisis and Pliocene to Quaternary units. References: (1) Leroux et al., 2017; (2) GALSI project; (3) Dal Cin et al., 2016 (3); (4) Roveri, et al., 2014; (5) El-Bassiony et al., 2018.

A single representative lithology per unit is selected, using seismic stratigraphy and literature sources (Table 6). For the five units, the primary lithologies were marlstone, claystone, halite and gypsum. Marlstone was used for the pre-Messinian and Pliocene to Quaternary (P-Q) units, claystone for the MSC Stage 1 (Lower Unit), halite for the MSC Stage 2 (Mobile Unit), and gypsum for the MSC Stage 3 (Upper Unit).

		1-D Models									
Property	**Units**	**Early to late Miocene (Pre-Messinian)**		**MSC Lower Unit (LU)**		**MSC Mobile Unit (MU)**		**MSC Upper Unit (UU)**		**Pliocene to Quaternary (PQ)**	
		A-B	**L-P**	**A-B**	**L-P**	**A-B**	**L-P**	**A-B**	**L-P**	**A-B**	**L-P**
Seismic depth thickness range	m	418 - 775	553-1087	-	612-840	198 - 255	758-921	171 - 193	550 – 621	220 - 347	1000 – 1575
Pre-compacted thicknesses	m	579	740	-	661	241	933	190	646	286	1480
Modelled thickness present-day	m	567 (1)	705 (1)	Absent (1)	630 (1)	236 (1)	888 (1)	187 (1)	615 (1)	280 (1)	1409 (1)
Time duration	Ma	14 (4)	10 (4)	-	0.37 (5)	0.05 (5)	0.05 (5)	0.22 (5)	0.22 (5)	5.33 (5)	5.33 (5)
Dominant Lithology	-	Marl (3)	Marl (7)	-	Clay/ limestone (11)	Halite (12)	Halite (12)	Gypsum (12)	Gypsum (12)	Marl (6)	Marl (7)
Compressible initial porosities at seabed	%	30 (10)	30 (10)	-	30 (10)	2.0 (1)	2.0 (1)	3.0 (1)	3.0 (1)	30 (10)	30 (10)
Average grain density	g cm^{-3}	2.65 (8)	2.65 (8)	-	2.68 (8)	2.13 (1)	2.13 (1)	2.32 (1)	2.32 (1)	2.65 (8)	2.65 (8)
Permeability at seabed	m^2	10^{-17} (9)	10^{-17} (9)	-	10^{-17} (9)	10^{-20} (2)	10^{-20} (2)	10^{-18} (1)	10^{-18} (1)	10^{-17} (9)	10^{-17} (9)
Initial compaction factor	km^{-1}	0.4 (1)	0.4 (1)	-	0.4 (1)	0.1 (1)	0.1 (1)	0.2 (1)	0.2 (1)	0.4 (1)	0.4 (1)

Table 6: Physical property parameters used in modelling the evolution of overpressure from Miocene to present-day for the Algero-Balearic (A-B) and Liguro-Provençal (L-P) models. Range of seismic depth thicknesses are a result of velocity uncertainty over the region. References: (1) this study; (2) Beauheim et al., 1991; (3) Burollet et al., 1978; (4) Carminati et al., 2011; (5) CIESM, 2008; (6) Hsü et al., 1978; (7) Leroux et al., 2017; (8) Mavko et al., 2009; (9) Neuzil, 1994; (10) Proshlyakov, 1960; (11) Roveri et al., 2001; (12) Roveri et al., 2014.

Duration of deposition of the modelled units from Miocene to Present is provided in Table 6. Duration of deposition in our models for the pre-Messinian unit ranges from 14 Myr along the basin edge to 10 Myr in the deep central oceanic location (Carminati et al., 2011). The time durations in our models for the MSC units are 0.37 Myr for the LU, 0.05 Myr for the MU and 0.22 Myr for the UU, with no difference in time duration considered for the Messinian units between the basin edge and deep central oceanic model locations (CIESM., 2008).

Average fluid and solid properties and other modelling constants are provided in Table 7. We assume fully-water saturated sediment for all scenarios with initial seabed density and viscosity for water of 1028 kg m^3 and 0.0012 Pa s, respectively. For marlstone units we use an initial seabed porosity of 30% from claystone porosity trends (Magara, 1980), an initial compaction factor of 0.4 km^{-1} reported in Marin-Moreno et al. (2013) for similar sediments, an irreducible porosity of 10%, and a permeability at the seabed of 10^{-17} m^2 from porosity and permeability trends for argillaceous material (Neuzil, 1994). For evaporite units, we use an initial seabed porosity of 2.0 - 3.0%, an initial compaction factor of 0.1 - 0.2 km^{-1}, an irreducible porosity of 1.0%, and a permeability at seabed for the most likely scenario of 10^{-20} m^2 for halite and 10^{-18} m^2 for gypsum estimated from laboratory tests as part of this study.

Property	**Units**	**1-D Models**		**Reference**
		A-B	**L-P**	
Acceleration of gravity	m/s^2	9.80	9.80	Robinson et al. 1995
Seabed depth	m	2585	2638	this study
Seabed temperature	C	13	13	Manca et al. 2004
Thermal gradient	C/km	36	36	Erickson et al. 1978
Seabed water viscosity	Pa.s	0.0012	0.0012	IAPWS 2008
Seabed water density	kg/m^3	1028	1028	Iona et al. 2018
Fracture limit	Decimal	0.8	0.8	this study

Table 7: Physical constants assumed in the Algero-Balearic (A-B) and Liguro-Provencal (L-P).

We assume a seabed (top boundary) temperature of 13˚C, which corresponds to the estimated temperature at water depths of 2585 - 2638 m (Manca et al., 2004) and an average geothermal gradient of 36˚C km^{-1} (Erickson et al. 1978). The temperature is only used to calculate changes in pore fluid density and viscosity with depth. We impose boundary conditions of zero overpressure at the top of the models representing the seabed, and zero flow at the base of the models.

The mathematical model (eq. 8) is solved in Matlab (R2017) using an implicit finite difference scheme with backward differences to approximate the time derivative and second-order centered differences in space, an harmonic average to estimate the permeability in the interface between cells, and a fully compacted coordinate system for the depth axis (Marín-Moreno et al., 2013). The numerical model uses 400 to 800 cells in the z-direction and 800 to 1600 time steps per unit. We run the default model with different mesh sizes to assess their influence on our results and select the mesh size from which further refinement produced negligible changes.

2.5 Results

To evaluate the impact of sediment loading on overpressure generation and fluid release, we reconstruct the sedimentation history in the central oceanic portion of the Liguro-Provençal basin, where evaporite thicknesses are greatest, and at the base of the Emile Baudot Escarpment in the Algero-Balearic basin, where fluid release features have previously been observed (Figure 4).

2.5.1 Liguro-Provencal basin modelling

Figures 11 to 13 show the results of the Liguro-Provençal basin modelling.

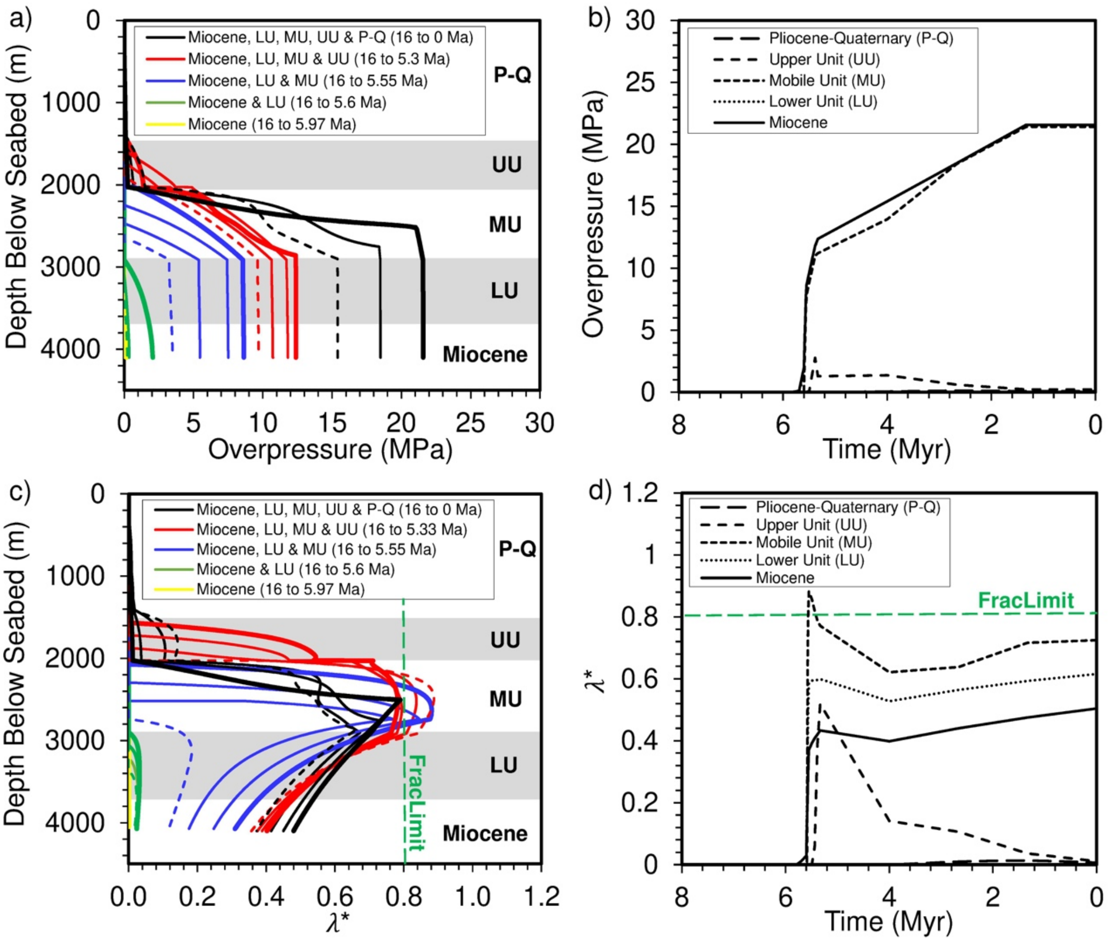

Figure 11: Most likely scenario of evolution of overpressure and λ* from Miocene to present-day for the Liguro-Provençal model (central oceanic location within the basin). (a, c) Overpressure and λ* evolution with depth and time for the deposition of a given unit with four equally divided subunits, where dashed lines correspond to the first time increment, thin solid lines correspond to second and third time increments, and bold lines correspond to end of deposition for a given unit. Results are presented relative to present-day depth. Yellow lines that represent deposition from 16 to 5.97 Ma are barely visible owing to near hydrostatic pressures in the marlstone. (b, d) Overpressure and λ* evolution with time for the five units modelled at the mid-thickness depth point for each unit. All models use a constant fracture limit of 0.8.

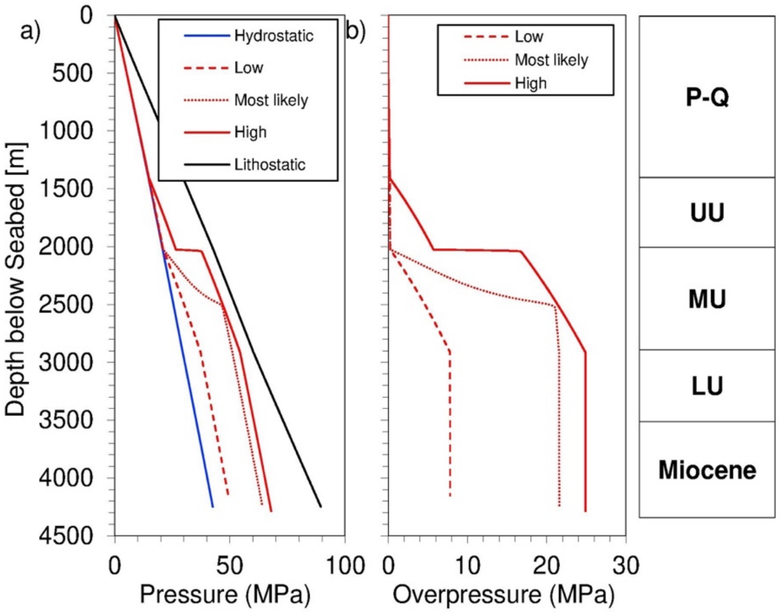

*Figure 12:*a) Present-day pressure and b) overpressure from seabed estimated for the Liguro-Provençal model. Red lines are uncertainty ranges. Results were calculated applying variation in fracture limit from 0.7 to 0.9 and permeability of evaporites from 10^{-17} to 10^{-21} m^2. The most likely scenario (red dotted line) uses a fracture limit of 0.8 and permeability of gypsum and halite of 10^{-18} and 10^{-20} m^2, respectively. The low value scenario (red dashed line) uses a fracture limit of 0.7 and permeability of gypsum and halite of 10^{-17} and 10^{-19} m^2, respectively. The high value scenario (red solid line) uses a fracture limit of 0.9 and permeability of gypsum and halite of 10^{-19} and 10^{-21} m^2, respectively. The column on the right side shows the five units modelled.

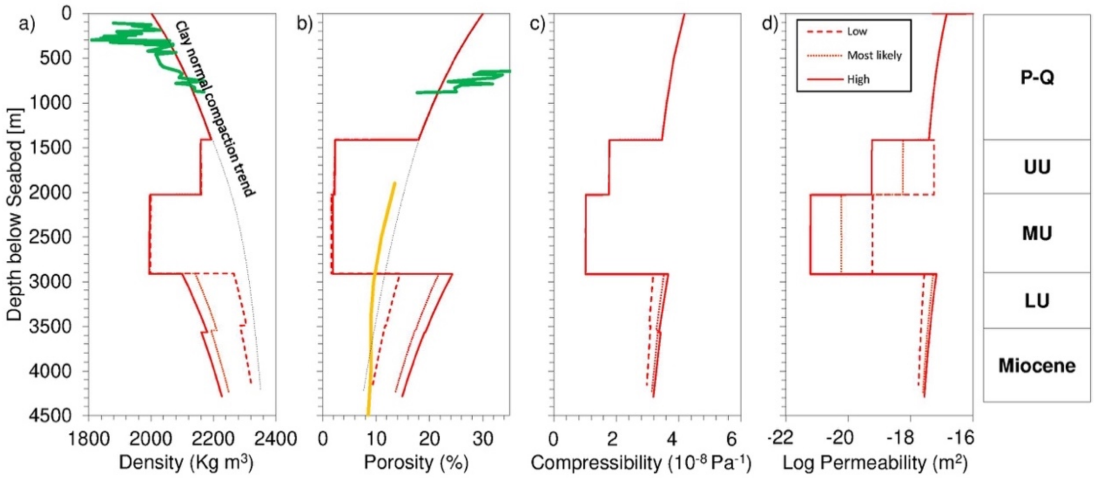

Figure 13: Present-day variations of density, porosity compressibility and permeability with depth for the Liguro-Provençal model. (a, d) Results were calculated applying variation in fracture limit from 0.7 to 0.9 and permeability of evaporites from 10^{-17} to 10^{-21} m^2. The most likely scenario (red dotted line) uses a fracture limit of 0.8 and permeability of gypsum and halite of 10^{-18} and 10^{-20} m^2, respectively. The low value scenario (red dashed line) uses a fracture limit of 0.7 and permeability of gypsum and halite of 10^{-17} and 10^{-19} m^2, respectively. The high value scenario (red solid line) uses a fracture limit of 0.9 and permeability of gypsum and halite of 10^{-19} and 10^{-21} m^2, respectively. The column on the right side shows the five units modelled. Data from (DSDP) 372 (green lines) and GLP-2 (orange line) are included for comparison with our results. Sonic derived claystone porosity from GLP-2 represents claystone porosity with depth, unaffected by loading of a thick basin-centre evaporite.

Deposition from 16 - 5.97 Ma

Commencing in the Middle Miocene (Pre-Messinian; yellow lines), deposition of 740 m of marlstone (16 - 5.97 Ma; sedimentation rate 74 m Myr^{-1}) allowed pore fluid dissipation to near hydrostatic pressure within the marlstone itself.

Deposition from 16 - 5.6 Ma

Following sediment loading of 661 m of claystone and limestone as part of Stage 1 (Lower Unit) of the MSC (5.97 - 5.6 Ma; sedimentation rate 1786 m Myr^{-1}), overpressure of 2.1 MPa was generated within the underlying pre-Messinian sediment (green lines).

Deposition from 16 - 5.55 Ma

The impact on overpressure is greatest during Stage 2 (Mobile Unit) of the MSC when the peak of the crisis was reached. Following sediment loading of 933 m of halite as part of Stage 2 of the MSC (5.6 - 5.55 Ma; sedimentation rate 18660 m Myr^{-1}), overpressure increases to 8.6 MPa within the halite and sediments of MSC Stage 1 and pre-Messinian (blue lines). Towards the end of MSC Stage 2, loading brought on by deposition of a thick basin-centre halite caused overpressure and λ^* to increase above a point at which hydro fracturing may have occurred, resulting in overpressure release from within the halite.

The effect of hydro fracturing is best represented during deposition of the halite of MSC Stage 2 (Figure 11a) where the increment in overpressure increases uniformly between the first to third sub-unit time intervals (thin blue dashed line to thin blue solid line) prior to hydro fracturing. Once the system fractures, overpressure dissipates at a faster rate as seen by the increase in the overpressure gradient between the third to fourth sub-unit time intervals (thin blue solid line to thick blue solid line). In response to hydro fracturing, overpressure and λ^* reduce but there is a time delay to respond to the new hydrodynamic conditions. The delay in the reduction of λ^* can be seen in the MSC Stage 2 halite (Figure 11b; thick blue line to thin solid red lines), which is caused by the time it takes for fluid flow to react to the new higher permeability developed by hydro fracturing and reduce overpressure and λ^* within and below that unit.

The effect of permeability on our scenarios show that the most likely and high scenarios give similar results in terms of pore pressure within the halite using permeabilities of 10^{-20} and 10^{-21} m2, respectively (Figure 12). This means that for permeabilities lower than 10^{-20} m^2, differences in pore pressure are small.

Deposition from 16 - 5.3 Ma

After the peak of the MSC, MSC Stage 3 is characterized by deposition of 646 m of Upper Unit gypsum (5.55 - 5.3 Ma; sedimentation rate 2936 m Myr^{-1}) contributing to further loading of underlying evaporitic units with overpressure increasing to 11.2 and 12.4 MPa within the base of the MSC Stage 2 halite and pre-Messinian units, respectively (red lines).

Deposition from 16 Ma – present day

Following the MSC, deposition of 1480 m of marlstone during the Pliocene-Quaternary (5.3 Ma to present day; sedimentation rate 278 m Myr^{-1}) allowed pore fluid to dissipate to near hydrostatic pressure within the MSC Stage 3 gypsum and the Pliocene to Quaternary (black lines). However, below the MSC Stage 2 halite seal with present-day λ^* near hydro fracture conditions, overpressure up to 21.6 MPa is retained within the pre-Messinian sediment. The present-day overpressure that remains is located below 1409 m where porosity deviates from the clay normal compaction trend (Figure 13) as is expected during disequilibrium compaction. In Alger-1, (DSDP) Sites 134, 371 and 372 and (ODP) Site 975, the Pliocene to Quaternary (P-Q) overburden sediments are dominated by deposition of marlstone with various mixtures of sand, silt and claystone, while GLP-2 is dominated solely by carbonated claystone. When comparison is made to the sedimentation rate versus fluid retention depth relationship for silt, silty claystone and claystone from global data (Swarbrick, 2012), assuming a sedimentation rate of 278 m Myr^{-1}, and “silty” lithology, we would expect top of overpressure to begin near the base of our P-Q unit. This is consistent with our estimates and hydrostatic pressures maintained to 2000 m depth below the seabed in wells like Andalucia-G1 (Fernandez-Ibanez et al. 2017). Applying the same sedimentation rate and an alternative “silty shale” lithology, we would expect top of overpressure to occur at depths anywhere from ~900 m below seabed to near base of our P-Q unit based on global equivalent examples of sedimentation rate.

2.5.2 Algero-Balearic basin modelling

Figures 14 to 16 show the results of the Algero-Balearic basin modelling.

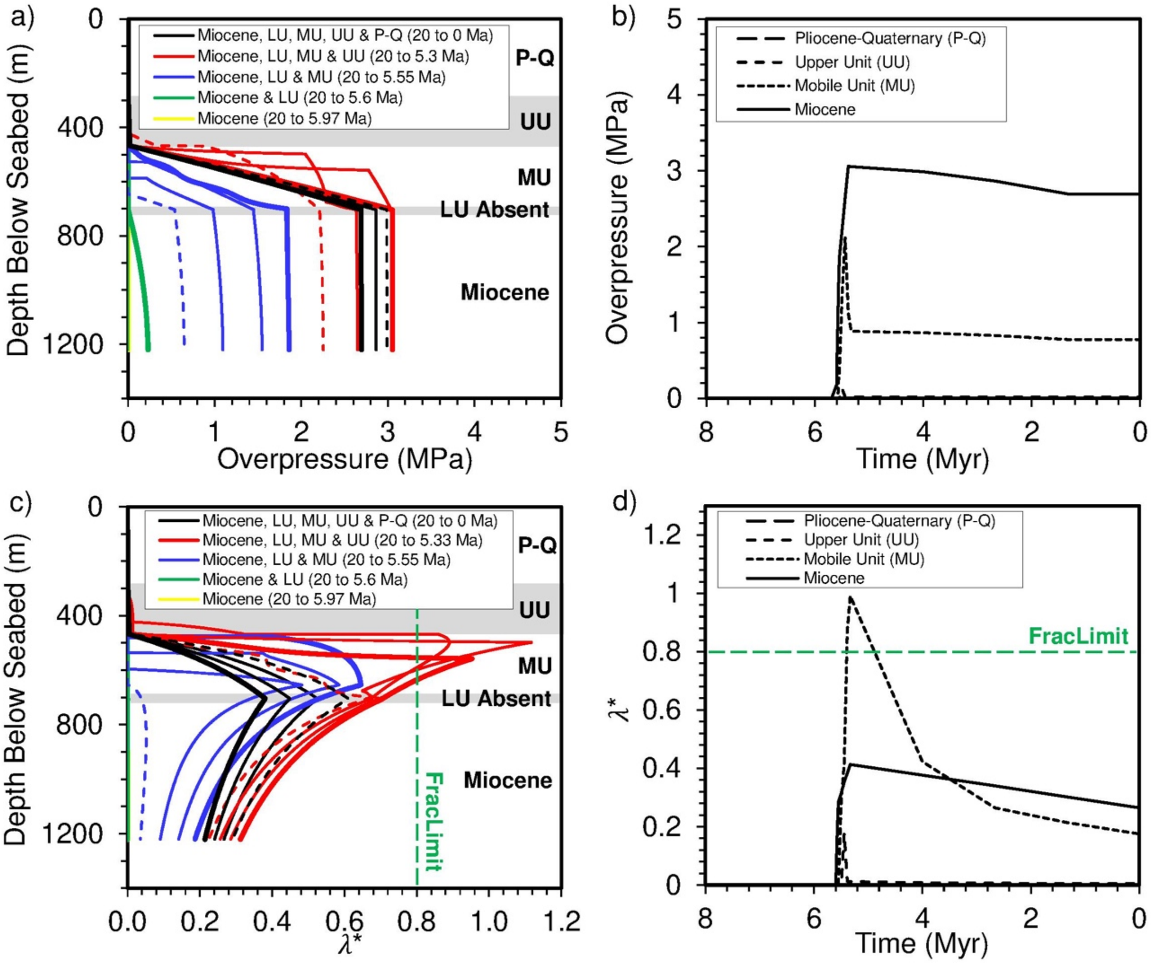

Figure 14: Most likely scenario of evolution of overpressure and λ* from Miocene to present-day for the Algero-Balearic model (at the base of the Emile Baudot Escarpment). (a, c) Overpressure and λ* evolution with depth and time for the deposition of a given unit with four equally divided subunits, where dashed lines correspond to the first time increment, thin solid lines correspond to the second and third time increments, and bold lines correspond to the end of deposition for a given unit. Results are presented relative to present-day depth. Yellow lines that represent deposition from 16 to 5.97 Ma are barely visible owing to near hydrostatic pressures in the marlstone. (b, d) Overpressure and λ* evolution with time for the four units modelled at the mid-thickness depth point for each unit. All models use a constant fracture limit of 0.8.

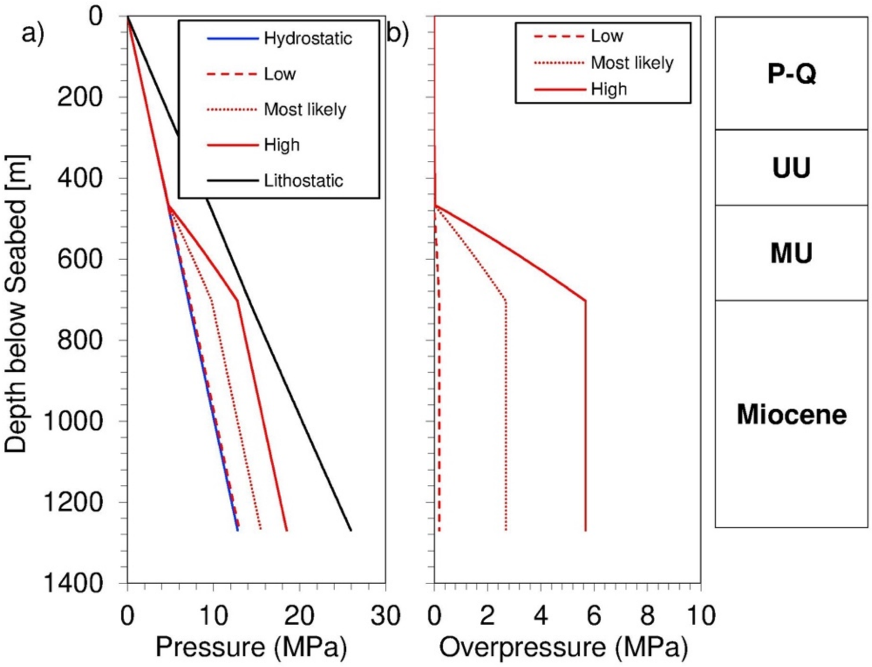

Figure 15: a) Present-day pressure and b) overpressure from seabed estimated for the Algero-Balearic model. Red lines are uncertainty ranges. Results were calculated applying variation in fracture limit from 0.7 to 0.9 and permeability of evaporites from 10^{-17} to 10^{-21} m^2. The most likely scenario (red dotted line) uses a fracture limit of 0.8 and permeability of gypsum and halite of 10^{-18} and 10^{-20} m^2, respectively. The low value scenario (red dashed line) uses a fracture limit of 0.7 and permeability of gypsum and halite of 10^{-17} and 10^{-19} m^2, respectively. The high value scenario (red solid line) uses a fracture limit of 0.9 and permeability of gypsum and halite of 10^{-19} and 10^{-21} m^2, respectively. The column on the right side shows the four units modelled.

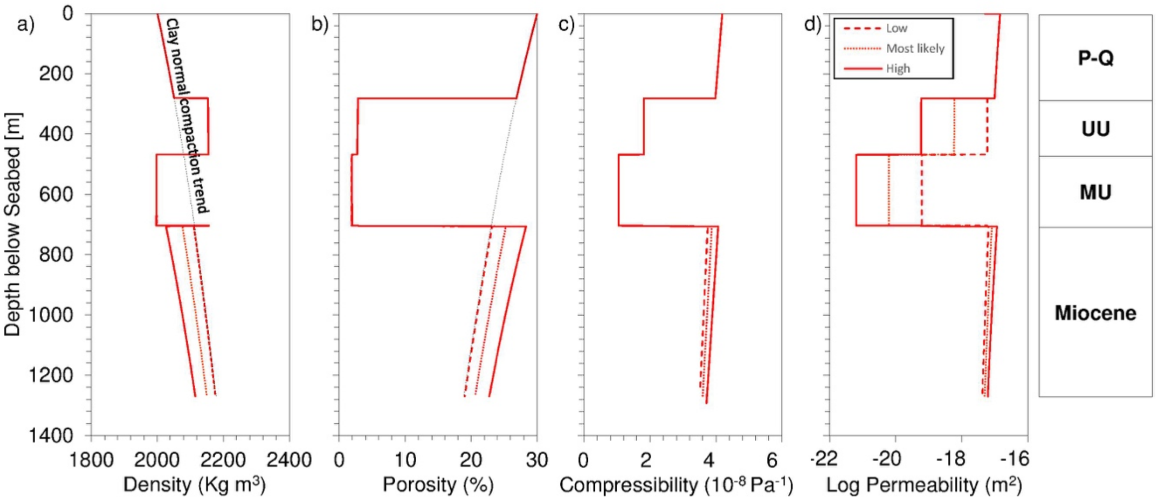

Figure 16: Present-day variations of density, porosity compressibility and permeability with depth for the Algero-Balearic model. (a, d) Results were calculated applying variation in fracture limit from 0.7 to 0.9 and permeability of evaporites from 10^{-17} to 10^{-21} m^2. The most likely scenario (red dotted line) uses a fracture limit of 0.8 and permeability of gypsum and halite of 10^{-18} and 10^{-20} m^2, respectively. The low value scenario (red dashed line) uses a fracture limit of 0.7 and permeability of gypsum and halite of 10^{-17} and 10^{-19} m^2, respectively. The high value scenario (red solid line) uses a fracture limit of 0.9 and permeability of gypsum and halite of 10^{-19} and 10^{-21} m^2, respectively. The column on the right side shows the four units modelled.

Deposition from 20 - 5.97 Ma

Commencing from the Early Miocene (Pre-Messinian; yellow lines), deposition of 579 m of marlstone (20 to 5.97 Ma; sedimentation rate of 41 m Myr^{-1}) allowed pore fluid dissipation to hydrostatic pressure.

Deposition from 20 - 5.6 Ma

Assuming the Lower Unit of MSC Stage 1 is absent along the edge of the basin (1 m inferred, 5.97 to 5.6 Ma; sedimentation rate of 2.7 m Myr^{-1}), hydrostatic pressure conditions persist to 5.6 Ma (green lines).

Deposition from 20 - 5.55 Ma

Following sediment loading of 241 m of halite as part of Stage 2 (Mobile Unit) of the MSC (5.6 to 5.55 Ma; sedimentation rate of 4820 m Myr^{-1}), overpressure increases to 1.9 MPa within the MSC Stage 2 halite and pre-Messinian sediments (blue lines).

Deposition from 20 - 5.3 Ma

The impact on overpressure is greatest during MSC Stage 3 when sediment loading of 190 m of Upper Unit gypsum (5.55 to 5.3 Ma; sedimentation rate of 864 m Myr^{-1}) increases overpressure to 3.1 MPa within the MSC Stage 2 halite and pre-Messinian sediments (red lines). Towards the end of the MSC Stage 3, loading brought on by deposition of the Upper Unit gypsum caused overpressure and λ^* of the underlying MSC Stage 2 halite to increase above a point at which hydro fracturing may have occurred, resulting in overpressure release from within the MSC Stage 2 halite.

Deposition from 20 Ma – present day

Following the Messinian Salinity Crisis, deposition of 286 m of marlstone during the Pliocene-Quaternary (5.3 Ma to present day; sedimentation rate of 54 m Myr^{-1}) allowed pore fluid to dissipate by up to 2.6 MPa within the MSC Stage 2 halite and pre-Messinian sediment (black lines).

2.5.3 Sensitivity of the model to common halite properties

We evaluated the impact of uncertainty in initial seabed porosity, permeability and sedimentation rate on overpressure development during halite deposition (Figure 17), as this is the primary unit contributing to the major increase in λ^* (Figure 18). We considered halite thicknesses of 200-1000 m, the latter based on thickness estimates of 600-1000 m from seismic interpretation of the WM stratigraphy, and a depositional time of 50 kyr (Topper et al. 2011; Roveri et al. 2014).

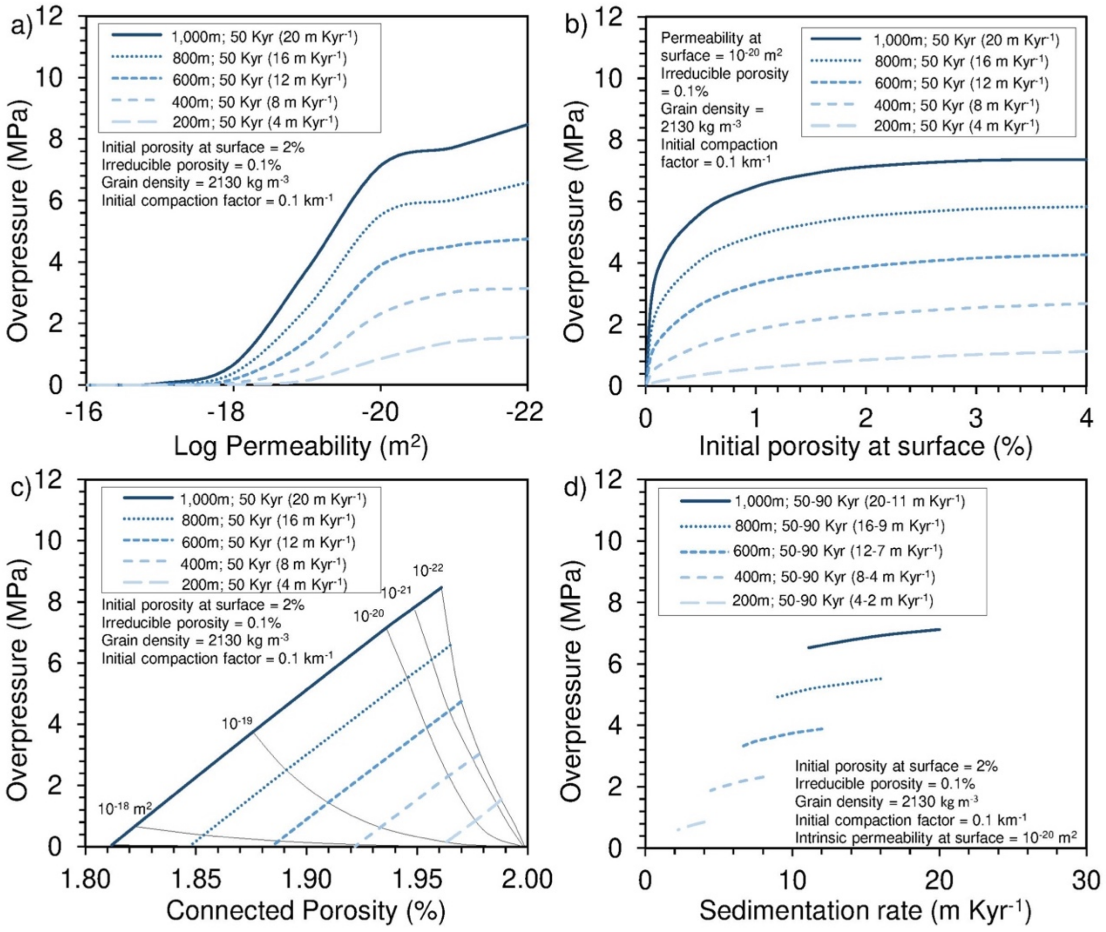

Figure 17: Influence of rock properties on overpressure generation within Messinian halite with thickness of 200-1000 m. Overpressure change in halite with (a) seabed permeability ranging from 10^{-16} to 10^{-22} m^2 and (b) seabed porosity ranging from 0.1 to 4.0%. c) Overpressure and connected porosity in halite for permeabilities ranging from 10^{-18} to 10^{-22} m^2. d) Overpressure changes with historical ranges in duration of the acme of the Messinian Salinity Crisis at 50-90 kyr.

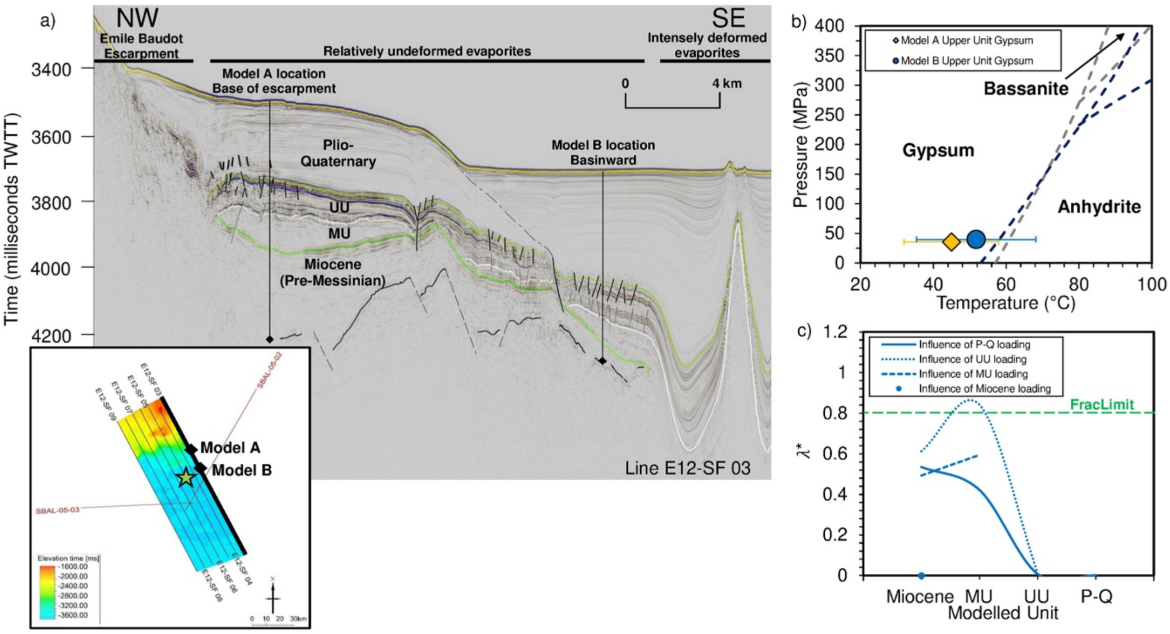

Figure 18: Comparison between gypsum and anhydrite reaction and disequilibrium compaction as possible mechanisms explaining observed fluid escape features in the Algero-Balearic basin. a) Seismic profile E12-SF 03 showing location of 1-D overpressure models, and interpreted horizons and faults. Inset showing the location of Algero-Balearic seismic profiles (black lines) and 1-D overpressure models evaluated in this study. Note that the Lower Unit (LU) is absent in this location. Green star shows the location of possible evaporite diagenesis and a fluid flow feature from Bertoni et al. (2015). b) Pressure and temperature phase diagram for gypsum-bassanite-anhydrite with dehydration boundaries by Klimchouk et al. (1996; dashed dark grey line) and Peter (2008; dashed dark blue line). Circle and diamond show, with uncertainty bars, the P-T conditions of the Algero-Balearic Upper Unit Gypsum relative to the boundaries of the dehydration reaction. Note that pressure includes the weight of 2585 m water column while temperature includes a 13°C seabed temperature. c) Maximum λ* evolution for the basin-ward units modelled at the end of deposition of each of the interpreted units.

We used halite permeabilities of 10^{-16} - 10^{-22} m^2 based on global literature ranges, derived from a combination of laboratory tests, modelled and inferred values, and our experimental data. Halite permeabilities above 10^{-17} m^2 generate hydrostatic pressures. Hence, for the low overpressure scenario with a fracture limit of 0.7 and the highest halite permeability of 10^{-19} m^2, if the overpressure exceeds the fracture limit, our assumed permeability increase of two orders of magnitude results in a halite permeability of 10^{-17} m^2, which is the threshold above which permeability does not influence our results. When the permeability drops below a threshold of about 10^{-18} m^2, halite with thickness greater than 600 m develops overpressure above 1 MPa. In contrast, halite with thickness of 200 m requires permeability below 10^{-20} m^2, to generate and maintain the same overpressure magnitude. This two orders of magnitude difference in threshold permeability is related to the ability of permeability to dissipate overpressure for a given length scale and time scale. In our 1-D models, for the same time scale, the thinner the layer the shorter the distance the fluid needs to travel to dissipate overpressure, and so the lower the permeability needed to generate and maintain the same amount of overpressure. For halite thicknesses of 600 - 1000 m, a permeability of 10^{-20} m^2 develops overpressure within the range 3.9 - 7.1 MPa. Below 10^{-21} m^2, that being the permeability of pristine, undamaged halite, overpressure for a 1000 m halite remains high at 7.7-8.5 MPa. When comparison is made for permeability ranges of 10^{-20} - 10^{-22} m^2, minor variation in overpressure, up to 1.3 MPa, is obtained.

Shallow halite layers such as that of Quaternary halite in the Saline Valley, CA display low porosities (<10% at 10 m below ground level) and tightly cemented layers below a depth of 45 m (Casas et al. 1989). In our study, lower connected porosities of 1.0 - 2.7% were obtained from laboratory testing of shallow Messinian halite collected in Sicily. Integrating literature sources and our laboratory measurements of porosity, we tested the impact of uncertainty in initial halite seabed porosity of 0.1 - 4.0% on overpressure. For an initial seabed porosity of 1.0%, a significant increase in overpressure up to 6.5 MPa is obtained for a 1000 m thick halite. For initial seabed porosities above 1.0%, overpressure plateaus with only minor increase in overpressure by about 0.9 MPa.

There is considerable uncertainty concerning the stratigraphic framework for the MSC evaporites, as well as their absolute chronostratigraphy in the deep basins owing to limited well control, lack of chronostratigraphic constraint, studies not structured within a regional context and scientific debate on the origin of the evaporites (Hardie et al. 2004; Krijgsman et al. 1999). Accounting for the uncertainty in stratigraphic models for the MSC, we test the impact of sedimentation rate on overpressure, using halite thicknesses of 200 - 1000 m and total duration of Messinian halite deposition of 50-90 kyr. For duration of deposition of 50 - 90 kyr and halite thickness of 1000 m (sedimentation rates 11-20 m kyr^{-1}), a minor difference in overpressure, up to 0.6 MPa, is obtained. Halite with a lower thickness of 200 m and the same duration of deposition (sedimentation rates 2-4 m kyr^{-1}) show even lower magnitude difference in overpressure, of 0.25 MPa.

2.5.4 Sensitivity of the model to downward fluid migration

We evaluated the impact of downward fluid migration from pre-Messinian sediment into basement rock and the effect of permeability variation of pre-Messinian sediment on this type of migration. To do this, we assumed a highly fractured basement rock by imposing a zero overpressure bottom boundary condition. Although the nature of the basement in the

Mediterranean is variable, we expect there to be oceanic crustal igneous rock in the Liguro-Provençal basin where our model is located (Figure 4.; Sabat et al., 2018)). If a boundary condition of zero overpressure is imposed at the base of the model representing full dissipation through the basement, the ability to retain overpressure within pre-Messinian units depends largely on its permeability which is poorly constrained. We tested pre-Messinian permeabilities of 10^{-17}- 10^{-22} m^2 (Neuzil, 1994) reasonable values at porosities of 2 - 14% based on claystone compaction trends at a depth of ~4000 m (Allen, et al., 2013). For downward flow and permeability of 10^{-17} m^2, present-day overpressure is near hydrostatic pressures within the pre-Messinian sediment. For permeability lower than 10^{-19} m^2 overpressure develops, which increases mid-unit up to 32.2 MPa (λ* of 0.75) for a permeability of 10^{-22} m^2. Below this at the boundary between pre-Messinian and basement, a regression in overpressure to hydrostatic conditions is modelled (Figure 19).

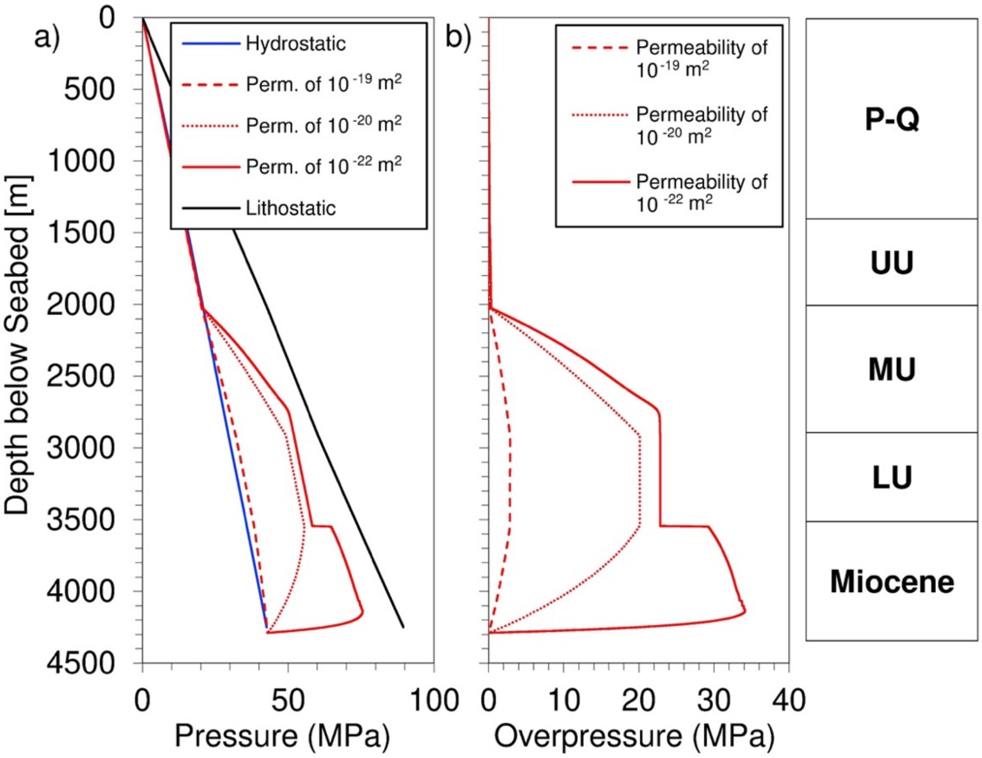

Figure 19: a) Present-day pressure and b) overpressure from seabed estimated for the Liguro-Provençal model with downward fluid migration possible through a hypothetical fractured basement rock. Red lines are uncertainty ranges accounting for Miocene (Pre-Messinian) permeabilities of 10^{-19} m^2 to 10^{-22} m^2. The column on the right side shows the five units modelled.

2.5.5 Gypsum dehydration to anhydrite

In the Algero-Balearic basin, polygonal faults have been interpreted within the upper evaporites of the MSC and lowermost Pliocene sequences, suggesting presence of past fluid expulsion and migration events (Bertoni et al., 2015). Tassy et al. (2018) interpret the polygonal faulting to be generated by overpressure induced by fluid from the gypsum to anhydrite dehydration process. Anhydrite has been cored before from the Upper Unit (UU) of (DSDP) Site 371 in the Algero-Balearic Basin, however the well was drilled in a zone where numerous shallow magnetic anomalies and a thin veneer of evaporites are present (Figure 4; Hsü et al., 1978). To understand if gypsum dehydration occurs in the location of the SALTFLU seismic data, we first evaluate pressure and temperature conditions of the Upper Unit gypsum at the base of the Emile Baudot Escarpment (Figure 4; Figure 18a Model A location) relative to the boundaries of the dehydration reaction (Figure 18b). Using the parameters described above (section 4), we show that the Upper Unit of gypsum at the base of the Emile Baudot Escarpment is unlikely to reach the pressure and temperature conditions required for gypsum-anhydrite transformation. Considering thicker basinward units on the lowermost slope of the continental rise (Figure 4 green star on strike direction and in close proximity with Figure 18a Model B location), fluid release from evaporitic dehydration is possible if heat flow exceeds 105 mW m^{-2} in combination with low thermal conductivities for marlstone and gypsum of 1.5 and 1.0 W m^{-1} K m^{-1}, respectively. However, these low modelled thermal conductivities are inconsistent with higher values obtained during (DSDP) Leg 42A (Erickson et al., 1978). Alternatively, our disequilibrium compaction models suggest that sediment loading over the 5.55 - 5.33 Ma period can cause sufficient overpressure to hydro fracture the underlying MSC Stage 2 (Mobile Unit) halite (Figure 18c), allowing fluid to migrate into the Upper Unit of gypsum and leading to development of a polygonal fault system.

2.6 Interpretation and discussion

Our sensitivity analysis of evaporite petrophysical properties show that permeability is the dominant parameter controlling the generation of pore fluid overpressure. However, a broad range of permeability values are reported in literature (Figure 9) which reduces the predictive ability of overpressure from numerical models, as illustrated in our modelling of the MSC Stage 2 (Mobile Unit) halite. Laboratory measurements of permeability from high quality, undamaged evaporites from borehole cores is then essential to produce reliable predictions. When permeability measurements of representative evaporites under undisturbed conditions are not available, low (most likely) and high permeability overpressure modelling scenarios and the threshold above which permeability does not influence overpressure results should be provided (Figure 17).

Overpressure build-up up to hydro fracturing during the MSC has likely caused fluid expulsion events in the WM basin. Fluid expulsion related features are evident on seismic data with examples of mud volcanoes, pipes and polygonal faulting in sediments of the Central and Western Mediterranean (Bertoni et al., 2015). Using seismic-based evidence across the entire Mediterranean, a conceptual framework for timing of fluid expulsion during the MSC indicates three possible fluid flow stages, the first commencing in the early stage of the MSC before about 5.6 Ma, the second during deposition of MSC Stage 2 basin centre evaporites from 5.6 to 5.53 Ma, and the third during deposition of MSC Stage 3 (Upper Unit) evaporites from 5.53 to 5.33 Ma (Bertoni et al. 2015). To evaluate the role that evaporite deposition played on these three stages, we model overpressure applying a scenario of conservative values for fracture limit of 0.7, permeability for gypsum and halite of 10^{-19} and 10^{-21} m^2, respectively, and a high Stage 1 (Lower Unit) thickness of 1405 m, as observed on seismic data in the Gulf of Lion deep basin (Leroux et al., 2017) with an alternative low permeability evaporite scenario of gypsum. Our models show that sediment loading by this thickness of LU gypsum does not cause overpressure to increase above hydro fracturing in this first stage, from 5.97 to 5.6 Ma. From our modelling in the WM, we identify two possible timings of fluid expulsion events relative to the MSC, the first by sediment loading of Stage 2 (Mobile Unit) halite from ~5.58 to 5.55 Ma and the second by sediment loading of Stage 3 (Upper Unit) evaporites from ~5.55 to 5.33 Ma causing overpressure of the underlying MSC Stage 2 halite to increase above hydro fracturing. We therefore show that in the WM the fluid expulsion events triggered by an increase in overpressure above hydro fracturing likely started during and after deposition of Stage 2 halite (Mobile Unit). The former event timing during Stage 2 differs slightly from seismic observations of basin-centre pockmarks in the Eastern Mediterranean, described to have formed in the early stages of the MSC related to sea-level drop (Bertoni et al., 2015), while the latter event timing is consistent with brecciated limestone in Central Mediterranean outcrop and seismic observations of polygonal faulting in the Western Mediterranean, formed at the late stage of the MSC up to the early Pliocene (Bertoni et al., 2015; Iadanza et al., 2013).

The distribution and thickness of the Stage 1 Lower Unit in the Algero-Balearic basin is not entirely known, due to complex structures of salt deformation, erosion, and seismic imaging effects (Dal Cin et al. 2016). The Lower Unit appears absent on seismic line E12-SF03 in the Algero-Balearic basin at the base of the Emile Baudot Escarpment. To understand the impact of seismic unit thickness on our modelled sediment loading and overpressure generation, we apply a thickness for the Lower Unit of 73 m, representing the maximum estimated threshold for vertical resolution. This threshold was determined using a relationship between frequency, velocity, wavelength and resolution (Liner et al. 2019). For gypsum rock with compressional velocities of 5700 to 5800 m s^{-1} and dominant frequency of the seismic signal between 50 and 20 Hz, the theoretical thickness that can be resolved is estimated at 29 - 73 m. Our models show that during deposition of 73 m of LU gypsum 5.97 - 5.6 Ma, only low overpressure, of 0.4 MPa, is generated. Even if we assume erosion removed part of the LU gypsum and that a maximum thickness of 300 m may have been deposited 5.97 - 5.6 Ma (Lugli et al. 2010), then only low overpressure, of 0.95 MPa, is generated. We therefore show that for the Algero-Balearic basin at the base of the Emile Baudot Escarpment, sediment loading of the MSC Stage 1 (Lower Unit) 5.97 - 5.6 Ma played no role in overpressure increase above hydro fracturing and fluid release in the area.

2.7 Conclusions

We completed laboratory measurements to constrain properties of evaporite minerals as input to a series of 1-D disequilibrium compaction models. We conclude for the physical properties of Mediterranean evaporites that:

- Evaporite porosities lower than 3% can become connected by cracks and/or dilatancy of grain boundaries allowing fluid flow.
- Permeabilities of anhydrite and gypsum at different confining pressures range from 10^{-17} to 10^{-21} m^2.

We used a 1-D disequilibrium compaction model to reconstruct fluid flow through time and to quantify the magnitude of overpressure generated in the Western Mediterranean basin. For the Liguro-Provençal basin and Algero-Balearic basin we conclude:

- Permeability lower than 10^{-18} m^2 can cause overpressure within Messinian evaporites.
- Rapid sediment loading of low permeability Messinian evaporites inhibited vertical fluid flow causing high overpressure within pre-Messinian and Messinian sequences.
- Rapid sediment loading caused sufficient overpressure to hydro fracture MSC evaporites. Hydro fracturing may have occurred during Stage 2 deposition of halite (Mobile Unit) from about 5.58 to 5.55 Ma in the Liguro-Provençal basin, and during Stage 3 deposition of Upper Gypsum from 5.55 to 5.33 Ma in the Algero-Balearic basin.

- Fluid release features observed in seismic reflection data near the Emile Baudot escarpment of the Algero-Balearic basin, previously interpreted to be caused by gypsum-anhydrite transformation, can also be explained by disequilibrium compaction-related hydro fracturing.

Chapter 3 Quantifying overpressure and sea-level fall during the Messinian Salinity Crisis from pockmark genesis, Levant Basin, Eastern Mediterranean

At the onset of the Messinian Salinity Crisis (MSC) immediately preceding regional evaporites deposition, a field of pockmarks formed at the contemporaneous seafloor in the Levant Basin. These pockmarks were created by the excision of near-surface sediments during venting of methane gas from a Miocene (pre-Messinian) source, triggered by a substantial sea-level fall. However, constraints on the magnitude of sea-level change at this time are limited. Sea-level fall can significantly affect subsurface pressures when the sediment is saturated with a compliable gas such as methane. Using analytical modelling of fracture-dominated gas migration through sediments, we quantify the evolution of fluid pressure in Miocene sediment of the Levant Basin during the onset of the MSC and estimate possible magnitudes of sea-level fall that led to seal failure and migration of gas to the paleo-seafloor. Tensile fracturing of the seal overlying Miocene sediments partially saturated with methane occurs with sea-level falls of ~52-388 m, for overburden thicknesses 74 - 371 m, which reduced subsurface pressures by up to 1.4 MPa at the onset of the MSC. We propose that in the deep Eastern Mediterranean, the genesis of the pockmark field located at the base of the Messinian evaporites was triggered by sea-level falls of 10s to 100s of metres, that significantly reduced subsurface pressures during the initial stage of the MSC, resulting in tensile fracturing of Middle to Late Miocene sediment. Our results provide new constraints on mechanisms of overpressure creation and gas leakage in worldwide salt giant basins, which are dominated by large fluctuations of sea-level during their evolution.

3.1 Introduction

The Messinian Salinity Crisis (MSC) was a Mediterranean-wide event that led to dramatic changes in sedimentation and biota (e.g., Hsü, et al., 1973; Krijgsman et al., 1999; Manzi et al., 2013; Roveri et al., 2014), however the related changes in sea-level across the basin at various stages of the crisis remain widely debated. The development of high fluid overpressures in pre-Messinian sediment, large-scale methane venting and the formation of eruptive pockmarks on the paleo-seabed of the Eastern Mediterranean has been postulated to be due in part to the combination of sea-level fall at the onset of the crisis and the presence of a pre-Messinian (Oligocene to Miocene) biogenic petroleum system (Bertoni et al., 2013; Al-Balushi et al., 2016). Water level falls can result in significant fluid overpressuring and even the formation of supra-lithostatic fluid pressures, enhanced by the effects of gas in the sub-surface (Liu and Flemings, 2009; Hermanrud et al., 2013). Free gas increases the compressibility of the pore fluid and reduces the loading efficiency, that describes the portion of applied load supported by the pore fluid (Wang et al., 1998; Liu and Flemings, 2009). During sea-level fall, this may trigger geohazards (e.g., seafloor displacement and slope failure), and discharge of emissions into the atmosphere. Recent studies generally show that the largest sea-level falls in the Mediterranean related to the MSC took place towards the end of the crisis (Madof et al., 2019; Ryan, 2008). However, amplitudes and the duration of sea-level fall at the onset of the MSC remain uncertain, in particularly in the Eastern Mediterranean (Levant basin) where circumstantial evidence compatible with sea-level fluctuations (e.g., canyon incisions, acceleration of evaporation that led to the onset of basin-wide salt deposition, widespread methane emissions) does exist.

Fraser et al (2011) discuss the impact of the MSC on the petroleum system of the offshore Eastern Mediterranean, in the effect on the petroleum phase and seal capacity of removal of a water column in excess of 1000 m. Basin modelling and pore pressure evolution studies in the Eastern Mediterranean show that pore fluids of pre-Messinian sediment respond instantaneously to MSC-related water unloading and deposition of salt, when applying a 2070 m sea-level fall from 5.97 to 5.6 Ma (Al-Balushi et al., 2016). Al-Balushi et al. (2016) further suggests that the rapid heating of biogenic source rock during Messinian sea-level fall may have caused high gas generation rates, and the resulting free gas may have triggered fluid-related fracturing. Circular depressions (pockmarks) identified within and at the base of the Messinian evaporitic section on seismic reflection profiles in this area, suggest migration of fluid and discharge at the paleo-seafloor during a period of desiccation when sea-level was low

(Lazar et al., 2012). 3-D seismic mapping of crater-shaped depressions at the base of the Messinian evaporites provides further evidence of large-scale methane venting at the onset of the MSC (Bertoni et al., 2013). However, the values of sea-level fall and subsurface pressure conditions to form these pockmarks are not well constrained.

Here we adapt Cathles et al. (2010) analytical model of gas-related chimney formation to quantify the time evolution of pore fluid overpressure and mechanisms triggering gas migration from the Miocene sediment that can explain the pockmark field at the base of the Messinian evaporites in the Levant Basin Figure 20**.**

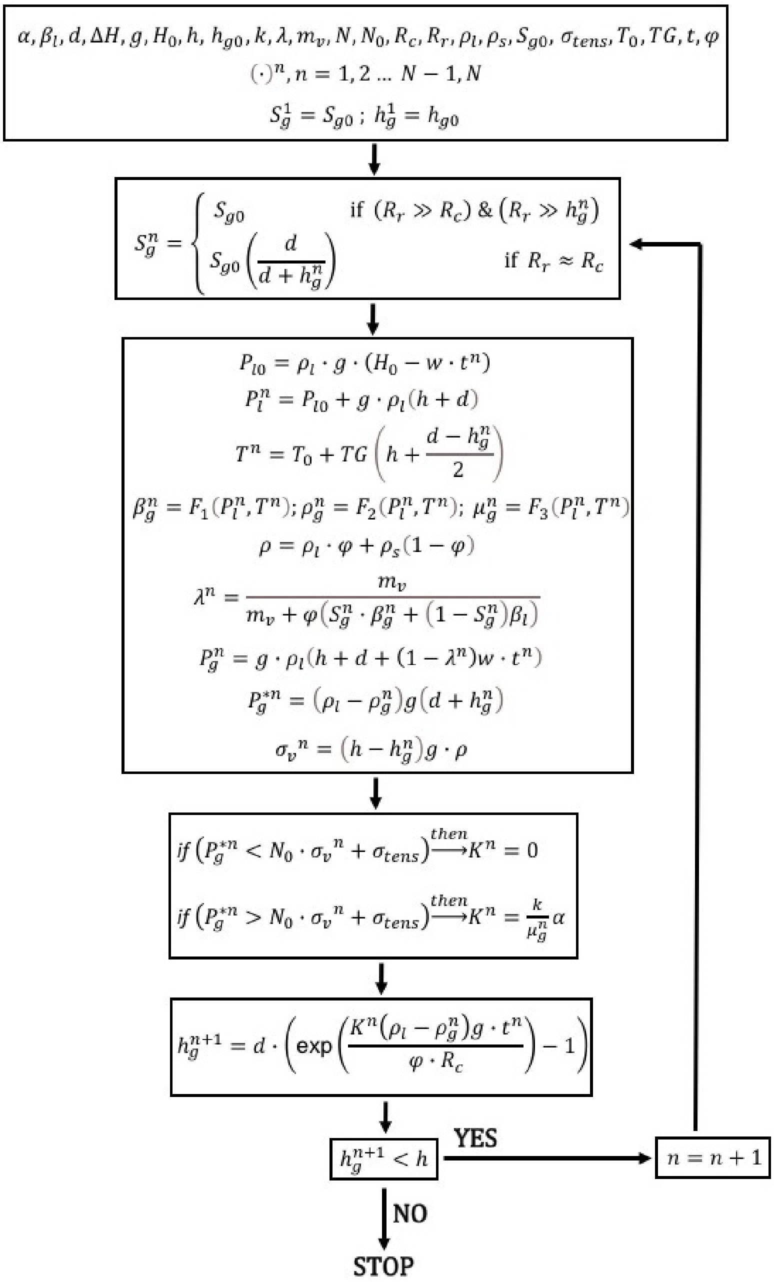

Figure 20: Governing equations and workflow for the analytical model.

The primary aim of this study is to test the hypothesis that the large crater pockmarks observed at the base of the Messinian evaporites may be caused by venting of methane gas accumulations in Miocene sediment towards the seafloor, triggered by sea-level fall at the onset of the MSC. We model an accumulation of methane gas trapped during the Early to Late Miocene in the Levant Basin, quantifying the initial overpressure generated by a given gas column of methane, the pore pressure evolution during sea-level fall, and the amount of sea-level fall and depth of reservoir from which seal failure likely occurred. Based on the modelling, we assess whether gas released to the seafloor likely originated from a shallow accumulation (Middle to Late Miocene submarine channel) or a deeper source (e.g., stratigraphic trap related to pinch-out of Early Miocene sands).

The study area is in the south Levant Basin in the Eastern Mediterranean (Figure 21). It is bounded to the north by the Cyprus Arc plate boundary, to the south and east by the African and Arabian coast, and to the west by the Eratosthenes Seamount (Gardosh & Druckman 2006; Barabasch et al., 2019).

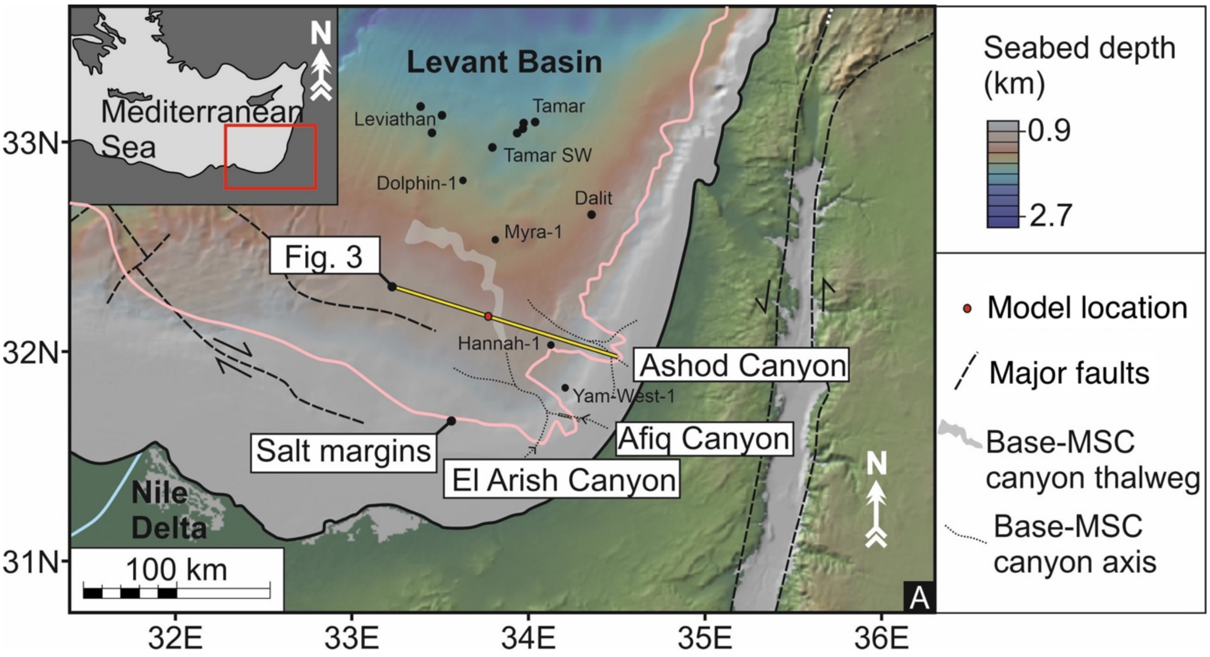

Figure 21: Tectonic and geographic setting of the study area. The model location represents the position of crater pockmark.

3.2 MSC sea-level

The timing and magnitude of sea-level fall during the MSC is controversial, with several studies suggesting that the onset of the MSC coincides with sea-level lowering (Butler et al., 1995; Clauzon et al., 1996; Riding et al., 1998; Rouchy and Caruso, 2006) while others suggest minor to no sea-level fall before massive halite deposition (Benson et al., 1991; Krijgsman et al., 1999, Govers, 2009; Lugli et al., 2010; Lugli, et al., 2015). The restriction of the Mediterranean may have been partially triggered by glacio-eustatic sea-level fall linked to climate cooling, generally accepted to have commenced at ca. 5.96 ± 0.02 Ma (Jimenez Moreno et al., 2013). Jimenez Moreno et al. (2013) estimate a sea-level fall up to ~227 m for the onset of the MSC, from analysis of benthic foram derived paleobathymetry from a drill core in southern Spain (Pérez-Asensio et al., 2012). Recent studies by Gvirtzman et al. (2022) estimate a MSC lowering of sea-level of 600 m (uncertainty range from ~550 – 750 m) by restoring the topography of the Messinian Nile canyon and the vertical position of the Messinian coastline by unloading post Messinian sediment (Gvirtzman, et al., 2022). In comparison, the models by Gargani et al. (2007) suggest that multiple short duration sea-level falls occurred, explaining the preservation of discontinuous paleo river profiles in the Western Mediterranean Basin and multiple erosional phases on seismic data in the Nile Delta (Eastern Mediterranean Basin). Evidence of a phase of sea-level lowering in the last stages of the MSC has also been observed in the Levant Basin (Madof et al., 2019; Ben Moshe et al., 2020). In this study we bring the story of sea-level further by using an analytical model to constrain the magnitude of sea-level change for the onset of the MSC in the deep Levant Basin, where publicly available drill core data is still limited.

3.3 Base-salt pockmarks

A number of crater-shaped depressions are imaged at the base of the Messinian salt sequence, in the region above the flanks of the pre-Messinian Afiq Canyon, on the 3D seismic surveys named ‘Levant’ and ‘Gal C’. (Bertoni et al., 2013; Figs. 22 and 23). The plan view geometry of these craters is circular or slightly elliptical, with diameters ranging from 100 to 2000 m (Figure 23). In the Gal C seismic survey, where the pseudo-well of this study’s model is located, a field of >15 smaller craters and an almost linear trail of 10 craters up to 2 km in diameter have been mapped, the best imaged of which is the Gal C crater (Bertoni et al., 2013; Figure 23). Crater-like depressions have only been observed at this stratigraphic level and at specific locations rather than throughout. The crater depth ranges from ~20 to more than 250 m (based on a seismic interval velocity (El-Bassiony et al., 2018). The crater morphology is best imaged in the larger craters, where it is entirely erosional with truncation of underlying Oligocene–Miocene reflections. The infill of the largest craters is composed of sparse reflections within the evaporite sequence, which onlap its flanks.

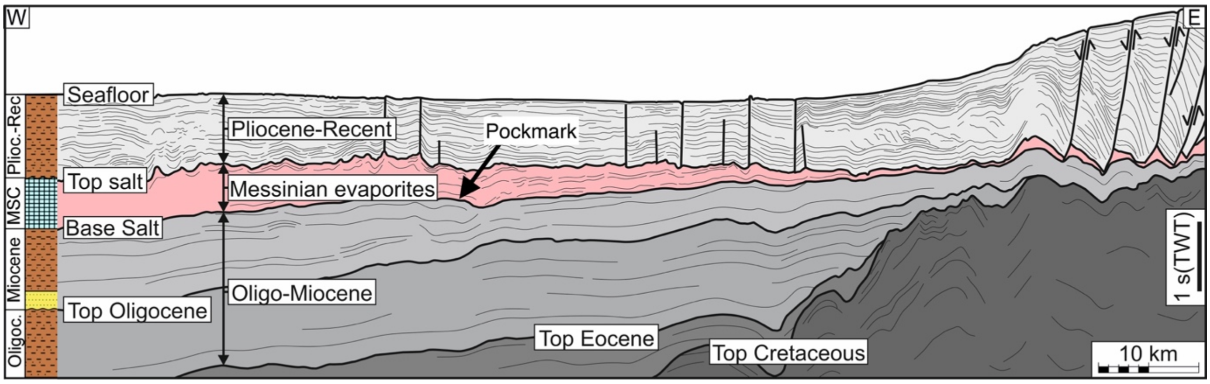

Figure 22: Stratigraphic interpretation over EMED-00-062 seismic line. Black arrow shows present-day location of crater pockmark, and our model location.

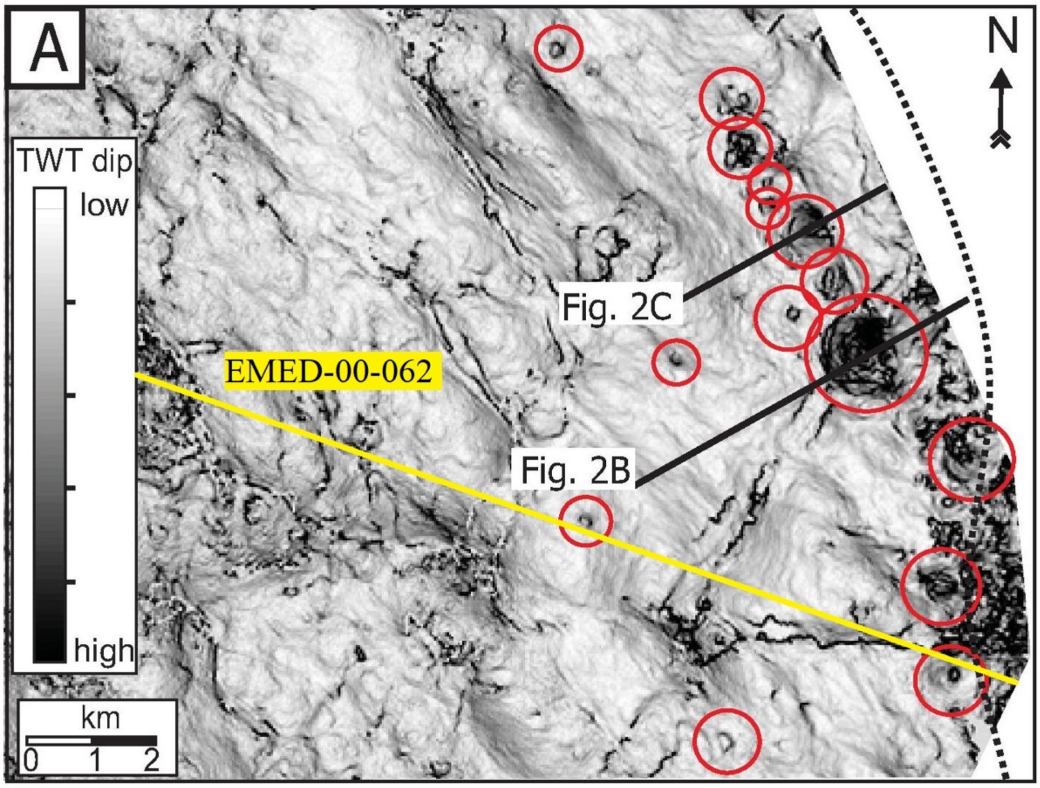

Figure 23: Subsurface time slice of southeast Gal C 3D seismic survey showing pockmark craters from Bertoni et al (2013; red circles). EMED-00-062 2D seismic line (solid yellow line) is shown covering our crater pockmark (modelled location; red circle in the centre of the image below Fig. 2B label). Fig. 2B and 2C indicate locations of seismic profiles from Gal C 3D seismic survey published in Bertoni et al. (2013) over the giant Gal C crater and smaller crater-like pockmark.

3.4 Seismic-Stratigraphic framework

The stratigraphic lithologies of the deep Levant Basin have been established by seismic facies analysis and calibrated to the nearby exploration wells Hannah-1, Myra-1 ST (side track) and Dolphin-1 (Meilijson et al., 2019; Ben-Gai, 2021). In this study, the focus of the stratigraphic framework is on Miocene successions relevant to our models (Figure 22).

The Early to Middle Miocene successions of the Levant basin is dominated by claystone and/or carbonate mudstone of deep-water middle to upper bathyal environment, characterised by discontinuous and low amplitude acoustic facies (Needham et al., 2017; Ben-Gai, 2021). The main gas discoveries in the Levant Basin, including Aphrodite, Leviathan and Tamar, host >40 Tcf of methane gas within folded Lower Miocene siliciclastic reservoirs. These reservoirs are composed of turbidite channels and basin-floor fans that are characterised by high-amplitude reflections (Gardosh & Druckman 2006; Al-Balushi et al., 2016; Needham et al., 2017).

Regionally, the Late Miocene sediment (pre-Messinian) are composed of cyclical alternations of claystone, sandstone and carbonate mudstone (Ben-Gai, 2021). In our study area the Late Miocene is characterised by discontinuous high amplitude reflections, where claystone, carbonate mudstone, and a series of small submarine channel fills have deposited downslope from the upslope incising El-Arish and Afiq canyons (Druckman et al., 1995; Bertoni & Cartwright, 2006). The Messinian Evaporites have a wedge-shaped geometry, thinning towards the continental margin. The Base Salt has continuous, high amplitude reflectors, with a negative impedance contrast and locally it truncates underlying reflections. Internally, the MSC unit is mostly composed of halite, which is seismically transparent and non-reflective (Al-Balushi et al., 2016; Meilijson et al., 2019), with several distinct reflective intra-salt layers. These intra-salt layers may be *in situ* or redeposited shelf clastics (Feng et al., 2016), carbonates, different evaporites (e.g., anhydrite, Mg-K salts), or diatomites (Al-Balushi et al., 2016; Manzi et al., 2018; Meilijson et al., 2019). The Top Salt is an acoustically hard reflection that is a regionally continuous unconformity that truncates intra-MSC reflections (Bertoni & Cartwright 2007; Gvirtzman et al., 2017; Kirkham et al., 2019).

3.5 Data

3.5.1 Boreholes, samples and seismic sections

Pre-stack time-migrated seismic reflection volumes (Gal C and Levant) were interpreted covering a total area of ~2,000 km^2 with bin size of 12.5 x 12.5 m, providing coverage of the deep-water extension of the Afiq canyon and basinal seismic stratigraphy. 2D seismic profile

EMED-00-062A was also examined to ascertain thicknesses (in time) of the Miocene (pre-Messinian and Messinian) and evaluate seismic facies around the crater pockmark modelling area (Figure 22).

Key marker horizons in the Oligo-Miocene Unit (Figure 22) have been depth converted using an average interval velocity of 2965 m/s by averaging the velocity values calculated from check shot surveys from 5 exploration wells in the Levant Basin (Gardosh & Druckman, 2006).

To constrain geophysical and petrophysical properties (p-wave velocity and permeability) of the Messinian evaporites, we evaluated seismic and well velocity data from literature (El-Bassiony et al., 2018) and from our laboratory experiments under dry conditions (Chapter 4) - we accept that measurements between seismic and ultrasonic, and under dry or wet conditions will vary. For our models, a single velocity of 4300 m/s was applied to the Messinian unit, the same salt velocity reported in the Levant Basin (El-Bassiony et al., 2018), and within the range of 4200 – 4500 m/s (seismic reflective layers) reported in areas south of the Levant Basin (Feng et al., 2016).

3.6 Modelling approach

3.6.1 Analytical model for the formation and propagation of gas overpressure-induced chimneys

The analytical model proposed in this study builds on Cathles et al. (2010) 1D analytical model of chimney formation caused by gas overpressure. Here gas overpressure is defined as the gas pressure above the liquid/water pressure of the system. The parameter definitions and the main equations are provided in Tables 8 & 9 and Figure 20. The model assumes the following:

(i) Upwards migration of the gas is due to buoyancy when the gas overpressure ($P_g - P_w$; in this work we use the term gas overpressure as an equivalent to capillary pressure) is higher than the sum of the minimum effective stress and tensile strength of the sediment (grain displacing, tensile fracture dominated invasion; e.g. Daigle et al., 2020).

(ii) The gas pressure at the top of the gas column is equal to the gas pressure at the base of the column. The gas pressure at the base of the column is equal to the pressure of the liquid/water (curvature of the gas-liquid interphase is zero; Fauria and Rempel, 2011);

(iii) Pore fluid overpressure develops due to sea level fall and it is estimated through the load efficiency concept (e.g. Liu and Flemings, 2009).

(iv) The load exerted by deposition of any Messinian evaporites during sea-level fall is negligible.

(v) Gas overpressure drops to zero at a distance of two times the chimney radius from the top of the chimney.

(vi) Dry (100% gas saturated) fractures based on observations from e.g. Algar et al. (2011) and Boudreau (2012) for gas propagation in soft, fine-grained, cohesive soils. To represent the formation of vertical fractures and gas migration through them, the absolute permeability of the chimney is increased (Table 9).

(vii) Two possible gas mass conservation cases: (a) in the unlimited gas reservoir, the amount of gas in the reservoir is significantly larger than the amount of gas that migrates through the chimney and so the saturation of gas along the chimney remains constant; (b) in the limited gas reservoir, the amount of gas in the reservoir is similar to that in the chimney, and hence the saturation of gas changes along the chimney. In this study we consider the unlimited gas reservoir case only.

Upward gas migration can also occur by capillary invasion, or porous flow, when the gas overpressure is larger than the capillary entry pressure, which depends on the pore size distribution and gas-liquid interfacial tension. The capillary entry pressure relates to gas saturation trough the capillary pressure curve (e.g., Daigle et al., 2020), so gas becomes mobile when the gas saturation reaches the gas percolation threshold, or critical gas saturation. If the gas becomes mobile before tensile fracturing occurs, then pressure may decrease. Here we assume that capillary invasion is limited for the type of materials in our study area, claystones and evaporites, with small pore sizes. Also, capillary invasion is not influenced by sea level change-induced pore pressure changes. Finally, chimney and pockmarks are generally associated with the development of overpressure-induced tensile fractures normal to the minimum principal stress (e.g. Cartwright & Santamarina, 2015).

Symbol	**Parameter**	**Units**
α	Permeability change factor due to fracturing	
β_g	Compressibility of the gas	Pa^{-1}
β_l	Compressibility of the liquid	Pa^{-1}
d	Thickness of the gas beneath the seal	m
d_g	Diameter of the sediment grain	m
g	Gravitational acceleration	m/s^2
H_0	Initial seabed depth	m
hss	Thickness of the sediment above seal	m
h_g	Height of gas chimney	m
h_{g0}	Initial height of gas chimney	m
K	Permeability coefficient	$kg\ m\ s^{-1}$

k	Intrinsic permeability	m^2
k_{rg}	Relative permeability of gas	
λ	Loading efficiency ratio	
m_v	Compressibility of the sediment	Pa^{-1}
μ_g,μ_l	Dynamic viscosity of gas (g) and liquid (l)	Pa^{-1}
N	Number time steps	
N_0	Coefficient of earth pressure at rest	
P_l	Liquid pressure at half thickness of gas column	Pa
P_{l0}	Initial liquid pressure at the seabed	Pa
P_c	Capillary Pressure	Pa
P_g	Gas pressure minus seabed liquid pressure	Pa
P^*_g	Gas overpressure (gas pressure above liquid pressure)	Pa
R_c	Radius of the gas chimney	m
R_r	Radius of the gas reservoir	m
R_e	Effective pore radius	m
ρ_g, ρ_l, ρ_s	Density of gas (g), liquid (l) and solid grains (s)	kg m^{-3}
S_e	Effective saturation of liquid	
S_g	Gas saturation in the gas column	
S_{g0}	Initial saturation of gas	
S_{gc}	Critical gas saturation	
S_{lr}	Residual liquid saturation	
σ	Liquid-gas interfacial tension	N m^{-1}
σ_{tens}	Tensile strength	Pa
σ_v	Vertical stress	Pa
T	Temperature at half thickness of gas column	°C
T_0	Temperature at the seabed	°C
TG	Geothermal gradient	°C m^{-1}
t	Time	s
w	Rate of sea level change	m s^{-1}
φ	Porosity	

Table 8: Symbols, definitions and units of parameters used in the calculations.

Parameter	**Units**	**Shallow scenarios**	**Deep scenario**	**References**
Gravitational acceleration	m s^{-2}	9.8	9.8	Robinson et al. (1995)
Type of gas used	-	CH_4	CH_4	Needham et al. (2017)
Methane density	$F_{CH4}(P,T)$			Setzmann, U., and W. Wagner (1991)
Seismic time thickness of the sediment overburden above seal	ms	50-250	800	This study. Deep scenario time thickness represents to top Oligocene marker
Overburden velocity	m s^{-1}	2965	2965	Gardosh & Druckman (2006)

Seismic depth thickness of the sediment overburden above seal	m	74-371	986	This study. Deep scenario depth thickness represents base Messinian to top Oligocene minus 200 m (equivalent to Early Miocene Tamar field sands)
Thickness of gas column beneath a seal	m	3	180	Estimated from Ben-Gai (2021) and Needham et al. (2017)
Initial height of gas flow in fluid channel	m	0	0	This study
Sediment porosity	-	0.58-0.47	0.29	Estimated from Kim and Lee (2018) based on trends from Giles (1997)
Intrinsic permeability	m^2	10^{-17} to 10^{-18}	10^{-19}	Estimated from Neuzil (1994)
Dynamic viscosity of liquid	Pa s	1.1x10^{-3}	1.1x10^{-3}	Lomax et al. (2001)
Liquid density	kg m^{-3}	1028	1028	Iona et al. (2018)
Solid grain density	kg m^{-3}	2650	2650	Mavko et al. (2009)
Compressibility of the liquid	Pa^{-1}	4.5x10^{-10}	4.5x10^{-10}	Estimated from Mavko et al. (2009) based on Bulk Modulus of water of 2.2 GPa.
Compressibility of the sediment	Pa^{-1}	1.5x10^{-8}	1.5x10^{-8}	Sawyer et al. (2008)
Coefficient of earth pressure at rest	-	0.9	0.9	Estimated from Needham et al. (2017)
Tensile strength	Pa	0	0	This study
Permeability change factor due to fracturing	-	2- and 4-order	2- and 4-order	This study
Radius of the gas chimney	m	100	100	This study; Cathles et al. (2010)
Liquid-gas interfacial tension	N m^{-1}	0.027	0.027	Vigil et al. (1994)
Initial saturation of gas	-	0.6	0.6	This study
Critical gas saturation	-	0.05	0.05	This study
Residual liquid saturation	-	0.3	0.3	This study
Seabed temperature	°C	13.6	13.6	Estimated from Manca et al. (2004)
Thermal gradient	°C m^{-1}	0.021	0.021	Estimated from Eckstein (1978) and Balkan et al. (2017); Macgregor (2018)

Initial seabed depth	m	1138	1138	This study
Sea-level fall gradient	m yr^{-1}	0.015	0.015	Estimated from Sternai et al. (2017)

Table 9: Physical parameters used in modelling gas overpressure generation and migration for the Early to Late Miocene periods for the Levant Basin (determined to be most likely values).

3.6.2 Modelling strategy and scenarios

We undertake modelling on two scenarios in the pre-Messinian at the location of the Levant Basin pockmarks: (1) shallow gas accumulations in small submarine channels (Middle to Late Miocene); and (2) a deep stratigraphic trap of Early Miocene sands similar to the Tamar field offshore Israel (see Figure 9 for depths and rock properties).

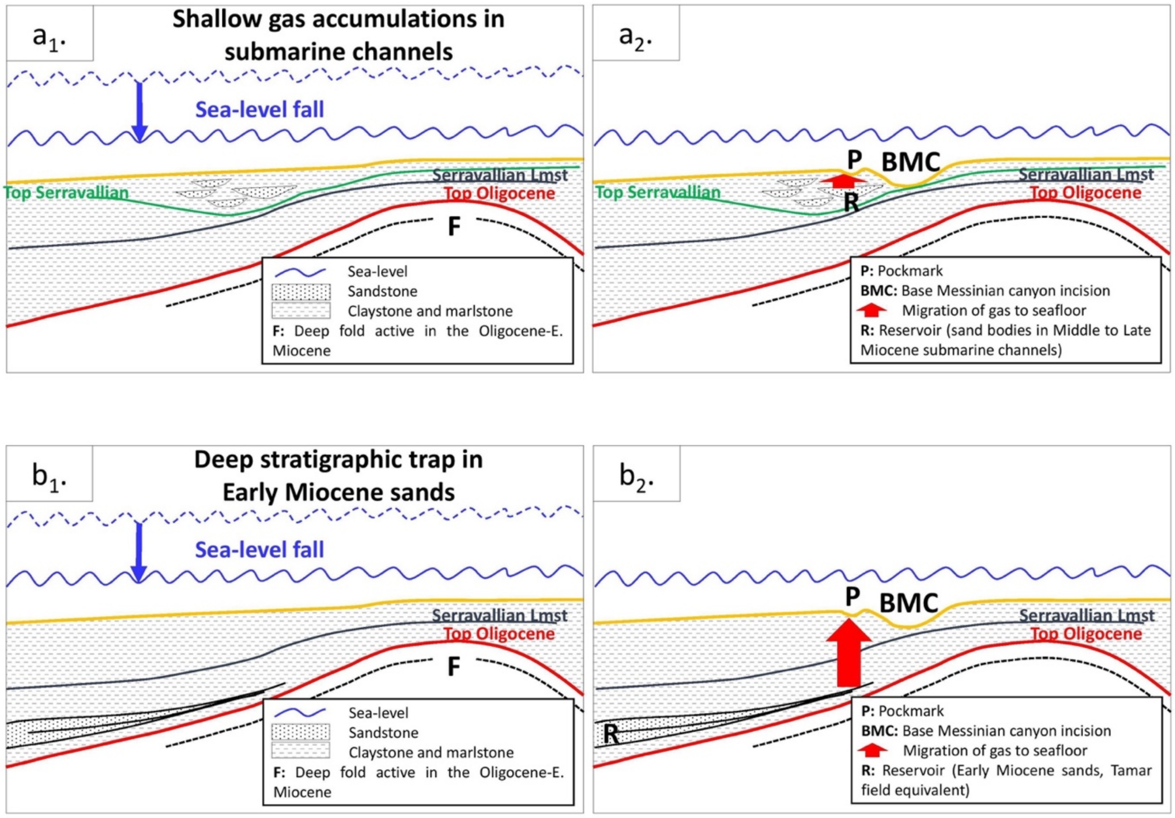

Figure 24: Schematic diagrams showing modelled scenarios in the development and propagation of gas overpressure-induced chimneys in the Levant Basin (prior to deposition of MSC units). a) Scenario of shallow gas accumulations in submarine channels of Middle to Late Miocene. b) Scenario of deep stratigraphic trap related to pinch-out of Early Miocene sands. a_1 and a_2 paleo-scenarios show the geological system prior to sea-level fall, while b_1 and b_2 show the features formed after sea-level fall and fluid migration.

(1) **Shallow middle to late Miocene submarine channel sands scenario** (Figure 24): The thalweg of the canyon is typically an erosional concave upward feature, with a vertical relief

of ca. 100 ms (>200 m in depth) at the base of the MSC evaporites (Figure 22), elongate in plan view, with a broadly meandering morphology (Figure 21; Bertoni & Cartwright, 2006). The thickness of the canyon deposits below the MSC unit is not well constrained and a clear canyon thalweg is not observed on 2D seismic lines below the base-MSC horizon. However, for an interval of ca. 200 ms (ca. 150 m using appropriate velocity values, chapter 4) below the base of the MSC unit, localised disruption of the overall continuous late Miocene reflections is observed, below and around the base-MSC canyon incision. In this area, the regionally continuous late Miocene reflections are truncated, and alternate with local discontinuous reflections with an asymmetrical concave upwards termination. This observation, if combined with the nearby submarine Afiq and El Arish canyon system (Bertoni & Cartwright, 2006; Druckman et al., 1999), strongly suggests the presence of submarine channels in the study area, as the distal expression of this canyon system (Figure 24), including in the pre-MSC late Miocene deposits.

(2) **Deep early Miocene sands scenario** (Figure 24): The study area is ca. 80 km south of the giant gas fields discovered offshore Israel (Tamar and Leviathan, Figure 21, and nearby discoveries). The reservoirs (Oligocene-Miocene) of these gas accumulations are well constrained and laterally continuous in the region (Needham et al., 2017). We therefore suggest that the same stratigraphic level could form a reservoir in our study area. However, while the traps of the Tamar petroleum system are faulted anticlines, there is no evidence of similar structures beneath the pockmarks in the study area. Alternatively, we propose a stratigraphic trap from pinch-out of early Miocene sands on the flanks of an anticline (Figure 24). The onlap terminations and growth pattern on this anticline show that it was active from the Oligocene to the early Miocene, and has no expression on the base of the MSC unit (Figure 24).

For both scenarios, we provide estimates of the gas overpressure required to overcome the tensile fracture threshold, the sea-level fall required to generate such fractures, and estimates for timing of fluid migration to the seabed after chimney initiation. We impose a sea-level fall of ~0.015 m/yr based on Eastern Mediterranean sea-level fall of ~1500 m between 5.7 – 5.6 Ma (Sternai et al., 2018). This value was selected as constraints on the magnitude and timing of sea-level change are limited. However, despite the uncertainty on timings and magnitudes of sea-level fall during the MSC, in our model the rate of sea-level fall only impacts the timing of fracture initiation and not the magnitude of sea-level fall required to initiate fracturing. To consider the different scenarios proposed for the initial stages of the MSC, we model with an initial large seabed depth of 1138 m. Here we assume paleo- and present-day seabed depths are the same.

Scenario (1) for shallow gas accumulation in small submarine channels uses overburden thicknesses ranging from 74 to 371 m and a small methane gas column of 3 m. Here we use porosities of 58% and 47%, permeabilities of 10^{-17} and 10^{-18} m^2, representing subsurface conditions for 74 and 371 m depths, respectively.

Scenario (2) for a deep Early Miocene stratigraphic trap accumulation uses overburden thickness of 986 m and a Tamar field equivalent gas column of 180 m, with three reservoir units (Needham et al. 2017). Overburden depth thickness is based on seismic time thickness from base Messinian salt to top Oligocene (800 ms) and a velocity of 2965 m/s. 200 m above top Oligocene depth is then determined, representing position of Tamar reservoir sands. Here we use porosity of 29 %, permeability of 10^{-19} m^2, representing subsurface conditions for 986 m depth.

In both scenarios, gas saturation and coefficient of pressure at rest were kept constant at 60% and 0.9, respectively, for depths described above (; estimated from Kim and Lee (2018) based on trends from Giles (1997), Neuzil (1994), and Needham et al. (2017)).

Three additional scenarios are presented for the Miocene that evaluate the sensitivity of sea-level fall to coefficient of pressure at rest, saturation of gas, and height of gas column beneath a seal, to understand their impact on tensile fracturing in our models. Sensitivity of sea-level fall to the coefficient of pressure at rest was modelled using values of 0.7 to 1.0, derived from well data in the Eastern and Western Mediterranean basins (Tamar field and Andalucia-1A well; Needham et al. 2017; Fernandez-Ibanez & Soto, 2017). The sensitivity of the model to saturation of gas was evaluated using saturations between 40 to 80%. For sensitivity analysis of gas column heights, values of 3 m and 38 m were selected. A gas column height up to 38 m was selected as the resolvable layer thickness in the seismic data, derived from the relationship between frequency, velocity, wavelength and resolution (Liner et al. 2019), and for a claystone with compressional velocities of 3000 m s^{-1} and dominant seismic frequency between 50 and 10 Hz.

In the analytical models, we used present-day seismic thicknesses and not the pre-compacted thicknesses of Miocene sediment. To evaluate the effect of compaction on Miocene sediment, especially when ~1 km of Messinian salt was deposited above, we run a 1-D disequilibrium compaction model (refer to Marin-Moreno et al., 2013 and Dale et al., 2021 for details). Our seismic stratigraphic model comprises three units with single representative lithologies: Oligocene to Miocene claystone, Messinian salt, and Pliocene claystone (supporting material Table S1). Although our models are based on brine as the pore fluid type, we changed the sediment compaction factor β to represent a more compressible sediment due to the presence of gas in the Oligocene to Miocene unit. For mixed claystone/ sandstone and claystone alone, average compaction factors used ranged from 0.6 to 1.0 for the Oligocene to Miocene unit, considering porosity ranges between 60 to 10% and density of fluid consisting of 70% gas (231 kg m^{-3}) and 30% brine (1030 kg m^{-3}). This is reasonable considering estimates of gas saturation in the A and B sands of the Tamar-1 well of 73 to 82% (Needham et al., 2017). Considering the above assumptions in the model, we estimate that the decompacted thicknesses for Oligocene to Miocene sediment are ~10 to 11 % higher than present-day seismic-derived thicknesses. For the Levant Basin analytical models with present-day seismic-derived overburden scenarios of 74 and 371 m, this equates to an increase of 7.5 to 8.1 m and 37 to 41 m, respectively. When comparison is made to the sediment overburden versus sea-level fall for the shallow overburden scenario of 371 m, using a decompacted 412 m overburden thickness (371 + 41 m), we estimate the sea-level fall required to initiate tensile fracturing is 441 m, 53 m above estimates using present-day seismic thicknesses (increase of 12 %). We therefore show that using present-day thicknesses as opposed to decompacted thicknesses in our analytical models has an effect, but it is not critical for assessing if sea-level fall triggered gas overpressured-induced fracturing of Miocene sediments because the difference is small.

3.6.3 Impact of the model properties on sea-level fall and fracture initiation

We evaluated the impact of coefficient of pressure at rest, saturation of gas and thickness of a gas column height on the sea-level fall required to initiate tensile fracturing for shallow scenarios (Figure 25).

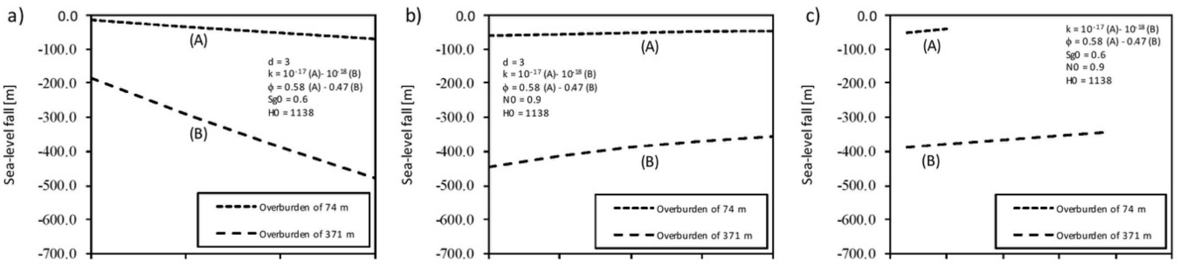

Figure 25: Influence of modelled parameters on sea-level fall required to initiate formation fracture with (a) coefficient of pressure at rest ranging from 0.7 to 1.0 (b) initial saturation of gas ranging from 0.4 to 0.8 and (c) thickness of gas column beneath a seal ranging from 3 to 38 m. A and B represent shallow scenarios with overburden thickness of 74 m and 371 m, respectively.

Sensitivity of the model to coefficient of pressure at rest

We evaluated coefficient of pressure at rest (N_0) of 0.7 to 1.0, derived from exploration well data, geomechanical modelling, and inferred from published data in the Mediterranean (Needham et al., 2017; Fernandez-Ibanez & Soto, 2017; Cartwright et al., 2021). For N_0 of 0.7 to 1.0 with a 3 m gas column height and overburden thickness of 74 m, sea-level fall required to initiate tensile fracturing varies from 14 m to 70 m, respectively. For N_0 of 0.7 to 1.0 with a 3 m gas column height and overburden thickness of 371 m, sea-level fall required to initiate tensile fracturing varies from 185 m to 479 m, respectively.

Sensitivity of the model to initial saturation of gas

Gas saturation varies greatly in the Tamar-1 well/field (0.1 to 0.95; Needham et al., 2017). To understand the impact of gas saturation on our models, we evaluate gas saturations from 0.4 to 0.8, considering the low values from the Tamar field core air-brine capillary pressure versus water saturation profile bulk dataset and high values from the calibrated porosity-weighted average gas saturation in the A and B sands of the Tamar-1 well, near the crest of the trap structure (Needham et al., 2017). For gas saturations of 0.4 and 0.8 with overburden thickness of 74 m, sea-level fall required to initiate tensile fracturing varies from 61 m to 48 m, respectively. For gas saturations of 0.4 and 0.8 with overburden thickness of 371 m, sea-level fall required to initiate tensile fracturing varies from 446 m and 356 m, respectively.

Sensitivity of the model to gas column height

We evaluated gas column heights of 3 m from Myra-1 well log data (Ben-Gai, 2021), and 38 m from the resolvable seismic layer thickness. We do not evaluate a gas column height of 38 m for overburden thickness of 74 m, as a gas column of this height at this shallow depth is considered unreasonable. Instead, we evaluate a smaller gas column height range of 3 and 10 m for this scenario. For a gas column height of 3 and 10 m with overburden thickness of 74 m, sea-level fall required to initiate tensile fracturing varies from 52 m to 41 m. For a gas column height of 3 m and 38 m with overburden thickness of 371 m, sea-level fall required to initiate tensile fracturing varies from 388 m to 344 m, respectively.

3.7 Results

3.7.1 Shallow gas in Middle to Late Miocene submarine channels modelling results

Figure 26 the results of the shallow gas accumulation scenario modelling in the Levant Basin. We consider a gas accumulation of 3 m with overburden thickness of 74 m (Figure 26a-c) and 371 m (Figure 26d-f), a sea-level fall rate of 0.015 m/yr, and an initial starting seabed depth of 1138 m.

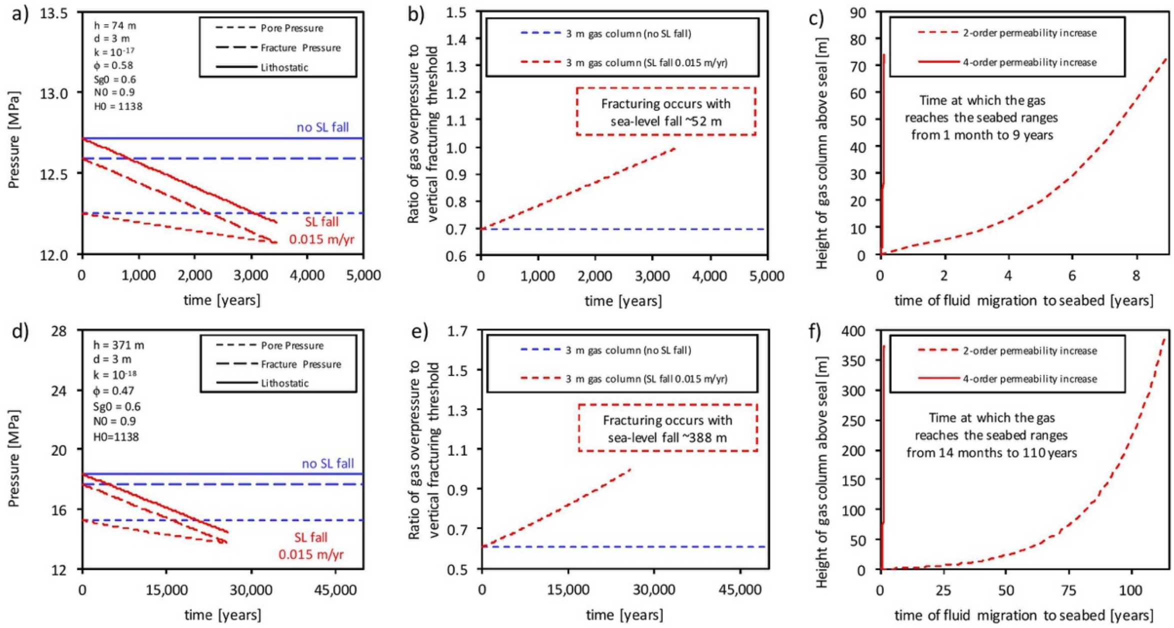

Figure 26: Scenarios of gas overpressure-induced chimneys from shallow gas accumulations. Results for the Middle to Late Miocene scenarios with overburden of 74 m (a, b, c) and of 371 m (d, e, f). Evolution with sea-level fall of paleo-pressure (a, d) and ratio of gas overpressure to tensile-vertical fracture threshold (b, e). (c, f) Timing of gas migration to seabed.

For the case with 74 m overburden thickness, the initial pore pressure, gas column overpressure and fracture pressure are 12.3, 0.03, and 12.6 MPa, respectively. Following sea-level fall of ~52 m over 3,462 years, pore and fracture pressures decrease to 12.1 MPa (Figure 26a) at which point tensile fracturing may have occurred (ratio of gas overpressure to vertical fracturing threshold of 1; Figure 26b). Assuming permeability increases of 4 orders (10^{-17} to 10^{-13} m^2) and 2 orders (10^{-17} to 10^{-15} m^2) of magnitude in response to fracturing, the time for fluid to reach the seabed (74 m distance) ranges from 1 month to 9 years, respectively.

For the case with 371 m overburden thickness, the initial pore pressure, gas column overpressure and fracture pressure are 15.2, 0.03, and 17.7 MPa, respectively. Following sea-level fall of ~388 m over 25,890 years, pore and fracture pressures decrease to 13.7 MPa (Figure 26e), at which point tensile fracturing may have occurred. Assuming permeability increases of 4 orders (10^{-18} to 10^{-14} m^2) and 2 orders (10^{-18} to 10^{-16} m^2) of magnitude in response to fracturing, the time for fluid to reach the seabed (371 m distance) ranges from 14 months to 110 years, respectively.

3.7.2 Deep stratigraphic trap in Early Miocene sands modelling results

Figure 27 shows the results of the deep stratigraphic trap modelling in the Levant Basin. We consider a gas accumulation of 180 m with overburden thickness of 986 m (Figure 27a-b), a sea-level fall rate of 0.015 m/yr, and an initial starting seabed depth of 1138 m. For the case with 986 m overburden thickness, the initial pore pressure, gas column overpressure and fracture pressure are 23.2, 1.52 and 30.5 MPa, respectively. Following sea-level fall of 1138 m, pore and fracture pressures decrease to 17.4 MPa and 19.0 MPa, respectively, with 1.66 MPa of gas column overpressure retained in Early Miocene sands.

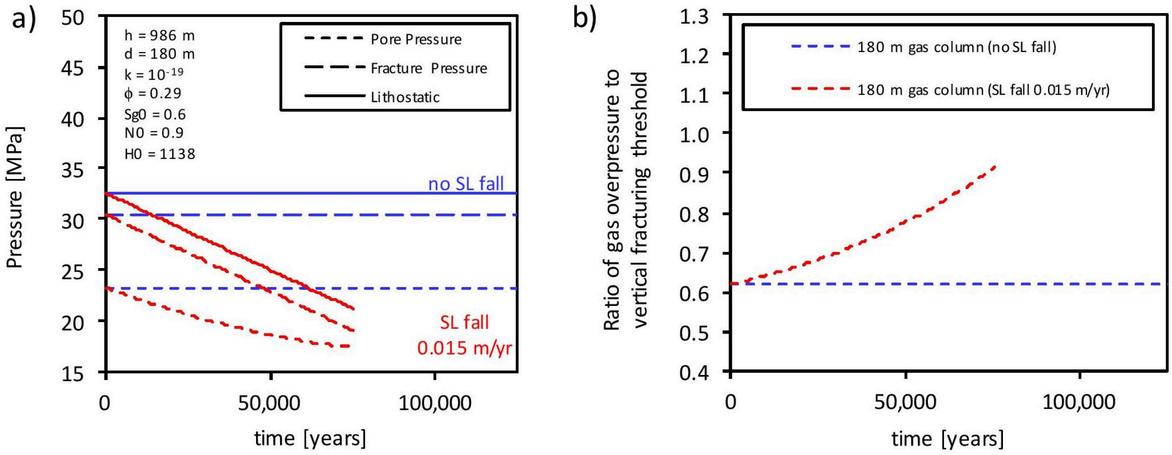

Figure 27: Scenario of gas overpressure-induced chimney from a deep stratigraphic trap. Results for the Early Miocene sands with overburden of 986 m (a, b). Evolution with sea-level fall of paleo-pressure (a) and ratio of gas overpressure to the tensile-vertical fracture threshold (b).

3.8 Interpretation and Discussion

Our modelling suggests that shallow gas escape from Middle to Late Miocene sands during the onset of the MSC triggered by sea-level fall of 10s to 100's m is more plausible than gas escape from an older source triggered by large sea-level fall of >1000 m. Further evidence supporting this result is provided by i) distinct continuous seismic reflectors in the Oligocene to Early Miocene units and absence of a gas chimney structure or faulting from the Oligocene to the base of the MSC deposits, ii) observations of seal failure of shallow Middle to Late Miocene units from several studies in the Mediterranean (e.g., Pérez-Asensio et al., 2012), and iii) sea-level fall being limited to 100s m from observations of enhanced erosion in the deep water canyons of the Levant margin. However, we recognise that gas escape from deep Early Miocene sands, triggered by much greater sea-level fall (>1000 m) cannot completely be discounted, considering that i) a basin container greater than 1 km thickness may have existed at the start of the MSC to accommodate significant sea-level fall, ii) the absence of fluid flow features on the seismic data does not rule out fluid migration, and iii) low temperatures and geothermal gradients and early trap formation support the presence of a deep biogenic system (Macgregor, 2018) from which fluid could have been released.

Other mechanisms of overpressure generation and crater formation could have acted here, in combination with sea-level fall, such as hydrate dissociation and disequilibrium compaction (specifically sediment loading from MSC salt accumulates). Sediment remobilization due to dissociation of methane hydrates is a mechanism that may have contributed to the formation of paleo-seabed craters in our study area (Bertoni et al. 2013; Hermanrud et al. 2013). We recognise that hydrate dissociation may have occurred, considering i) the visual similarity of the Levant Basin and Barents Sea craters, with hydrate dissociation considered responsible for the formation the Barents Sea giant seabed craters (Halkjelsvik, 2012 in Hermanrud et al., 2013), ii) that hydrate dissociation has been suggested to explain soft-sediment deformation in the Lorca Basin, southeastern Spain (Pierre et al., 2002), and iii) that this part of the Afiq canyon system would have been within the paleo water depth and temperature range of the hydrate stability field prior to sea-level fall (paleo depth ~1000 m, bottom temperatures ~5–10 °C; Bertoni et al. 2013).

To assess the importance of overpressure generation caused by disequilibrium compaction we used Marin-Moreno et al. (2013) model (see Table 10 for input parameters). We indirectly consider gas as the pore fluid by increasing our compaction factor within the pre-Messinian Miocene units (see above). To constrain petrophysical properties controlling the generation of pore fluid overpressure within the Messinian evaporites, we undertook laboratory measurements of permeability, porosity and density (chapter 4) to improve the predictions of overpressure. Our model shows the impact on overpressure is greatest during Stage 2 of the MSC when loading generated by deposition of ~500 m of halite caused overpressure and λ^* (ratio of overpressure to effective stress under hydrostatic conditions) to increase above a point at which tensile fracturing may have occurred, resulting in overpressure release from within the halite (Figure 28). Our disequilibrium compaction model cannot explain the development of the pockmark and crater features at the base of the MSC evaporites when tensile fracturing occurred during deposition of the Stage 2 MSC, and only after ~ 500 m of halite were deposited. We recognise that the load exerted by deposition of any Messinian evaporites during sea-level fall is null in our 1-D analytical models and therefore that sea-level fall and sediment loading should be considered jointly as contributing factors in overpressure generation. In such a scenario, estimates of sea-level fall with loading would be lower than what we estimated with the analytical models in our results above, i.e., including sediment loading tends to reduce the required magnitude of sea level fall.

1-D Model				
		Early to late Miocene (Pre-Messinian)	**MSC evaporite (Mavqi'im)**	**Pliocene to Quaternary (PQ)**
Seismic time thickness	ms	1044 (1)	457 (1)	974 (1)
Velocity	m/s	2965 (2)	4300 (3)	1834 (2)
Present-day seismic depth thickness	m	1548	983	893
Pre-compacted thicknesses	m	1743	1000	958
Modelled thickness present-day	m	1553	981	895
Time duration	Ma	17 (5)	0.05 (4)	5.3 (4)
Dominant Lithology	-	Claystone	Halite	Claystone
Compressible initial porosities at seabed	%	30 (6)	2.0 (1)	30 (6)
Average grain density	g cm^{-3}	2650 (7)	2160 (1)	2650 (7)
Permeability at seabed	m^2	10^{-17} (8)	10^{-20} (1)	10^{-17} (8)
Initial compaction factor	km^{-1}	1.0 (1)	0.1 (1)	0.5 (1)

Table 10: Physical property parameters used in 1-D disequilibrium compaction modelling to evaluate the evolution of overpressure from Miocene to present-day for the Levant basin. References: (1) this study; (2); estimated averages of 6 wells from Gardosh, et al., 2006; (3) El-Bassiony et al., 2018; (4) CIESM, 2008; (5) estimate from Tectonostratigraphic chart in Al-Balushi et al., 2016 (6) single estimate of 30 % set from Proshlyakov, 1960 as porosity ranges from 60 to 11 % exist for seabed to 500 m below seabed in Erickson et al. 1978; (7) Mavko, et al., 2009; (8) Neuzil, 1994.

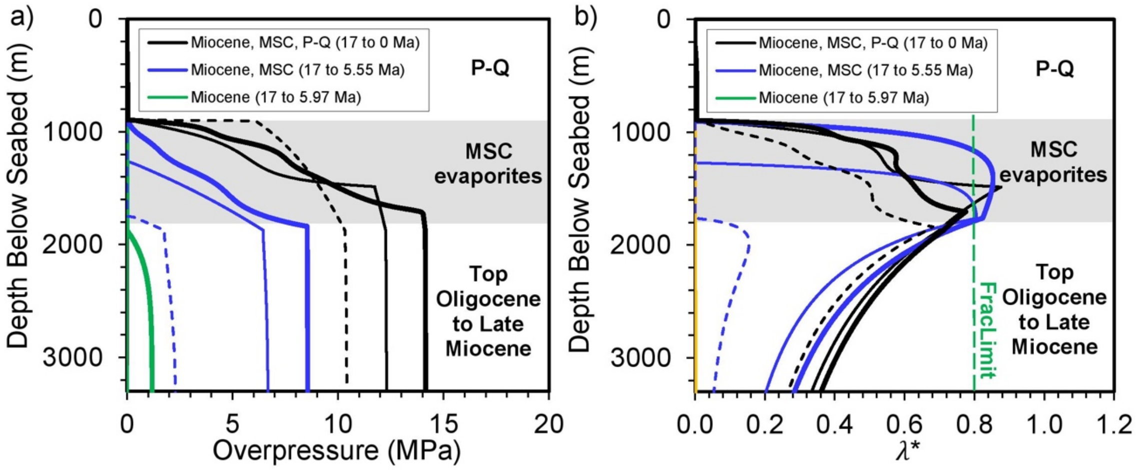

Figure 28: Most likely scenario of evolution of overpressure and λ* from Miocene to present-day for the Levant basin model. (a, b) Overpressure and λ* evolution with depth for the deposition of a given unit with three equally divided subunits, where dashed lines correspond to the first time increment, thin solid lines correspond to second time increment, and bold lines correspond to end of deposition for a given unit. Results are presented relative to present-day depth. All models use a constant fracture limit of 0.8.

Overpressure generated by tectonic compression or uplift and subsequent fluid release that contributed to development of the linear swarm of pockmarks/craters in the Levant Basin is considered unlikely (Figure 23; Bertoni et al. 2013). Previous research suggests that during the Early to Middle Miocene, the shelf in the eastern Mediterranean (Israel) was tectonically uplifted (e.g. Buchbinder et al., 1997). Although we cannot exclude short term events (e.g., earthquakes) generating gas release, we consider longer term tectonic compression, uplift and general tectonic activity unlikely over our study area, because (i) the development of pockmarks occurred specifically at the base MSC, when important hydrological changes were happening in the basin, (ii) there are no signs of continued pockmark formation in other parts of the stratigraphic column related to tectonic activity in the area, and (iii) pockmark locations are far from faults or folds active at the beginning of the MSC.

3.9 Conclusions

We used a 1D analytical model of chimney formation caused by gas overpressure to explain the crater pockmarks observed at the base of the Messinian evaporites in the Levant basin. The field of pockmarks was most likely triggered by fluid migration from shallow methane gas accumulations in middle to late Miocene sediment towards the seafloor, triggered by sea-level fall at the beginning of the Messinian Salinity Crisis (MSC) of a few 10s to a few 100s m. This limited sea-level fall of 100 m is compatible with enhanced erosion observed in the deep-water canyons of the Levant margin. A deep stratigraphic reservoir (Early Miocene sands) requires an unreasonable sea-level fall (>1000s m) to generate tensile fractures at the beginning of the MSC.

Chapter 4 Experimental study of the elastic and transport properties of salt rock and controlled dissolution: Insights for H_2 caverning

Salt rock is an effective sedimentary seal with low permeability, low porosity and high capillary entry pressure. To use salt caverns for storage of compressed hydrogen as part of renewable electricity systems, we need to better understand and quantify salt rock hydromechanical properties and to better understand factors that may lead to uncontrolled dissolution and fluid release from the host rock. In this experimental work, we undertook laboratory measurements to investigate the initial properties of salt rock and stress coupling effects prior to evaluating the impact of dissolution on the geophysical properties of intact (non-cracked) and cracked salt rock samples. The combined measurements of permeability and velocity with empirical trends provide important information for stress dependency and elastic-permeability relationships of salt rock at high pressure of confinement up to 50 MPa. Geophysical signature demonstrate that small discontinuities may significantly impact dissolution patterns, promoting fluid transport. This work could be developed further to guide seismic monitoring strategies during solution-mining and long-term safe storage of gases (e.g., hydrogen) in caverns.

4.1 Introduction

Salt rock is a suitable host rock for underground natural gas storage (e.g., hydrogen), for disposal and storage of nuclear waste (e.g., radioactive fuel), and naturally as an effective seal for trapped oil and gas, predominantly due to excellent self-healing, low permeability, long-term creep behaviour, and high entry pressures (Gloyna and Reynolds, 1961; Popp and Kern, 1998; Popp et al., 2001; Zhang et al., 2020). Salt mining for storage and extraction purposes requires a deep understanding of their in-situ transport properties for the design and safety of underground cavities (i.e., to better assess the hydromechanical response of salt mine storage site during caverning development activities (Fokker, 1995; Popp and Kern, 1998)). Dissolution can occur rapidly in natural (salt) karstic systems or by human activity (intentionally or inadvertently) producing impacts such as subsidence and collapse of overlying strata over a short-timescale, instability to above ground and underground construction and transport of waste out of the storage repository (Johnson, 2005; Weisbrod et al., 2012). Halite or 'rock salt' is a highly soluble material mainly composed of sodium chloride (NaCl). Four requirements have been suggested for dissolution to occur (Johnson, 1989, 2005): (i) deposits of salt through which water (brine) can flow, (ii) a source of NaCl-unsaturated brine flowing through the salt, (iii) an open outlet to allow the flow-through, and (iv) enough hydraulic energy to ensure brine flow through the system. Davies (1989) described dissolution of halite in contact with groundwater unsaturated in brine as 'essentially instantaneous', with the rate of solid salt removal controlled by diffusion and convection transport mechanisms. Transport by diffusion occurs when solutes move under the influence of their own kinetic activity in the direction of decreasing concentration. This process is slow with respect to free convection due to a contrast of pre- and post-dissolution fluid densities, which leads to more effective dissolution.

In nature, we can find natural and artificial (human-induced) salt dissolution structures. Natural dissolution is sensitive to climatic changes, as it is to groundwater. Salt karst formation in the United Kingdom was studied by Cooper (2002), who suggested that the karsting was related to changes in the groundwater regime during the last glaciation (Devensian). Essentially, when the ice sheet melted, groundwater level increased and enabled the circulation of freshwater through salt units interbedded with more permeable units of siltstone, mudstone and gypsum. Lugli et al. (1999) related the natural salt dissolution of the Messinian Realmonte salt deposit (Sicily) to basin desiccation. In this case, halite was heated upon exposure and broken, and then affected by drawdown of the groundwater (~4-6 m below surface) with meteoric-water dissolution cutting vertical dissolution pipes. Anderson and Kirkland (1980) found that collapse structures and breccias in the Delaware Basin of western Texas were associated with enhanced dissolution due to the free convection triggered by the density difference between the (pressurized or artesian) source of freshwater with respect to the generated brine within evaporites and collapse of overlying units.

Artificial salt dissolution is a common engineering approach during mining activities to enhance extraction, and to generate available volumes for underground storage (i.e., artificial caverns). Salt caverns will play an important role in the net-zero energy transition challenge, serving as safe locations for underground hydrogen (energy) storage (UHS), to efficiently contribute to the renewable energy supply during the seasonal demanding periods (Tarkowski and Czapowski, 2018). The process of solution mining and cavern/reservoir formation involves (i) injecting water using injection tubing to dissolve the underground salt and form brine, and (ii) extracting the brine solution to surface with a production tubing set sufficiently below the injection point to extract the higher density brine which tends to flow downwards (Fokker, 1995). Generating salt caverns for underground storage might also lead to environmentally undesirable effects derived from fracturing related to the seasonal energy demand (increasing/decreasing pore pressure cycles, biannually), or land subsidence due to subsurface dissolution (Fokker, 1995; Zidane et al., 2014). For instance, Stoeckl et al. (2020) found that chamber collapse of abandoned salt mines in the Ukraine might increase the salinity of the Tisza river, which supplies drinking water to Ukraine, Romania, Hungary and Croatia. Also, salt dissolution and collapse of the Wink Sink in Texas in 1980 was found to be influenced by petroleum activities (Johnson, 1989).

Geophysical tools can be used for monitoring the evolution of the caverning during artificial generation and mining/storing activities. Seismic properties inform about the status of the rock frame and evolution of dissolution through potential decreasing in both P- and S-wave velocities (V_P and V_S) and their respective attenuation factors. Electrical resistivity offers a good diagnostic of the rock changes during the caverning process due to the high conductivity contrast between the pore fluid and the rock matrix, although the poor resolution of the method in depth complicates resolving the channelling geometries accurately. The expansion of UHS activities will potentially require development of specific numerical predictive tools, calibrated with experimental data. These numerical tools require constraints from laboratory tests under controlled conditions of natural salt dissolution combined with geophysical monitoring. These laboratory tests are currently very limited mainly due to the complexity of the experimental configurations required (e.g., corrosiveness related to sample coring preparation and hypersaline fluid flow testing).

Experimental studies with salt rock have historically focused on the mechanical properties and permeability characteristics of both altered (fractured) and undamaged salt rocks (Beauheim et al., 1991; Brodsky, 1994; Cosenza and Ghoreychi, 1997; Gloyna and Reynolds, 1961; Kröhn et al., 2015; Pfeifle and Hurtado, 1998; Rutqvist, 2015; Stormont, 1997; Stormont et al., 1992; Wang et al., 2018; Zhang et al., 2020). However, only few works have addressed how the permeability of salt related to its elastic properties under variable effective stress conditions (Ezersky and Goretsky, 2014; Popp and Kern, 1998; Popp et al., 2001). This combined analysis can enable to indirectly estimate hydromechanical changes (i.e., pore space and connectivity with effective pressure), which is crucial for UHS due to the cyclic (annual) variability of the underground pressure conditions associated with this technology. Furthermore, experimental work addressing the potential use of these tools for monitoring dissolution during caverning activities is missing, to the best of our knowledge.

Beauheim and Roberts (2002) reported salt permeabilities within the range of 10^{-21} to 10^{-24} m^2, in undamaged rock formations. Popp and Kern (1998) reported a dataset combining absolute (gas) permeability with V_P, V_S under increasing confining pressure for rock samples from the Gorleben salt dome (with composition ranging between 90-98 % halite and 3-10 % anhydrite). Their results showed that, at low confining pressure (5 MPa), the tested samples showed high variability in permeability (~10^{-16} to 10^{-20} m^2), but low P and S-wave velocities variability (4.45 ± 0.1 km s^{-1} s and 2.53 ± 0.06 km s^{-1}, respectively), while both permeability and wave velocities showed significant pressure dependency within the range 5-30 MPa (Popp and Kern, 1998). Ezersky et al., (2014) studied the relationship of porosity-permeability with the geophysical properties of shallow borehole salt rock samples from the Dead Sea, where, since 1990, thousands of sinkholes have occurred along coastal areas of Israel and Jordan. In this case, impurities such as carbonate-filled fractures (between 5-21%) resulted in a higher V_P and V_S variabilities (4.1 ± 0.4 km s^{-1} and 2.2 ± 0.3 km s^{-1}, respectively) and with V_P-V_S decreasing approximately linearly with porosity, for an equivalent permeability range of that reported by Popp and Kern (1998).

The aim of this study is twofold. First, we analyse the hydromechanical properties of seven salt rock samples from different geological environments to develop relationships between their elastic and transport properties, accounting for their dependency to effective pressure to help assessing suitable scenarios for UHS. Second, we select two samples to conduct controlled dissolution tests, to investigate the effect of rock structural heterogeneities on the dissolution and the use of common geophysical sensing methods (seismic and electromagnetic tools) for monitoring the process. The tests were conducted using one intact and one visually cracked halite samples, under constant confining (reservoir-like) and increasing pore pressure, with a continuous monitoring of the rock elastic and transport properties through their ultrasonic P- and S-wave attributes (i.e., velocities and corresponding attenuations), and electrical resistivity.

4.2 Materials and methods

4.2.1 Rock samples

For this study, we selected samples from various evaporite deposits, including Pre-Cambrian salt (Pakistan – four samples collected from a commercial rock namely Likit salt lick bricks (source: www.likit.co.uk/)), Cambrian salt (unknown well, Tunguska Basin, Russia), Triassic salt (Arm Hill #1 well, NW Lancashire, UK), and Messinian salt (3A GN3 S02 well, core # 19, near Marianopoli, Sicily, Italy). From the original rock specimens, we cored ~5 cm diameter core plugs, cut and their ends ground flat and parallel, resulting in ~2.5 cm length samples. Rocks composition were estimated by X-ray diffraction (XRD) analysis (conducted with a Philips X'Pert Pro XRD – Cu X-ray tube XRD), and connected porosity (ϕ) by He-pycnometry, while absolute porosity (ϕ_T) was estimated by the grain (ρ_s, from Dale et al. (2021b) and Mavko et al. (2009)) and bulk (ρ_b) densities, according to the relationship $\phi_T = 1- \rho_b / \rho_s$. Table 11 shows the main properties of the samples used in this study.

Sample	XRD-Mineralogy (wt.%)				Bulk density	Porosity (%)	
	Halite	Anhydrite	Polyhalite	Dolomite	(g cm^3)	Connected	Absolute
Miocene	95.8	0	2.2	2	2.160	0.10	1.32
Triassic	97.6	0.2	0	2.2	2.130	0.72	1.71
Cambrian	98.1	0	0.5	1.4	2.110	0.56	0.60
Pre-Cam1	97.3	0	0	2.7	2.159	1.14	2.26
Pre-Cam2	97.3	0	0	2.7	2.140	1.90	3.17
Pre-Cam3 (S1)	97.3	0	0	2.7	2.124	1.61	2.54
Pre-Cam4 (S2)	97.2	0	1	1.8	2.122	1.13	2.61

Table 11: Physical properties and mineralogy of the rock samples. Samples used for the dissolution test, and referred there as samples S1 and S2, respectively.

4.2.2 Experimental setup

The test was conducted using the high-pressure room-temperature (20°C) experimental setup for flow-through tests at the National Oceanography Centre, Southampton (NOCS) (Figure 29). The system allows for simultaneous measurement of the hydromechanical and geophysical properties of rock samples (e.g., Falcon-Suarez et al., 2017). Samples are radially ($\sigma_2 = \sigma_3$) and axially (σ_1) confined, independently controlled by a dual ISCO EX-100D system, although for this experiment we adopted a hydrostatic configuration (i.e., $P_c = \sigma_1 = \sigma_3$). Radially, the sleeve that prevents the contact between the mineral (confining) oil and the sample is equipped with two arrays of eight electrodes each for accurate electrical resistivity (including tomography) measurements. Under our operating conditions and in homogeneous samples, the bulk electrical resistivity error is <1% for bulk resistivities <100 Ω m increasing up to 5% above this value, at frequencies 1–500 Hz (North et al., 2013; North and Best, 2014). Axially, two platens house the ultrasonic pulse-echo sensors to measure P- and S-wave properties of velocity and their respective attenuations using the pulse echo method. This technique provides useable frequencies between 300 and 1000 kHz, with velocity precision of ± 0.1% and the accuracy of ± 0.3% (95% confidence), and attenuation accuracy of ± 0.1 dB cm^{-1} within this range (Best, 1992). For this test, we processed the ultrasonic data to compare the elastic properties of our three samples at a single (ultrasonic) frequency of 600 kHz, obtained from Fourier analysis of broadband signals. We refer, for instance, to Falcon-Suarez et al. (2017) for further information about the instrumentation sensors specification, and to Falcon-Suarez et al. (2020a) for multi-flow configurations.

For this experiment, we used two pore fluid configurations. First, we set up the rig to enable the circulation of N2-gas (directly delivered from a commercial bottle and with flow/pressure controlled by a manual regulator) through the (dry) core samples; second, during the dissolution tests, we used fluid transfer vessels (FTV1 and 2) to deliver and control (by another dual ISCO EX-100D system) the pore pressure (P_p) using 3.5% NaCl synthetic brine solution as pore fluid.

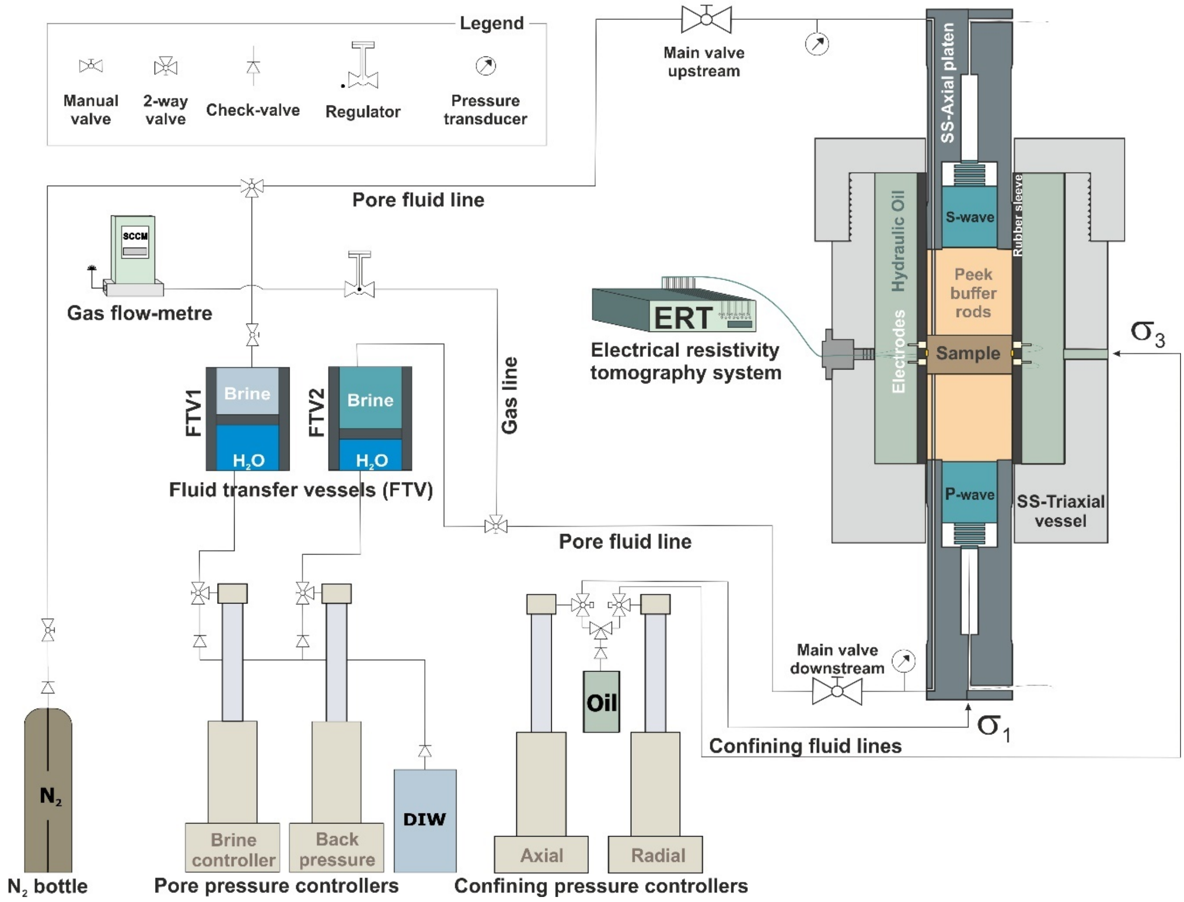

Figure 29: Experimental rig

4.2.3 SaLt rock elastic and transport properties and pressure dependency

The experiment was configured to investigate changes in the ultrasonic and transport properties of the samples under increasing pressure and returning to the original Pc to account for the increasing hysteresis, according to the P_c path 5-10-5-15-5-20-5-30-5-50 MPa (with the exception of the samples Pre-cam3 and 4 used for the dissolution test; see below) under dry conditions (i.e., Pp ~ 0.1 MPa). In every step, we applied a gentle loading/unloading stress rate of 0.05 MPa s^{-1} up to the target Pc, and then waited until the sample reached a mechanical equilibrium (i.e., when pressure controllers stabilized), before measuring the elastic and transport properties.

Elastic properties were measured using the technique and sensors described above. Permeability to N_2 was determined using the steady state (based on Darcy's law) and pore pressure transmission (based on transient states of the porous medium) methods (e.g., Falcon-Suarez et al., 2017; Metwally and Sondergeld, 2011), as convenient, depending on the sample permeability (high-medium permeability, the former; low, the latter). Klingenberg correction

(Klinkenberg, 1941) was applied in all cases to account for the gas slippage effect on the experimental data, to obtain the absolute permeability (k).

4.2.4 Dissolution test procedure

The two samples were selected for the dissolution test based on their hand-scale visual features (Dale et al., 2021a): Pre-Cam 4, with visible cm-scale cracking, and Pre-Cam 3, apparently coherent. To minimize potential pressure-induced changes on the original sample properties, we limited the elastic and transport characterization of these two samples to $P_c = 15$ MPa, which was the pressure selected for the dissolution tests (a representative value for existing salt caverns for H_2 storage around the world (e.g., Kruck et al., 2013)). Once we reached the target Pc, the brine was delivered at a minimum P_p of 0.1 MPa. Then, keeping P_c constant, P_p was progressively increased (1 MPa stepwise) attempting at reaching a minimum effective pressure ($P_e = P_c – P_p$) of 0.1 MPa. This procedure simulates a potential scenario of a progressive overpressure.

4.3 Salt rock elastic and transport properties

4.3.1 Experimental results

Figure 30 shows our results during the loading steps (hysteresis is assessed separately; see Figure 31), together with Popp et al. (2001) data, as this is the most suitable dataset available in the literature to assess our results, both in terms of measured parameters and pressure conditions. Note that Pre-Cam 3 and 4 were the samples used for the dissolution tests (see below), and therefore compressed (only) up to the target effective pressure used for those tests (i.e., $P_{eff} =$ 15 MPa).

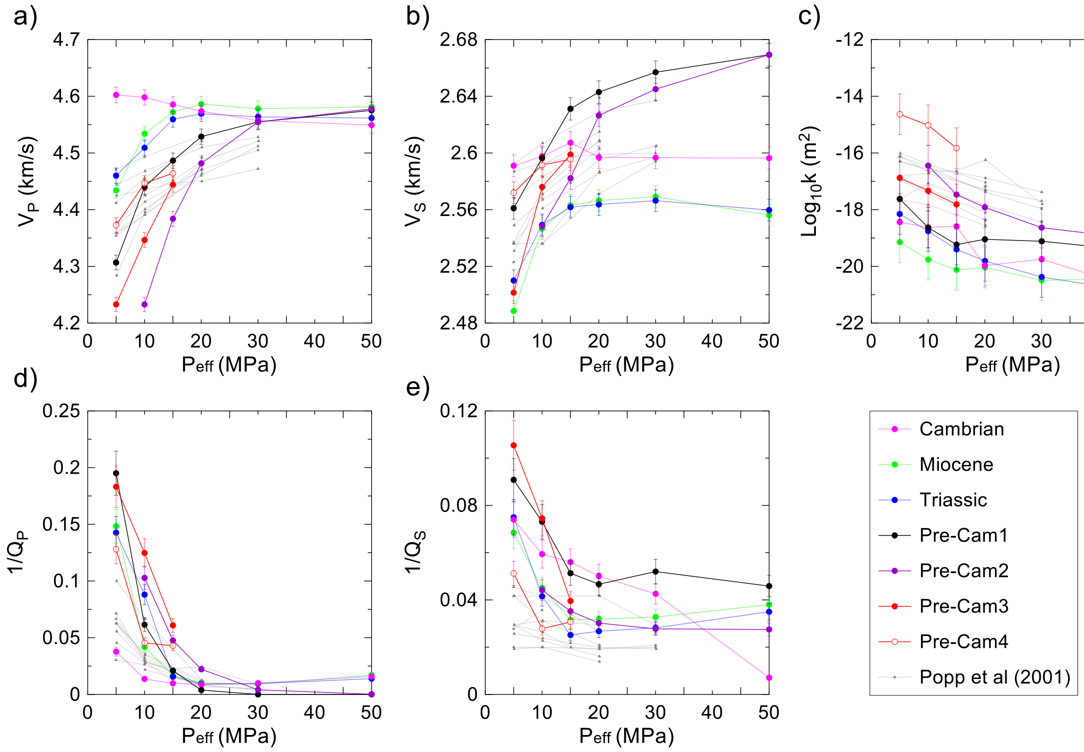

Figure 30: Ultrasonic wave velocities (V_P and V_S), attenuation factors (Q_P^{-1} and Q_s^{-1}) and permeability versus effective pressure for the salt samples used in this study (see *Table 11*) and the data reported by Popp et al. (2001).

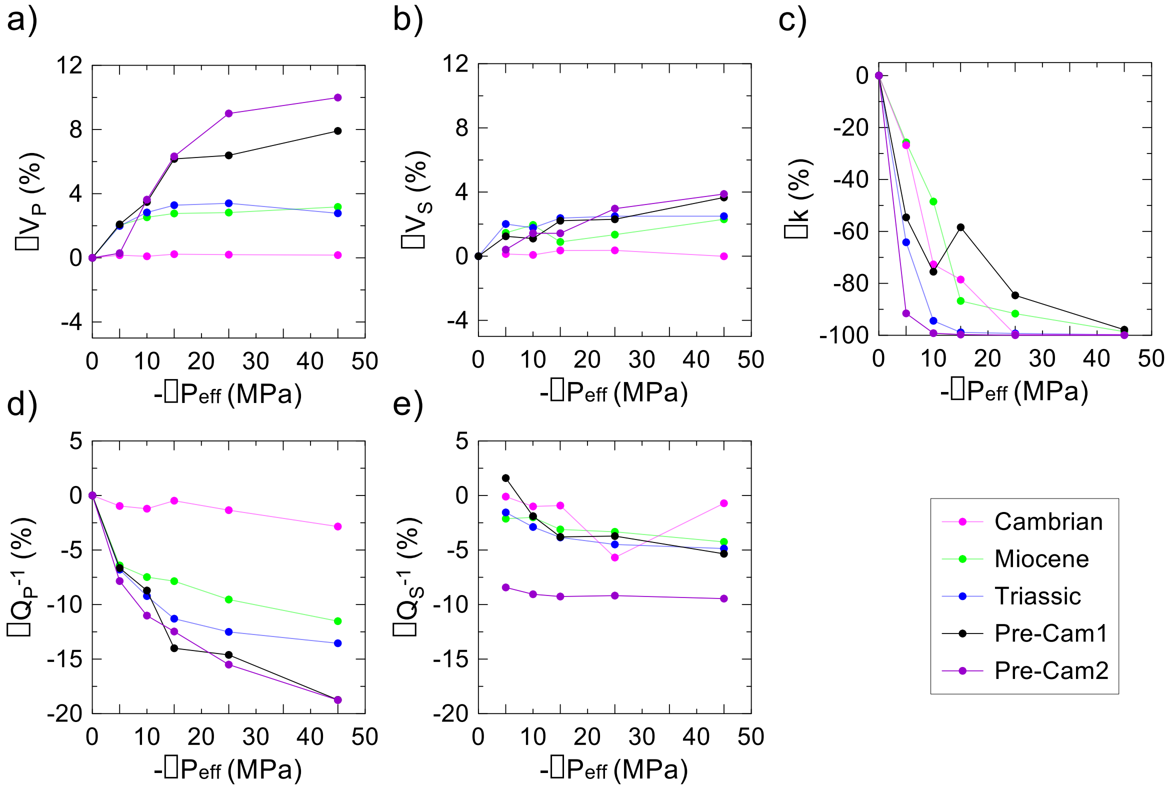

Figure 31: Hysteresis effect on the ultrasonic wave velocities (V_P and V_S), attenuation factors (Q_P^{-1} and Q_s^{-1}) and permeability with respect to the increasing unloading, for the salt samples used in this study (see *Table 11*).

Overall, our elastic parameters and permeability agree with Popp et al. (2001)'s data (Figure 30). V_P varies between 4.2 and 4.6 km s-1 (i.e., < 10%) for the tested pressure range, increasing with effective pressure in all samples except for the Cambrian one, but all approaching to a common maximum of 4.575 ± 0.025 km s^{-1}. V_S exhibits smaller range, between 2.49 and 2.67 km s^{-1} (i.e., < 7%), with a less defined maximum. The same occur with their respective attenuation factors: both Q_P^{-1} and Q_s^{-1} decrease towards zero with the increasing pressure, explained as a drop of energy dispersion related to microcracks closure.

Permeability spans nearly six orders of magnitude, also decreases with increasing pressure in all samples. The permeability of our samples are all below Popp et al. (2001)'s except for sample Pre-Cam4 (Figure 30), which was specially selected for exhibiting a cm-scale crack. According to the elastic parameters and permeability results, the main changes in the salt rocks occur below 20 MPa. However, the lack of data in Popp et al. (2001) above 30 MPa hampers further analysis in this regard. Our results below 20 MPa also agree with the data reported by Zhang et al. (2020) for permeability of salt rock under hydrostatic loading.

Figure 31 shows that all the parameters reflect certain degree of hysteresis after compaction. In general, P- and S-wave velocities increase and the attenuations and permeability decrease with respect to their original (pre-load) values with the unloaded pressure range (i.e., $-\Delta P_{eff}$) considered. Pre-Cam 1 and 2 are the most affected samples, with up to 10% increase in V_P and 20% decrease in Q_P^{-1} after 50 MPa compaction, and 4% and 10% for V_S and Q_s^{-1}, respectively. This behaviour might be related to the shallower origin of the commercial Pre-Cam samples, subjected for the first time to compaction. A similar degree of unrecovered permeability in all samples, particularly below 20 MPa (dropping between 60% and 100%), suggests similar permanent structural changes affecting the fluid pathways. Our results agree with the degree of hysteresis exhibiting by the few samples subjected to unloading in Popp et al. (2001), both in terms of elastic properties and permeability, and with the degree of unrecovered permeability in Zhang et al. (2020).

4.3.2 Combined assessment of elastic and transport properties

Data interpretation from underground storage activities is limited to the sort of data acquired and the correlations that can be developed from them. During our tests, we have measured combined ultrasonic properties, permeability and porosity; the latter transport properties are more challenging to collect in the field (i.e., commonly based on well logging information, and therefore limited to the surroundings of the well). Cross-plotting permeability and elastic properties of salt rocks may therefore help to expand our interpretation of the transport properties of a target formation.

By cross-plotting our elastic and permeability results, we identify linear trends between them all for each individual sample, which agree with the general fitting for Popp et al. (2001)'s data. The linearity is missing at high pressure (> 20 MPa) for permeability and the attenuation factors, this may indicate the existence of some cracks (i.e., compliant porosity (Shapiro, 2003; Shapiro et al., 2015)), but considering the low porosity of the samples, it could also be related to more complex grain-to-grain phenomena (e.g., recrystallization). Hence, in order to stablish a more thorough assessment accounting for the pressure dependency of each variable, we analyse the potential of the following empirical relationship to explain our data:

$$Y(P_{eff}) = A_Y + B_Y P_{eff} - C_Y \exp^{(-D_Y P_{eff})}, \qquad (1)$$

with Y acting as any (usually elastic) rock property, and A, B, C and D being fitting parameters. These four fitting parameters describe: A, the crack-free value for the property Y; B, the slope at high pressure; C, the sensitivity of the cracks compliance to pressure (Eberhart- Phillips et al., 1989), with A-C, expressing the zero-pressure velocity (Freund, 1992); and D, the rate of crack compliance with the increasing stress, a universal quantity based on sample elasticity, homogeneity and isotopic stress field, which has proved to be valid for sedimentary and crystalline (metamorphic) rocks of high and low porosity, and that also extends to transport (Kaselow and Shapiro, 2004).

This relationship has been successfully used to describe elastic properties of granular sedimentary rocks, including sandstones (e.g., Eberhart- Phillips et al., 1989; Zimmerman et al., 1986), siltstones and claystone (Freund, 1992), and transport properties in sandstones (from permeability (Shapiro et al., 2015) and electrical resistivity (Falcon-Suarez et al., 2020b; Kaselow and Shapiro, 2004)) with increasing P_{eff}. This relationship works well for sedimentary rocks under drained conditions as acoustic velocity increases with increasing effective pressure increase as pores and micro-cracks close leads to reduced rock compressibility (Eberhart-Phillips et al., 1989). However, it has been also successfully used for low porosity/permeability rocks (e.g., Kaselow and Shapiro, 2004), which are expected to poorly drain due to low pore connectivity. Here, we use equation (1) to obtain the four fitting parameters for our data and Popp et al. (2001)'s, for V_P , V_S and permeability. For the particular case of permeability, we used $Y = -\mathrm{Log}_{10}k$ in equation (1) to accommodate the fitting.

Figure 32 shows that the four fitting parameters depend on the initial porosity for P- and S-wave velocities and permeability. Our salt samples and Popp et al. (2001)'s fittings follow a similar trend in most of the parameters. From the parameter A, we see that the elastic properties are little influenced by the porosity within the considered porosity range (0-7%), while a clearer decreasing trend between porosity and permeability exists. At high pressure (above 20 MPa, in our case), the increasing pressure seems to only affect permeability, as for the elastic properties the parameter B is close to zero. In the lower pressure domain, parameter C seems to correlate differently with porosity for our data and Popp et al. (2001)'s, both for the elastic properties and permeability (see dashed lines in Figure 32). This fact might be related to the way different minerals accommodate the discontinuities, since the main difference between the two datasets is the amount and composition of the minerals accompanying the halite (i.e., < 3% dolomite in our samples; < 9% anhydrite in Popp et al. (2001)'s). The parameter D shows similar values for the ultrasonic waves and permeability, suggesting both properties accommodate the compaction mechanisms similarly, but the higher C for permeability indicates they have higher importance (Falcon-Suarez et al., 2020b) in the changes of transport properties.

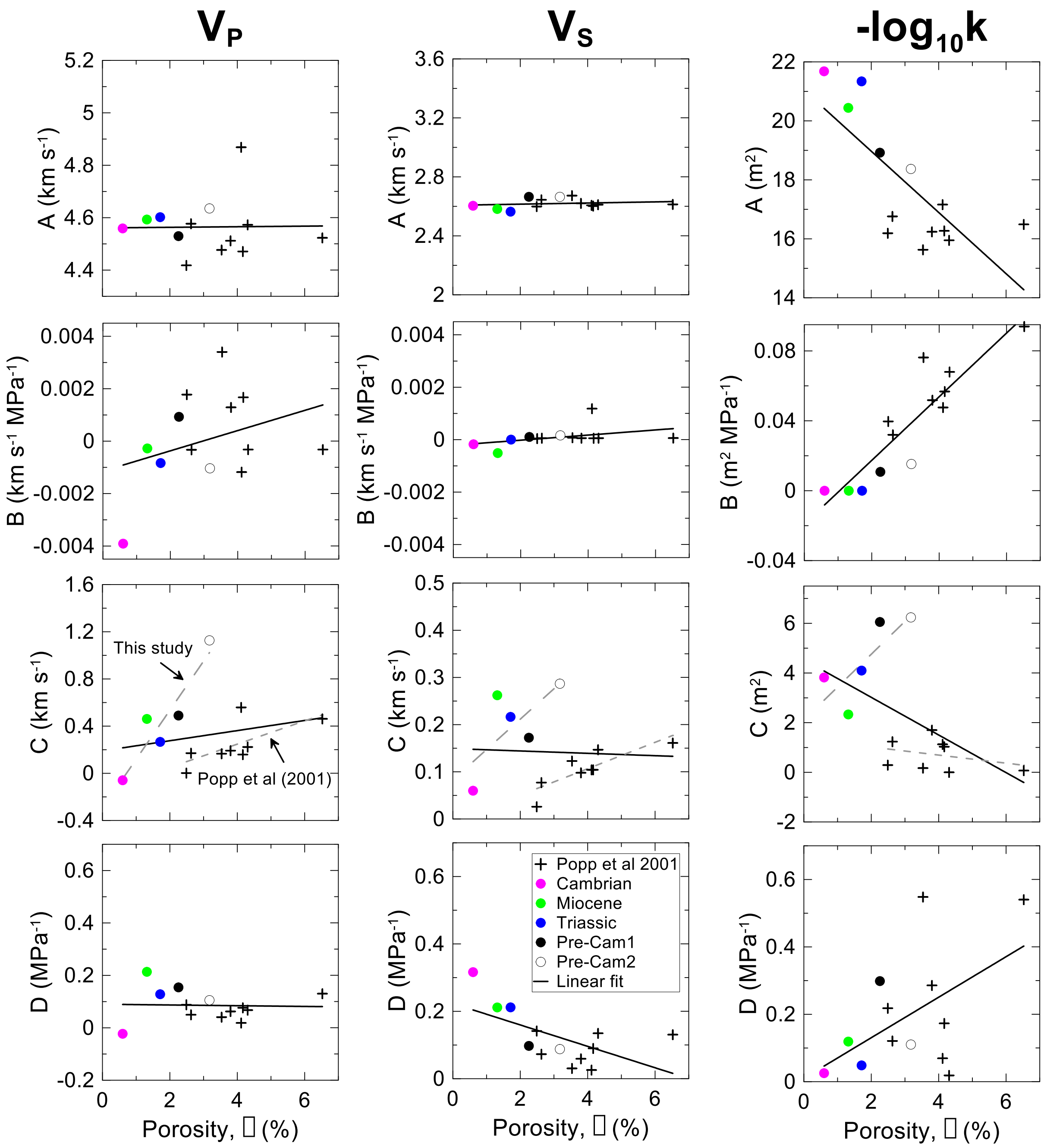

Figure 32: Fitting parameters A, B, C and D of equation (1) versus porosity for the ultrasonic wave velocities (V_P and V_S) and permeability for the salt samples used in this study (see *Table 11*), the data reported by Popp et al. (2001).

In terms of relationships between elastic and transport properties, Figure 33 shows that the fitting parameters for permeability correlate poorly with those of the V_P, although any correlation is statistically limited due to the reduced number of measurements per sample and the number of halite samples available for this study and the lower limit of our experimental permeability-setup (i.e., 10^{-21} m^2). Therefore, more samples and more precise sensors are needed to accurately expand our interpretation to the realm of ultralow permeability ($< 10^{-21}$ m^2).

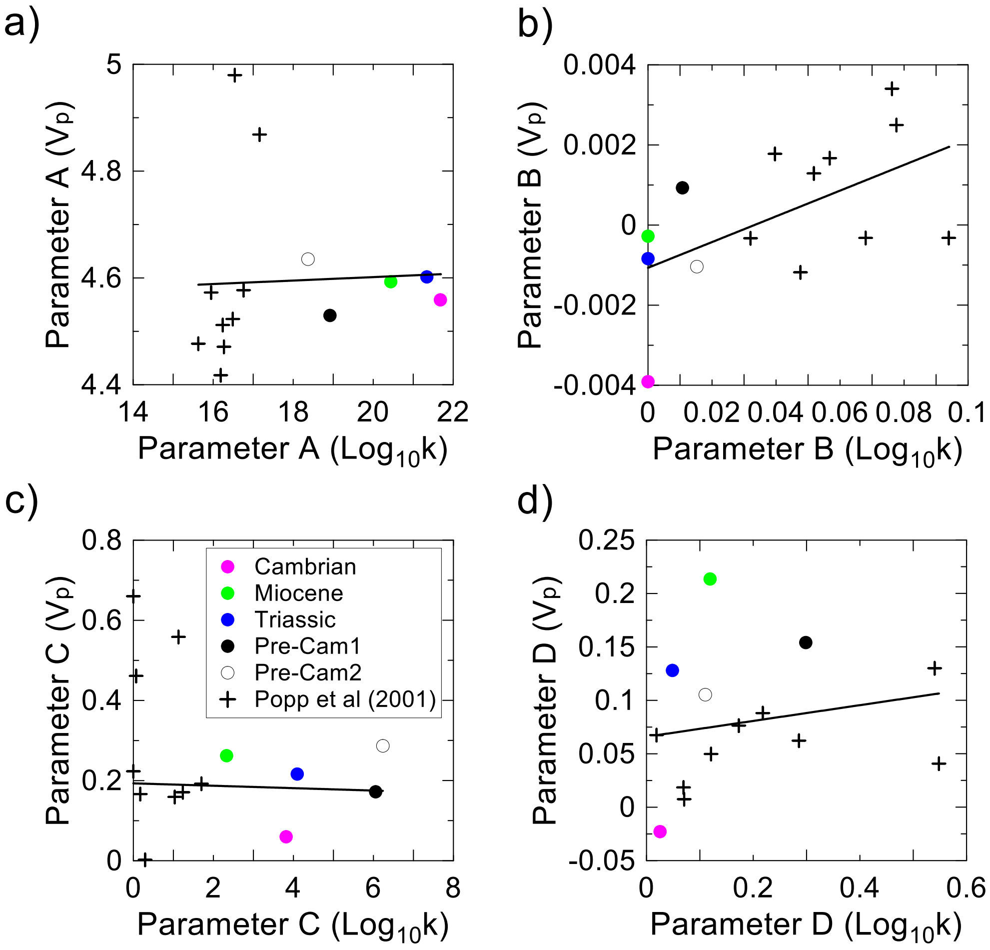

Figure 33: Fitting parameters A, B, C and D of equation (1) of the ultrasonic P-wave velocity (V_P) versus permeability, for the salt samples used in this study (see *Table 11*) and the data reported by Popp et al. (2001).

4.4 Controlled dissolution tests

The selected samples for the dissolution tests (i.e., Pre-Cam 3 and 4) show similar elastic and transport values and trends than the rest of the tested samples (Figure 30). The main difference is the higher permeability of Pre-Cam 4, due to the hand-scale crack observed in the sample. As this discontinuity is parallel to the direction of the wave propagation (i.e., perpendicular to the basal plane), the elastic properties, including the attenuation factors, remain unaffected (e.g., Falcon-Suarez et al., 2020b).

The dissolution test on sample Pre-Cam 4 lasted ~4 hrs (Figure 34). The test was terminated as a result of an early rock dissolution event that commenced in the nearby of the inlet pore fluid port and quickly propagated peripherical around the outer part of the sample, triggering the failure of the inner rubber sleeve in the triaxial vessel. The little time window of this test shows inconclusive trends of the elastic properties with a slight increase in V_P and Q_P^{-1}, possibly due to increasing saturation of the central part of the sample via (fast) imbibition, while the minor increase in V_S might be related to crack closure in localized areas. Resistivity was unable to be collected because of some electrodes-rock missing contacts associated with the early lateral dissolution. This early dissolution is fairly consistent with Davies (1989) who suggested that dissolution of halite in contact with unsaturated water is ‘essentially instantaneous’, irrespective of the rate. Our experimental results also agree with Weisbrod et al. (2012) hypothesis of fast dissolution channels formation along preferential fluid pathways in areas of minimum resistance to flow, such as cracks, even under high effective pressure (i.e., 15 MPa).

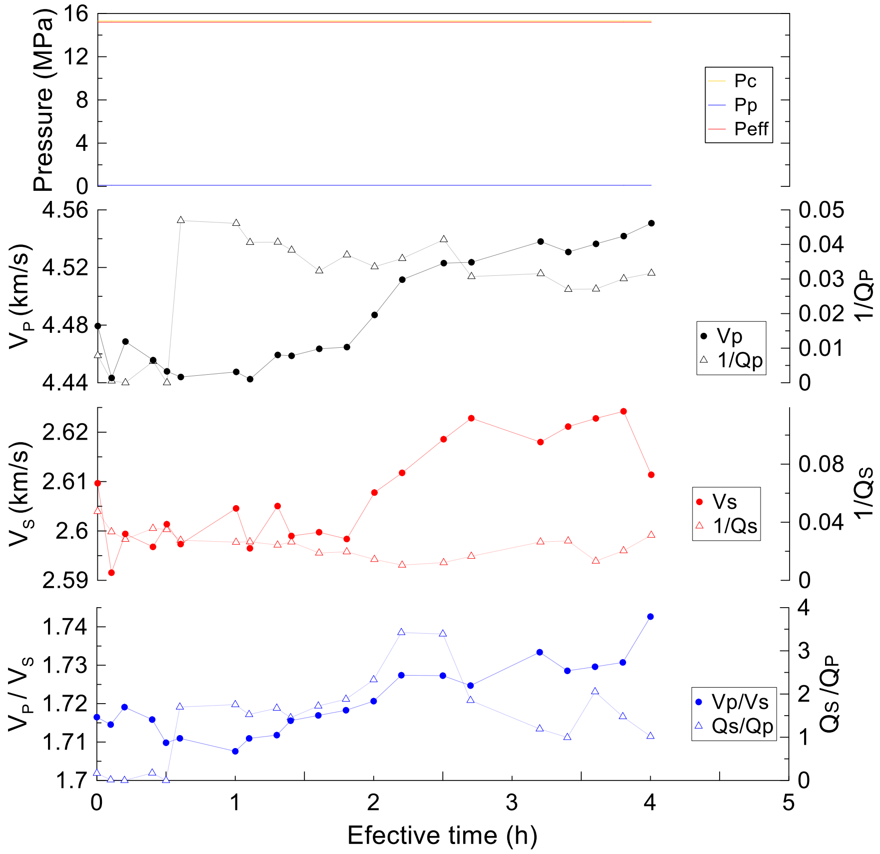

Figure 34: Dissolution test on the salt sample Pre-Cam 4. Ultrasonic wave velocities (V_P and V_S), attenuation factors (Q_P^{-1} and Q_s^{-1}) and V_P/V_S ratio versus effective time (i.e., disregarding interludes with no measurements).

The dissolution test on the intact salt rock sample Pre-Cam 3 (Figure 35) shows that the geophysical parameters vary very little during the first P_{eff} step, when the sample was exposed to brine under minimum pore pressure (P_p = 0.1 MPa, i.e., maximum P_{eff} = 15 MPa) for over three days (see the difference between interlude periods and effective time in Figure 35). During this period, we assume the sample is being partially saturated in brine, as Q_P^{-1} exhibits a little prompt increase in agreement with theoretical Q_P^{-1} -saturation curves with very small gas patchy areas at high (>60%) water saturation (Amalokwu et al., 2014), and resistivity starts decreasing after the first increment in pore pressure. Then, V_P progressively increases with the increasing P_p (despite the decrease in P_{eff}) due to changes in the bulk density of the sample as a result of the brine filling pores. Here the decrease in bulk modulus due to dissolution is smaller to the decrease in density due to the increase in volumetric concentration of brine. The brine saturation is heterogeneously distributed in the sample, more localized in the surroundings of the pore fluid inlet port, as interpreted from the decrease of resistivity in that area (ERT-3, Figure 36). When P_{eff} is below 6 MPa, V_P starts decreasing and V_S slightly increases, suggesting the decrease in density due to having brine instead of halite dominates over the decrease in shear modulus due to dissolution (this trend is more significant with the decreasing P_{eff}). At this point, resistivity drops by ~50% but still showing a highly heterogeneous distribution in the sample (ERT-4, Figure 36). This evolution has a complex interpretation, which lies in the interplay of both fracturing and dissolution. Once P_{eff} reaches its minimum (i.e., $P_{eff} = 0.1$ MPa), the test continues during two more days without significant changes in any of the geophysical properties (i.e., V_P ~4.53 km/s, V_S ~2.625 km/s and resistivity ~30 Ω m). From ERT-5 to ERT-6 (Figure 36), the inlet area exhibits a large decrease in resistivity, suggesting that dissolution was occurring preferentially during the period of minimum P_{eff}.. From our resistivity tomography data, we interpret the initiation of the channelling in sample Pre-Cam 3 at P_{eff}.≤ 3 MPa (Figure 36).

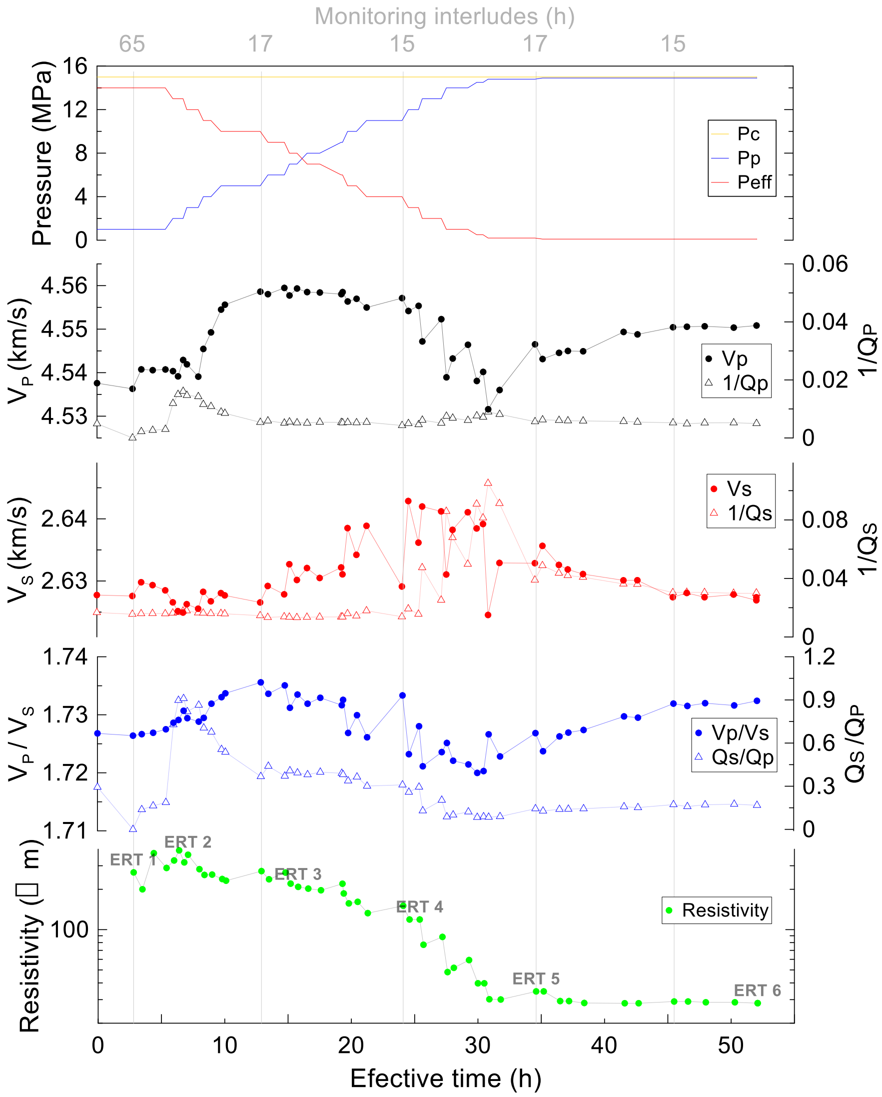

Figure 35: Dissolution test on the salt sample Pre-Cam 3. Ultrasonic wave velocities (V_P and V_S), attenuation factors (Q_P^{-1} and Q_s^{-1}), V_P/V_S ratio and electrical resistivity versus effective time (i.e., disregarding interludes with no measurements), for a decreasing effective pressure (P_{eff}) sequence. Electrical resistivity tomography was computed six times (ERT 1 to 6) during the test.

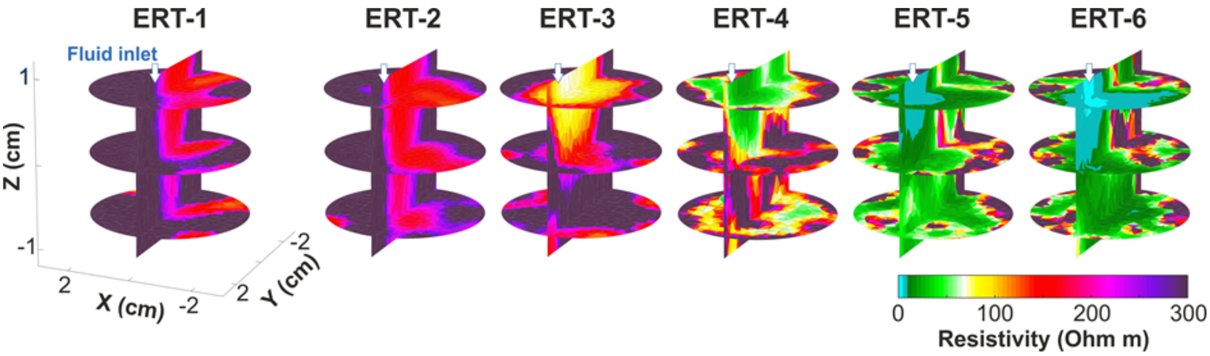

Figure 36: Electrical resistivity tomography (ERT) computed during the dissolution test on the halite sample Pre-Cam 3

To properly interpret the dissolution test, we need to understand the actual reach of our geophysical measurements. Figure 37a shows the configuration of our geophysical sensors in the vessel. The incidence of the P- and S-waves limit the interpretation of our experimental data to the 38 mm diameter of the central area of our samples. By contrary, the lateral position of the electrodes provides a bulk electrical resistivity record of the whole sample. Therefore, unlike resistivity, our ultrasonic sensors are blind to the changes occurring in the outer areas of the samples.

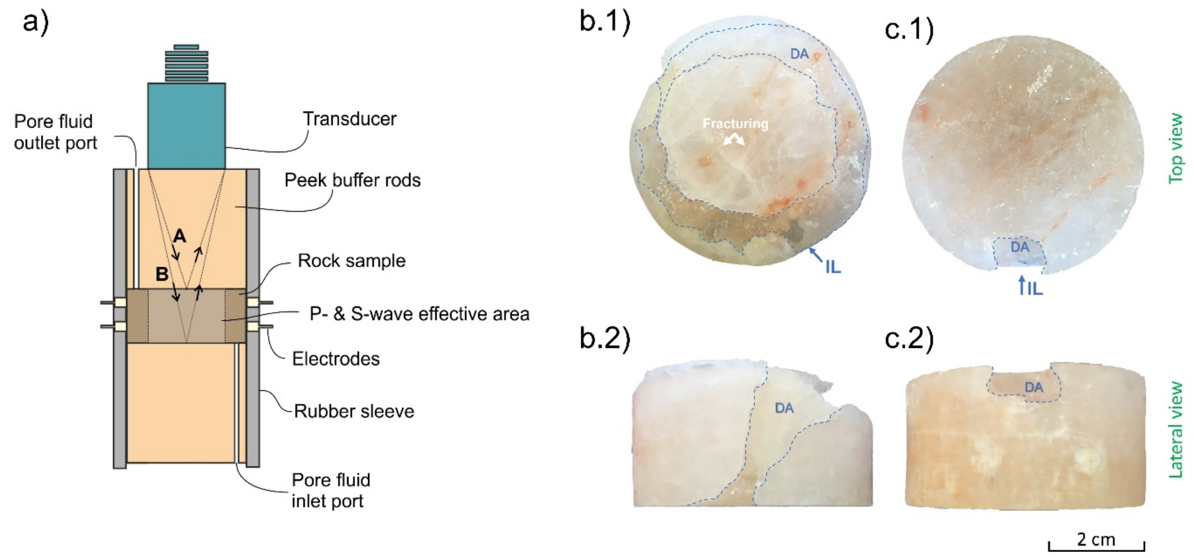

Figure 37: a) Configuration of the geophysical sensors around the rock sample in the experimental rig (*Figure 29*). Top (1) and lateral (2) view of samples (b) Pre-Cam 4 and (c) Pre-Cam 3 post-testing.

Figure 37b shows that dissolution on the Pre-Cam 4 (fractured sample) developed a peripherical channel from the inlet port – rock contact. The channelling progressed horizontally, instead of following the visual (pseudo-) vertical fracturing network (Figure 37b.1), suggesting a 3D cubic cracking network (completed by a third fracture family parallel to the basal plane) following the common cleavage planes of halite rocks (Popp et al., 2001). The basal plane could have developed as a result of the early dissolution and fracturing, as the attenuation data versus pressure (Figure 30) suggested the absence of fractures perpendicular to the wave propagation. Pre-Cam 3 post-testing shows a smaller dissolution volume near the inlet port (Figure 37), as previously observed in the electrical resistivity tomography (Figure 36). In this case, the absence of initial fracturing led to localised dissolution near the inlet, with slow diffusion backwards into the pipe system. The post-test drying suggests a total salt dissolution volume of ~6 % during the Pre-Cam 3 test, while over 25 % for Pre-Cam 4, although in the latter case this is a rough estimate due to the sample being oil-contaminated (which is only partially removable by oven-drying) during the failure of the experimental setup.

4.5 Discussions

Operating and proposed sites for UHS in salt caverns are commonly placed at depths that can lead to confining pressures above 20 MPa (Kruck et al., 2013; Zivar et al., 2020). However, the energy transition challenge will require refined storing strategies, aiming to combine CO_2 sequestration and UHS in the same area to enhance the effectivity of the whole process (Akhurst et al., 2021). This could lead to shallower UHS to enable CO_2 (much more compressible) to be stored in deeper reservoirs underneath. We have identified a turning point in the compaction trend around 15-20 MPa in our experimental data. All the measured properties change faster with effective pressure below 20 MPa (Figure 30) but inelastically, as interpreted from the high hysteresis carried by all the parameters in all samples below this pressure (Figure 31). This finding is relevant for UHS, as this strategy implies cyclic changes in P_{eff} to satisfy seasonal energy demands. Our results indicate that below 20 MPa, increasing P_{eff} (e.g., autumn-winter; depleted reservoir due to high energy demand) will lead to a safer state of the underground compartment, by enhancing the sealing (i.e., lowering permeability) and the mechanical properties of the rock (at least to 50 MPa); while decreasing the P_{eff} (e.g., spring-summer periods; larger H_2 stored due to low energy demand) would impact very little or nothing of the original conditions.

The results collected in this study agree with the limited data available in the literature for elastic and transport properties and their pressure dependency of salt rocks. The suitability of the dataset reported by Popp et al. (2001) contrast with the low pressure range (< 30 MPa) and number of measurements collected per sample. This fact hampers the statistical significance during data analysis, and limiting to some extent our interpretation about potential correlations between elastic waves and permeability. Our assessment of the elastic waves with depth shows a good fitting between both V_P and V_S, for the salt samples. Such a good correlation is particularly interesting for offshore exploration surveys, where the shear (S-) wave collection is limited by the commonly encountered low amplitude of S-waves in marine wide-angle seismic data (Falcon-Suarez et al., 2020b). Furthermore, where S-wave is available, changes in the pressure dependency V_P-V_S correlation could serve as an indicator of partial saturation, as this will affect the bulk compressibility of the rock and therefore the shape of the loading curve. Note that parameter B and D in equation (1) vary to some extent between dry and wet granular rocks (Figure 32). This possibility would be of great interest to interpret leaks from storage reservoirs through overburden formations from 4D seismic imaging (Robinson et al., 2021). However, to further analyse this possibility in halite rocks, we need to collect more experimental data under both dry and fully saturate conditions and stablish a more robust statistical analysis.

The dissolution tests on samples Pre-Cam 3 (intact) and 4 (fractured) demonstrate that even small structural discontinuities may significantly impact the dissolution patterns. Weisbrod et al. (2012) focused on the dissolution patterns of salt rock when an unsaturated solution with respect to halite flowed through the salt cores. They found that dissolution channel patterns generated were related to rock structural, mineralogic and petrographic heterogeneities (with preferential dissolution pathways in areas with cracks, i.e., larger surface areas enhancing the dissolution), flow rate and gravity. But the flow rate is only effective if an outlet for fluid escape exists (i.e., one basic requirement for dissolution to happen (Johnson, 2005)). Our results suggest that the fractures dominate the dissolution, as even an uncontrolled increase in fluid pressure (e.g., as a result of constant flow through intact salt rocks during caverning) would lead to minor (both mechanically and temporally) changes than those expected in a fractured rock with a minimum fluid pressure. In a large scale, dissolution of halite free of fractures would lead to low salt-removal rates, leading to more ductile subsidence than fractured formations, which with higher salt-removal rates may generate brittle subsidence with associated vertical fracturing (Davies, 1989).

The presence of structural discontinuities influences largely the safety of salt caverning and UHS activities. We have observed how vertical discontinuities that control fluid migration (dispersion or channelling) may lead to undetectable elastic signatures. This finding has important implications for UHS in salt formations, as the existence of seismically unseen vertical fractures might lead to undesirable uncontrolled dissolution events during caverning. One strategy could be performing completing the conventional 3D seismic data with higher-resolution multifrequency surveys (Robinson et al., 2021). Our results suggest that electrical resistivity might also contribute to the monitoring of the caverning process due to the contrast between the rock and the fluid in the pores/cavern. Although our dissolution test on the intact halite sample clearly shows the evolution of the aperture nearby the sample inlet (Figure 36), these results should be carefully interpreted, as we commenced the test from a high resistivity (dry sample) stage. Despite this circumstance amplifies the contrast between rock and pore fluid, by the end of the test (ERT 5 and 6) the rock is partially saturated and still shows a large contrast (by ~50 Ohm m) between frame and pores. However, the detection of sub vertical fractures from electromagnetic surveys would be conditioned by the low spatial resolution of the electrical methods data (Gehrmann et al., 2021), which would limit the interpretation of the actual fracture size (i.e., length and aperture).

4.6 Conclusions

We completed laboratory testing on hydromechanical properties of salt rock to develop relationships between their elastic and transport properties. We conclude from this testing that:

- Permeability spans nearly six orders magnitude from 10^{-15} to 10^{-21} m^2 for the seven samples investigated.
- A turning point in the compaction trend exists at ~15-20 MPa, with all measured properties changing faster with effective pressure below 20 MPa, but inelastically.
- By cross-plotting elastic and permeability results, we identify linear trends between all samples. The linearity is missing at high pressure (>20 MPa) for permeability and attenuation factors.

Secondly, we undertook dissolution tests to investigate the effect of rock structural heterogeneities on the dissolution. We conclude from the dissolution tests that:

- Small structural discontinuities may significantly impact the dissolution patterns.
- Salt rock with pre-existing fractures (at macro-scale) can give rise to rapid dissolution, irrespective of the fluid pore pressure or confining pressure. Here, the low permeability salt (aquiclude) is cut by a high-permeability pathway of fractures, promoting fluid transport and dissolution.

Chapter 5 Summary and Future Work

In this thesis, I undertook a numerical modelling study to understand the evolution of pore fluid overpressure through geological time in the Western and Eastern Mediterranean basins using the disequilibrium compaction mechanism.

From the initial literature review of hydromechanical properties of evaporites, I found laboratory-based permeability values ranging between 10^{-13} to 10^{-23} m^2 which undamaged salt rock was likely to be from $10^{-21}$to 10^{-23} m^2. From initial sensitivity analysis of evaporite properties on our overpressure numerical model, I showed that the broad ranges of property values found in the literature, particularly for permeability, reduced the predictive ability of our models. To reduce uncertainty in the role of evaporite deposition inducing overpressure during the Messinian Salinity Crisis (MSC) in the Mediterranean, I undertook initial laboratory testing on three salt rock samples from the Caltanissetta Basin, Sicily. Results provided permeability of fractured salt rock ranging from 10^{-13} to 10^{-16} m^2 at confining pressures from 1.5 to 17.2 MPa with connected “porosity of 1.0 to 2.0 %. Based on the uncertainties observed, our most likely overpressure scenario in the Liguro-Provençal (L-P) deep basin model used an initial permeability at seabed of 10^{-20} m^2 for the MSC Stage 2 salt rock that translated to 10^{-21} m^2 after loading of MSC Upper Unit Gypsum and Pliocene to Quaternary (PQ) units. A low compressible initial porosity at seabed of 2 % was also used for modelling of the salt rock.

After determining uncertainties identified in the Western Mediterranean study, I extended the laboratory testing work to constrain the elastic and transport properties of salt rock from globally selected samples, including the Mediterranean, where some rock properties of the Messinian evaporites were absent. Testing was undertaken on seven salt rock samples of Cambrian to Miocene age, with five samples visibly intact and two pre-fractured. Tests undertaken to 50 MPa showed permeability spans nearly six orders of magnitude and decrease in permeability with increasing pressure in all salt rock samples. Permeability results showed major changes in salt rock due to changes in effective pressure below 20 MPa. Testing undertaken on the MSC Stage 2 salt rock sample from Marianopoli, Sicily, Italy, showed permeability decrease from $7x10^{-20}$ to $3x10^{-21}$ m^2 as effective pressure increased from 5 to 50 MPa. During this study, I measured permeability of intact salt rock from 10^{-21} to 10^{-24} m^2, and not 10^{-23} m^2 as initially reported in the Western Mediterranean study. All samples showed connected porosity of 0.1 – 1.9 %, similar to the chapter 2 study.

To understand if disequilibrium compaction was a plausible mechanism that generated the existing crater pockmarks at the onset of the MSC in Eastern Mediterranean, I use salt rock properties from my laboratory study. Based on laboratory data, our most likely overpressure scenario in the Levant deep basin model used an initial permeability at seabed of 10^{-20} m^2 for the MSC salt rock and a low compressible initial porosity at seabed of 2 %, consistent with laboratory testing and modelling in the Western Mediterranean. Here, our model in the Levant basin shows that overpressure generated by loading of the MSC Stage 2 salt rock cannot explain the development of pockmark and crater features at the onset of the MSC.

I quantified the time evolution of overpressure and timing of fluid expulsion events using the disequilibrium compaction mechanism within Miocene sediment (pre-Messinian and MSC evaporites) of the Mediterranean, specifically at the Liguro- Provençal and Levant deep basins in the Western and Eastern Mediterranean, respectively. Commencing in the Middle Miocene in the Western Mediterranean (16 – 5.97 Ma) and Early Miocene in the Eastern Mediterranean (~23 – 5.97 Ma), deposition of marlstone and claystone with thicknesses ranging from 740 to 1743 m allowed pore fluid dissipation to near hydrostatic pressure. In the Eastern Mediterranean, we considered possible accumulations of methane gas trapped during the Early to Late Miocene. Here, a trapped gas accumulation of 180 m (Tamar field gas column equivalent) below an overburden of 986 m, could have developed mild gas overpressure of ~1.5 MPa. Fluid expulsion events are not observed during this time period in neither of our study areas of the Western nor Eastern Mediterranean basins. However, our uncertainty analysis in the Levant Basin shows that a gas column up to 38 m below an overburden of 74 m could trigger overpressure-induced tensile fracturing prior to deposition of the MSC.

In the Western Mediterranean, overpressure modelling was undertaken on claystone and limestone as part of Stage 1 (Lower Unit) of the MSC (5.97 - 5.6 Ma). Following loading of 661 m, overpressure of 2.1 MPa was generated within the underlying pre-Messinian sediment caused by disequilibrium compaction. Although the MSC events are assumed synchronous across deep basins (Manzi, et al., 2018), our modelling in the Levant Basin did not include an evaporite-free claystone accumulation from 5.97 - 5.6 Ma as this unit is not observed on seismic data across our study area, either because it is absent or it is below seismic resolution. During this period, fluid expulsion events were not modelled. The impact on overpressure in the Western and Eastern Mediterranean basins is greatest during deposition of the Stage 2 (Mobile Unit) of the MSC. In both basins, loading generated by deposition of ~500 m of halite caused overpressure and λ^* (ratio of overpressure to effective stress under hydrostatic conditions) to increase above a point at which fracturing may have occurred. Within the Messinian salt are groups of low frequency reflectors, separated by acoustic blanketing, bright spots and pockmarks, which evidences fluid migration.

Seismic observations of fluid migration within the Messinian salt are consistent with our modelled fluid expulsion during inter-deposition of Stage 2 (Mobile Unit) halite from ~5.58 to 5.55 Ma. However, this inter-Messinian seal failure cannot explain the development of the pockmark and crater features at the base of the MSC evaporites. To investigate pockmarks in the Levant basin, we used a 1D analytical model of chimney formation caused by gas overpressure. Here, sea-level fall at the beginning of the Messinian Salinity Crisis (MSC) of a few 10s to a few 100s m and the presence of free gas may have caused tensile seal failure and sub-vertical fluid migration to the paleo-seafloor. From our various modelling scenarios in the Western and Eastern Mediterranean basins, two main fluid expulsion events are identified during Stage 2 (Mobile Unit) of the MSC, the first during the initial commencement of the crisis from sea-level fall combined with other mechanisms of overpressure generation, and the second during inter-sediment loading of salt rock.

After the peak of the MSC, a unit of gypsum was deposited in the Western Mediterranean. Overpressure modelling was not undertaken on this unit in the Eastern Mediterranean as it is not observed on seismic data across our study area. However, in the Western Mediterranean, overpressure modelling in the Algero-Balearic basin at the base of the Emile Baudot Escarpment shows that towards the end of the MSC Stage 3, loading brought on by deposition of the Upper Unit gypsum caused overpressure and λ^* of the underlying MSC Stage 2 halite to increase above a point at which hydro fracturing may have occurred, resulting in overpressure release from within the MSC Stage 2 halite. This event is consistent with brecciated limestone in Central Mediterranean outcrop and seismic observations of polygonal faulting in the Western Mediterranean, formed at the late stage of the MSC. This could be interpreted as a third fluid expulsion event during the MSC.

5.1 Conclusions

Three aims were proposed in this PhD thesis that required the combined use of numerical modelling and laboratory experiments.

The first aim was to 'Understand, quantify and assess the time evolution and role of pore fluid overpressure on the Western Mediterranean'. In Chapter 2, we undertook numerical modelling of pore fluid overpressure due to the disequilibrium compaction mechanism on both the Liguro-Provençal basin and the Algero-Balearic basins considering time evolution of basin formation. We can conclude that i) rapid sediment loading of low permeability Messinian evaporites inhibited vertical fluid flow causing high overpressure within pre-Messinian and Messinian sequences, and ii) rapid sediment loading caused sufficient overpressure to hydro fracture MSC evaporites during Stage 2 deposition of halite (Mobile Unit) from about 5.58 to 5.55 Ma in the Liguro-Provençal basin, and during Stage 3 deposition of Upper Gypsum from 5.55 to 5.33 Ma in the Algero-Balearic basin.

The second aim was to 'Test if the crater pockmarks observed at the base of the Messinian evaporites may have been caused by fluid migration from overpressured methane gas in Miocene sediment towards the seafloor, triggered by sea-level drop at the beginning of the Messinian Salinity Crisis (MSC)'. In Chapter 3, we used a 1D analytical model of chimney formation caused by gas overpressure to explain the crater pockmarks observed at the base of the Messinian evaporites in the Levant basin. The field of pockmarks was most likely triggered by fluid migration from shallow methane gas accumulations in middle to late Miocene sediment towards the seafloor, triggered by sea-level fall at the beginning of the Messinian Salinity Crisis (MSC) of a few 10s to a few 100s m. From our quantitative modelling studies in Aims 1 and 2, we have identified a 'trilogy of high overpressure development and fluid expulsion events' during the MSC. This 'trilogy' has already been suggested based on seismic data in Mediterranean offshore basins.

The third aim was to 'Jointly analyse the geophysical (seismic-wave attributes and electrical resistivity) and transport properties of salt rocks, and develop relationships between them to investigate and remotely monitor changes in rock structure during salt rock dissolution from geophysical responses'. From our various laboratory experiments at different stages of study (Chapters 2 & 4), we show that permeability for salt rock ranges from 10^{-13} to 10^{-21} m^2 for effective pressures from 1.5 to 50 MPa, with the main changes occurring below 20 MPa. This broad range can highly reduce the predictive ability of overpressure from numerical models. By cross-plotting elastic and transport properties of salt rock, we identify linear trends between samples, however fitting parameters for permeability correlate poorly with V_p. Finally, from dissolution tests under pressure of confinement, salt rock with pre-existing fractures can give rise to rapid dissolution irrespective of fluid pore pressure or confining pressure.

5.2 Limitations of the research

Several limitations are identified for the 1-D models and the laboratory testing project.

I present a 1-D modelling study in Chapter 2 to calculate overpressure generation by the disequilibrium compaction model through geological time. Three limitations are recognized here. Firstly, 1-D overpressure modelling cannot account for lateral rock property and fluid flow variations in a geological system that is most likely influenced by 2-D or 3-D structures. However, in the Mediterranean, few boreholes have intersected through the thick evaporite units of the MSC to provide adequate rock property information and spatial variations in the evaporites and pre-Messinian clastic sequences. As wellbores typically do not obtain measurements like permeability within salt, critical to this study, the high degree of uncertainty in parameters arguably provide greater uncertainty in 2-D and 3-D models. Secondly, I undertook modelling over relatively undeformed layers of the Western Mediterranean basin to exclude the impact from tectonic compression. In certain areas of the Western Mediterranean deep basin, tectonic compression is observed from seismic. Here, exists a limitation in our study by not incorporating this mechanism that likely affects the evolution of deformation and salt flow, stress and pore fluid pressure to further understand the overprint of overpressure in areas of the basin from late Pliocene deformation. Thirdly, we treat the salt rock as brittle material, once a fracture is generated it remains open. However, for salt rock, because of its ductile nature under certain conditions, the salt can flow and close micro-fractures generated.

In Chapter 3 I present a second 1-D analytical model on vertical migration caused by gas overpressure. A key limitation is recognised here. When a porous medium is not rigid, interplays exist between fluid flow and mechanics of deformation of the solid (Juanes, et al., 2020). Here, grain-scale mechanisms control morphological patterns, relevant from pore to geological scale and spatially (Juanes, et al., 2020). In this study I do not account for this interplay. Because of the approach used, the results should be interpreted with caution. They provide a good estimate of the order of magnitude of sea level drop able to generate such gas chimney and time of propagation.

I present a laboratory testing project in Chapter 4 that evaluates elastic and transport properties of salt rock and changes in these properties during salt dissolution. Four limitations are recognized here. Firstly, our experimental setup does not allow to measure permeabilities below 10^{-21} m^2. Then, initial concept testing of salt dissolution was planned on two synthetic samples (one intact and the other fractured) prior to commencing dissolution testing on real core samples of Cambrian to Miocene age. With termination of this study early, due to failure of the rubber sealing sleeve that protects the rock from oil entering the system, I was able to undertake dissolution testing on two synthetic samples only. As a consequence, results and conclusions are limited here. Also related to the termination of this study, initial concept testing was undertaken with initial effective pressure of 15 MPa (with minimum pore pressure of 0.1 MPa). I was unable to undertake further testing with various pore pressures to understand the impact pore pressure plays on the dissolution of salt rock. Finally, and again related to termination of this study, the plan after concept testing was to undertake further testing with various fluid medium / saturation levels of <1,000 (freshwater), 35,000 (freshwater) and potentially 250,000 ppm (highly saturated brine) to understand the impact salinity plays on the dissolution of salt rock. With this was a desire to evaluate what coupled relationship may exist between saturation levels and pore pressure on dissolution using geophysical responses.

5.3 Future Work

In this thesis, I present a 1D numerical model on overpressure generation by the disequilibrium compaction model in the Western Mediterranean. One of the limitations highlighted was neglecting to model overpressure generated from the evolution of deformation and salt flow. In the Liguro-Provençal (L-P) basin, salt-related structures and diapirs are present in several regions attributed to gravity sliding and spreading of Plio-Pleistocene sediment above Messinian evaporites. Future considerations should include developing a 2D/ 3D model on deformation, stress and pore pressure in an area like the Gulf of Lions where proximal (upslope) extension to distal (downslope) contraction exists (Maillard, 2003). Here, developing a model to spatially understand the impact of differential loading, overpressure development and lateral/ vertical fluid migration within the MSC lower unit (LU) and pre-Messinian units that exist below a thick deformed Messinian evaporitic unit, may provide new insights on the overprint impact and lateral variations of pore fluid overpressure caused deformation, that our 1D model cannot provide. Further scope may include assessing the impact the extensive Messinian diapir province trending northeast-southwest in the Liguro-Provençal (L-P) basin and perpendicular to the slope direction (Maillard, 2003) may play spatially on overpressure development and fluid migration.

In this thesis, I present a 1D analytical model of chimney formation caused by gas overpressure. The focus was on overpressure generation associated with sea-level fall. However, in the Levant Basin, an irregular erosional surface exists towards the base of the Messinian salt traced upslope to canyons on the basin margin (Manzi et al., 2018; Bertoni & Cartwright, 2005). To determine the impact and importance that not only sea level fall but erosion may have played on fluid overpressuring at the onset of the MSC in middle to late Miocene sediment, a 2D model that spatially estimates overpressure generated for erosion between the deep basin to continental margin may be developed.

In this thesis, I present a joint analysis on geophysical and transport properties of salt rock along with changes in rock structure during salt rock dissolution. Investigation into the impact of dissolution using geophysical signature was terminated when failure of the rig equipment occurred under high confinement pressure. Future considerations for this work include 1) focusing on when dissolution effectively takes place for a given pore pressure, and 2) testing a given pore pressure with various fluid medium/ saturation levels. To understand when effective dissolution takes place, each test should use a constant pore pressure rate rather than increasing pore pressure in stepwise increments. The decision on fluid medium/ saturation level to use depends largely on the salinity within the aquifer of a study area. However, understanding the impact between fresh and saltwater would be a nice comparison study. Finally, none of the above can be progressed without finding a solution for the tear of the rubber sealing sleeve during dissolution. Three possible changes may be 1) increase the thickness or change the material of the sleeve (e.g., from rubber to plastic), 2) test only intact (non-cracked) samples to reduce the chance of rapid dissolution occurring during the initial stage of testing, and 3) monitor the dissolution behaviour in real-time using geophysical data (e.g., resistivity or Vp/Vs trends), terminating the test as soon as effective dissolution occurs. It is also recommended that future tests commence with synthetic salt rock to constrain the cut-off for effective dissolution and in the scenario of rig failure again, prior to progressing with natural samples.

References

Akhurst, M., Pearce, J., Sunny, N., Shah, N., Goldthorpe, W., Avignon, L., 2021. Tools and options for hydrogen and CCS cluster development and acceleration – UK case study, ELEGANCY project. Proceedings of the 15th Greenhouse Gas Control Technologies Conference 15-18 March 2021.

Al-Balushi, A. N., Neumaier, M., Fraser, A. J., & Jackson, C. A. L. (2016). The impact of the Messinian salinity crisis on the petroleum system of the Eastern Mediterranean: a critical assessment using 2D petroleum system modelling. Petroleum Geoscience, 22(4), 357-379. doi:10.1144/petgeo2016-054

Algar, C. K., Boudreau, B. P., & Barry, M. A. (2011). Initial rise of bubbles in cohesive sediments by a process of viscoelastic fracture. Journal of Geophysical Research: Solid Earth, 116(B4). doi:https://doi.org/10.1029/2010JB008133

Allen, P. A., & Allen, J. R. (2013). Basin Analysis: Principles and Application to Petroleum Play Assessment: Wiley.

Amalokwu, K., Best, A.I., Sothcott, J., Chapman, M., Minshull, T., Li, X.-Y., 2014. Water saturation effects on elastic wave attenuation in porous rocks with aligned fractures. Geophysical Journal International 197, 943-947, https://doi.org/10.1093/gji/ggu076.

Anderson, R.Y., Kirkland, D.W., 1980. Dissolution of salt deposits by brine density flow. Geology 8, 66-69, 10.1130/0091-7613(1980)8<66:dosdbb>2.0.co;2.

Arab, M., Belhai, D., Granjeon, D., Roure, F., Arbeaumont, A., Rabineau, M., . . . Deverchere, J. (2016). Coupling stratigraphic and petroleum system modeling tools in complex tectonic domains: case study in the North Algerian Offshore. Arabian Journal of Geosciences, 9(4), 289. doi:10.1007/s12517-015-2296-3

ASTM D4404-84 (2004), Standard Test Method for Determination of Pore Volume and Pore Volume Distribution of Soil and Rock by Mercury Intrusion Porosimetry, ASTM International, West Conshohocken, PA, 2004, www.astm.org

Balkan, E., Erkan, K., & Şalk, M. (2017). Thermal conductivity of major rock types in western and central Anatolia regions, Turkey. Journal of Geophysics and Engineering, 14(4), 909-919. doi:10.1088/1742-2140/aa5831

Barabasch, J., Ducros, M., Hawie, N., Bou Daher, S., Nader, F. H., & Littke, R. (2019). Integrated 3D forward stratigraphic and petroleum system modeling of the Levant Basin, Eastern Mediterranean. *Basin Research, 31*(2), 228-252. doi:https://doi.org/10.1111/bre.12318

Beauheim, R. L., Saulnier Jr, G. J., & Avis, J. D. (1991). *Interpretation of Brine-Permeability Tests of the Salado Formation at the Waste Isolation Pilot Plant Site: First Interim Report*. United States. doi:10.2172/6026281.

Beauheim, R. L., & Roberts, R. M. (2002). Hydrology and hydraulic properties of a bedded evaporite formation. Journal of Hydrology, 259(1), 66-88. doi:https://doi.org/10.1016/S0022-1694(01)00586-8

Bein, A.& Gvitzman, G. (1997). A Mesozoic fossil edge of the Arabian plate along the Levant coastline and its bearing on the evolution of the eastern Mediterranean. In: Biju-Duval, B. & Montadert, L. (eds.) Structural History of the Mediterranean Basins. Technip, Paris, 95-110.

Ben-Avraham, Z. (1989). Multiple opening and closing of the Eastern Mediterranean and South China Basins. Tectonics, 8, 351-362.

Ben-Gai, Y. (2021). The world unique triangular shaped Jonah High in the Levant Basin, eastern mediterranean – Tectonic setting, stratigraphy and exploration considerations. Marine and Petroleum Geology, 132, 105206. doi:https://doi.org/10.1016/j.marpetgeo.2021.105206

Ben Moshe, L., Ben-Avraham, Z., Enzel, Y., & Schattner, U. (2020). Estimating drawdown magnitudes of the Mediterranean Sea in the Levant basin during the Lago Mare stage of the Messinian Salinity Crisis. Marine Geology, 427, 106215. doi:https://doi.org/10.1016/j.margeo.2020.106215

Benson, R. H., Rakic-El Bied, K., & Bonaduce, G. (1991). An important current reversal (influx) in the Rifian Corridor (Morocco) at the Tortonian-Messinian boundary: The end of Tethys Ocean. Paleoceanography, 6(1), 165-192. doi:https://doi.org/10.1029/90PA00756

Bertoni, C., & Cartwright, J. (2005). 3D seismic analysis of circular evaporite dissolution structures, Eastern Mediterranean. Journal of The Geological Society - J GEOL SOC, 162, 909-926. doi:10.1144/0016-764904-126

Bertoni, C., & Cartwright, J. A. (2006). Controls on the basinwide architecture of late Miocene (Messinian) evaporites on the Levant margin (Eastern Mediterranean). *Sedimentary Geology*, *188*, 93-114.

Bertoni, C., & Cartwright, J. A. (2007). Major erosion at the end of the Messinian Salinity Crisis: evidence from the Levant Basin, Eastern Mediterranean. Basin Research, 19(1), 1-18. doi:https://doi.org/10.1111/j.1365-2117.2006.00309.x

Bertoni, C., Cartwright, J., & Hermanrud, C. (2013). Evidence for large-scale methane venting due to rapid drawdown of sea level during the Messinian Salinity Crisis. Geology, 41(3), 371-374. doi:10.1130/g33987.1

Bertoni, C., Cartwright, J. (2015). Messinian evaporites and fluid flow. Marine and Petroleum Geology. Marine and Petroleum Geology, 66(1), 165-176. doi:10.1016/j.marpetgeo.2015.02.003

Boudreau, B. (2012). The physics of bubbles in surficial, soft, cohesive sediments. Marine and Petroleum Geology, 38, 1-18. doi:10.1016/j.marpetgeo.2012.07.002

Brace, W. F., Walsh, J. B., & Frangos, W. T. (1968). Permeability of granite under high pressure. Journal of Geophysical Research (1896-1977), 73(6), 2225-2236. doi:10.1029/JB073i006p02225

Bredehoeft, J. D. (1988). Will salt repositories be dry? Eos, Transactions American Geophysical Union, 69(9), 121-131. doi:10.1029/88eo00078

Brodsky, N.S. (1994). Hydrostatic and shear consolidation tests with permeability measurements on Waste Isolation Pilot Plant crushed salt. United States. doi:10.2172/10142397.

Buchbinder, B., & Zilberman, E. (1997). Sequence stratigraphy of Miocene-Pliocene carbonate-siliciclastic shelf deposits in the eastern Mediterranean margin (Israel): effects of eustasy and tectonics. Sedimentary Geology, 112(1), 7-32. doi:https://doi.org/10.1016/S0037-0738(97)00034-1

Burollet, P. F., Said, A., & Trouve, P. (1978). Slim holes drilled on the Algerian Shelf. Leg 42B, Istanbul, Turkey, May-June 1975, 42, 1181.

Butler, R. W. H., Lickorish, W. H., Grasso, M., Pedley, H. M., & Ramberti, L. (1995). Tectonics and sequence stratigraphy in Messinian basins, Sicily: Constraints on the initiation and termination of the Mediterranean salinity crisis. GSA Bulletin, 107(4), 425-439. doi:10.1130/0016-7606(1995)107<0425:tassim>2.3.co;2

Callow, B., Falcon-Suarez, I., Ahmed, S., & Matter, J. (2018). Assessing the carbon sequestration potential of basalt using X-ray micro-CT and rock mechanics. International Journal of Greenhouse Gas Control, 70, 146-156. doi:https://doi.org/10.1016/j.ijggc.2017.12.008

Camerlenghi, A. and Aloisi, V., 2020. Uncovering the Mediterranean Salt Giant (MEDSALT)-Scientific networking as incubator of cross-disciplinary research in Earth Sciences. *European Review*, *28*(1), pp.40-61.

Cartwright, J., Kirkham, C., Foschi, M., Hodgson, N., Rodriguez, K., & James, D. (2021). Quantitative reconstruction of pore-pressure history in sedimentary basins using fluid escape pipes. Geology, 49(5), 576-580. doi:10.1130/G48406.1

Cartwright, J., & Santamarina, C. (2015). Seismic characteristics of fluid escape pipes in sedimentary basins: Implications for pipe genesis. *Marine and Petroleum Geology*, *65*, 126–140. https://doi.org/https://doi.org/10.1016/j.marpetgeo.2015.03.023

Capella, W., Spakman, W., van Hinsbergen, D. J. J., Chertova, M. V., & Krijgsman, W. (2020). Mantle resistance against Gibraltar slab dragging as a key cause of the Messinian Salinity Crisis. Terra Nova, 32(2), 141-150. doi:10.1111/ter.12442

Carminati, E., Doglioni, C., Gelabert, B., Panza, G., Raykova, R., & Roca, E. (2011). 18.4.1 Evolution of the Western Mediterranean.

Casas, E., & Lowenstein, T. K. (1989). Diagenesis of saline pan halite; comparison of petrographic features of modern, Quaternary and Permian halites. Journal of Sedimentary Research, 59(5), 724-739. doi:10.1306/212f905c-2b24-11d7-8648000102c1865d

Cathles, L. M., Su, Z., & Chen, D. (2010). The physics of gas chimney and pockmark formation, with implications for assessment of seafloor hazards and gas sequestration. Marine and Petroleum Geology, 27(1), 82-91. doi:https://doi.org/10.1016/j.marpetgeo.2009.09.010

Cherchi, A., Mancin, N., Montadert, L., Murru, M., Putzu, M. T., Schiavinotto, F., & Verrubbi, V. (2008). The stratigraphic response to the Oligo-Miocene extension in the western Mediterranean from observations on the Sardinia graben system (Italy). Bulletin de la Société Géologique de France, 179(3), 267-287. doi:10.2113/gssgfbull.179.3.267

Chilingar, G. & Fertl, W. & Rieke, Herman & ROBERTSONJR, J. (2002). Chapter 8 Tectonics and overpressured formations. Developments in Petroleum Science. 50. 191-208. 10.1016/S0376-7361(02)80029-2.

CIESM (2008). The Messinian Salinity Crisis from mega-deposits to microbiology - A consensus report. N° 33 in CIESM Workshop Monographs [F. Briand, Ed.], 168 p., CIESM Publisher, Monaco.

Clauzon, G., Suc, J.-P., Gautier, F. o., Berger, A., & Loutre, M.-F. (1996). Alternate interpretation of the Messinian salinity crisis: Controversy resolved? Geology, 24(4), 363-366. doi:10.1130/0091-7613(1996)024<0363:aiotms>2.3.co;2

Comas, M. C., Zahn, R., Klaus, A., Aubourg, C., Belanger, P. E., Bernasconi, S. M., . . . Wilkens, R. H. (1996). Site 975. Proceedings of the Ocean Drilling Program; initial reports; Mediterranean Sea II, the western Mediterranean; covering Leg 161 of the cruises of the drilling vessel JOIDES Resolution, Naples, Italy to Málaga, Spain, sites 974-979, 3 May-2 July 1995, 161, 113

Cooper, A.H., 2002. Halite karst geohazards (natural and man-made) in the United Kingdom. Environmental Geology 42, 505-512, 10.1007/s00254-001-0512-9.

Cosenza, P., Ghoreychi, M., 1997. Permeability evolution of rock salt under mechano-chemical stresses. Bulletin de la Societe Geologique de France 168, 313-324.

Daigle, H., Cook, A., Fang, Y., Bihani, A., Song, W., & Flemings, P. B. (2020). Gas-Driven Tensile Fracturing in Shallow Marine Sediments. Journal of Geophysical Research: Solid Earth. https://doi.org/https://doi.org/10.1029/2020JB020835

Dal Cin, M., Del Ben, A., Mocnik, A., Accaino, F., Geletti, R., Wardell, N., . . . Camerlenghi, A. (2016). Seismic imaging of Late Miocene (Messinian) evaporites from Western Mediterranean back-arc basins. Petroleum Geoscience, 22(4), 297-308. doi:10.1144/petgeo2015-096

Dale, M.S., Falcon-Suarez, I.H., Marín-Moreno, H., 2021a. Geophysical response to dissolution of undisturbed and fractured evaporite rock during brine flow, EGU General Assembly 2021, online, pp. EGU21-15572.

Dale, M.S., Marín-Moreno, H., Falcon-Suarez, I.H., Grattoni, C., Bull, J.M., McNeill, L.C., 2021b. The Messinian Salinity Crisis as a trigger for high pore pressure development in the Western Mediterranean. Basin Research 33, 2202– 2228, https://doi.org/10.1111/bre.12554.

Davies, P.B., 1989. Assessing deep-seated dissolution-subsidence hazards at radioactive-waste repository sites in bedded salt. Engineering Geology 27, 467-487, https://doi.org/10.1016/0013-7952(89)90042-2.

Dewey, J. F., Pitman, W. C., III, Ryan, W. B. F., & Bonnin, J. (1973). Plate Tectonics and the Evolution of the Alpine System. GSA Bulletin, 84(10), 3137-3180. doi:10.1130/0016-7606(1973)84<3137:ptateo>2.0.co;2

Domski, P.S., Upton, D.T., Beauheim, R.L., (1996). Hydraulic Testing Around Room Q: Evaluation of the Effects of Mining on the Hydraulic Properties of Salado Evaporites, SAND96-0435, Sandia National Laboratories, Albuquerque, NM.

Driussi, O., Maillard, A., Ochoa, D., Lofi, J., Chanier, F., Gaullier, V., . . . Garcia, M. (2015). Messinian Salinity Crisis deposits widespread over the Balearic Promontory: Insights from new high-resolution seismic data. Marine and Petroleum Geology, 66, 41-54. doi:https://doi.org/10.1016/j.marpetgeo.2014.09.008

Druckman, Y., Buchbinder, B., Martinotti, G. M., Tov, R. S., & Aharon, P. (1995). The buried Afiq Canyon (eastern Mediterranean, Israel): a case study of a Tertiary submarine canyon exposed in Late Messinian times. Marine Geology, 123(3), 167-185. doi:https://doi.org/10.1016/0025-3227(94)00127-7

Dusseault, Maurice & Maury, Vincent & Sanfilippo, Francesco & Santarelli, Frdric. (2004). Drilling Around Salt: Risks, Stresses, And Uncertainties.

Eberhart-Phillips, D., Han, D.-H., Zoback, M.D., 1989. Empirical relationships among seismic velocity, effective pressure, porosity, and clay content in sandstone. Geophysics 54, 82-89, http://library.seg.org/doi/abs/10.1190/1.1442580.

Eckstein, Y. (1978). Review of heat flow data from the eastern Mediterranean region. pure and applied geophysics, 117(1), 150-159. doi:10.1007/BF00879742

Ehgartner, B., Neal, J., & Hinkebein, T. (1998). *Gas releases from salt* (No. SAND-98-1354). Sandia National Lab.(SNL-NM), Albuquerque, NM (United States).

El-Bassiony, A., Kumar, J., & Martin, T. (2018). Velocity model building in the major basins of the eastern Mediterranean Sea for imaging regional prospectivity. The Leading Edge, 37(7), 519-528. doi:10.1190/tle37070519.1Erickson, A. J., & Von Herzen, R. P. (1978). Down-hole temperature measurements, Deep Sea Drilling Project, Leg 42A. Leg 42, Part 1, of the cruises of the Drilling Vessel Glomar Challenger; Malaga, Spain, to Istanbul, Turkey, April-May 1975, 42, 857.

Erickson, A. J., Montadert, L., Garrison, R. E., Fabricius, F. H., Mueller, C., Cita, M. B., . . . Worstell, P. J. (1978). Leg 42A physical properties data . *Initial Reports of the Deep Sea Drilling Project, Vol. 42*, p.1199-1206. doi:10.2973/dsdp.proc.42-1.app6.1978

Eruteya, O. E., Waldmann, N., Schalev, D., Makovsky, Y., & Ben-Avraham, Z. (2015). Intra- to post-Messinian deep-water gas piping in the Levant Basin, SE Mediterranean. Marine and Petroleum Geology, 66, 246-261. doi:10.1016/j.marpetgeo.2015.03.007

Ezersky, M., Goretsky, I., 2014. Velocity–resistivity versus porosity–permeability inter-relations in Dead Sea salt samples. Engineering Geology 183, 96-115, 10.1016/j.enggeo.2014.09.009.

Falcon-Suarez, I., Bayrakci, G., Minshull, T.A., J.L., N., Best, A.I., Rouméjon, S., IODP-Expedition-357-Science-Party, 2017. Elastic and electrical properties and permeability of serpentinites from Atlantis Massif, Mid-Atlantic Ridge. Geophysical Journal International 211, 708–721, 10.1093/gji/ggx341.

Falcon-Suarez, I.H., Livo, K., Callow, B., Marin-Moreno, H., Prasad, M., Best, A.I., 2020a. Geophysical early warning of salt precipitation during geological carbon sequestration. Scientific Reports 10, 16472, https://doi.org/10.1038/s41598-020-73091-3.

Falcon-Suarez, I.H., North, L., Callow, B., Bayrakci, G., Bull, J., Best, A., 2020b. Experimental assessment of the stress-sensitivity of combined elastic and electrical anisotropy in shallow reservoir sandstones. Geophysics 85, MR271, https://doi.org/10.1190/geo2019-0612.1.

Fauria, K. E., & Rempel, A. W. (2011). Gas invasion into water-saturated, unconsolidated porous media: Implications for gas hydrate reservoirs. Earth and Planetary Science Letters, 312(1), 188-193. doi:https://doi.org/10.1016/j.epsl.2011.09.042

Feng, Y., Yankelzon, A., Steinberg, J., & Reshef, M. (2016). Lithology and characteristics of the Messinian evaporite sequence of the deep Levant Basin, eastern Mediterranean. Marine Geology, 376. doi:10.1016/j.margeo.2016.04.004

Fernandez-Ibanez, F., & Soto, J. (2017). Pore pressure and stress regime in a thick extensional basin with active shale diapirism (western Mediterranean). AAPG Bulletin, 101, 233-264. doi:10.1306/07131615228

Finetti, I., & Del Ben, A. (2005). Crustal Tectono-stratigraphy of te Ionian Sea from New Integrated CROP Seismic Data. In I.Finetti (Ed.), *CROP Project: Deep seismic exploration of the central Mediterranean and Italy*. Atlases in Geoscience 1 (pp.1-30). Amsterdam, the Netherlands: Elsevier Science.

Finn, R. (1999). Capillary Surface Interfaces. Notices of the American Mathematical Society, 46(7), 770-781.

Fokker, P.A., 1995. The Behaviour of Salt and Salt Caverns.

Fraser, A., Guderjahn, C.G., Allen, H. & Al-Balushi, A. 2011. The Messinian Salinity Crisis: Impact on prospectivity in the E. Mediterranean. Paper presented at the AAPG International Conference and Exhibition, 23–26 October 2011, Milan, Italy

Freund, D., 1992. Ultrasonic compressional and shear velocities in dry clastic rocks as a function of porosity, clay content, and confining pressure. Geophysical Journal International 108, 125-135, 10.1111/j.1365-246X.1992.tb00843.x.

Frizon de Lamotte, D., Raulin, C., Mouchot, N., Wrobel-Daveau, j.-c., Christian, B., & Ringenbach, J.-C. (2011). The southernmost margin of the Tethys realm during the

Mesozoic and Cenozoic: Initial geometry and timing of the inversion processes. Tectonics, 30. doi:10.1029/2010TC00269

Gardosh, M. A., & Druckman, Y. (2006). Seismic stratigraphy, structure and tectonic evolution of the Levantine Basin, offshore Israel. Geological Society, London, Special Publications, 260(1), 201-227. doi:10.1144/gsl.sp.2006.260.01.09

Gardosh, M. A., Garfunkel, Z., Druckman, Y., & Buchbinder, B. (2010). Tethyan rifting in the Levant Region and its role in Early Mesozoic crustal evolution.

Garfunkel, Z. (1998). Constrains on the origin and history of the Eastern Mediterranean basin. Tectonophysics, 298, 5-35.

Gargani, J., & Rigollet, C. (2007). Mediterranean Sea level variations during the Messinian salinity crisis. Geophysical Research Letters, 34(10). doi:https://doi.org/10.1029/2007GL029885

Garrison, R. E., Schreiber, B. C., Bernoulli, D., Fabricius, F. H., Kidd, R. B., & Melieres, F. (1978). Sedimentary petrology and structures of Messinian evaporitic sediments in the Mediterranean Sea, Leg 42A, Deep Sea Drilling Project. Leg 42, Part 1, of the cruises of the Drilling Vessel Glomar Challenger; Malaga, Spain, to Istanbul, Turkey, April-May 1975, 42, 571.

Gehrmann, R.A.S., Provenzano, G., Bottner, C., Marin-Moreno, H., Bayrakci, G., Tan, Y.Y., Naima K. Yilo, Weitemeyer, K.A., Minshull, T.A., Bull, J.M., Berndt, C., 2021. Porosity and free gas estimates from controlled source electromagnetic data at the Scanner Pockmark in the North Sea. Submitted for publication.

Gevantman, L.H. & Lorenz, J. & Haas, J.L. & Clynne, Michael & Potter, R.W.. (1981). Physical Properties Data for Rock Salt.

Giles, M. R. (1997). Diagenesis: A quantitative perspective: Implications for basin modelling and rock property prediction: Springer.

Gloyna, E.F., Reynolds, T.D., 1961. Permeability measurements of rock salt. Journal of Geophysical Research (1896-1977) 66, 3913-3921, https://doi.org/10.1029/JZ066i011p03913.

Govers, R. (2009). Choking the Mediterranean to dehydration: The Messinian salinity crisis. Geology, 37(2), 167-170. doi:10.1130/g25141a.1

Gvirtzman, Z., Manzi, V., Calvo, R., Gavrieli, I., Gennari, R., Lugli, S., Reghizzi, M., Roveri, M. (2017). Intra-Messinian truncation surface in the Levant Basin explained by subaqueous dissolution. Geology. 45. 10.1130/G39113.1.

Gvirtzman, Z., Heida, H., Garcia-Castellanos, D. *et al.* Limited Mediterranean sea-level drop during the Messinian salinity crisis inferred from the buried Nile canyon. *Commun Earth Environ* **3**, 216 (2022). https://doi.org/10.1038/s43247-022-00540-4

Haq, B., Gorini, C., Baur, J., Moneron, J., & Rubino, J.-L. (2020). Deep Mediterranean's Messinian evaporite giant: How much salt? Global and Planetary Change, 184, 103052. doi:https://doi.org/10.1016/j.gloplacha.2019.103052

Hardie, L. A., & Lowenstein, T. K. (2004). Did the Mediterranean Sea Dry Out During the Miocene? A Reassessment of the Evaporite Evidence from DSDP Legs 13 and 42A Cores. Journal of Sedimentary Research, 74(4), 453-461. doi:10.1306/112003740453

Hart, B. S., Flemings, P. B., & Deshpande, A. (1995). Porosity and pressure: Role of compaction disequilibrium in the development of geopressures in a Gulf Coast Pleistocene basin. Geology, 23(1), 45-48. doi:10.1130/0091-7613(1995)023<0045:paproc>2.3.co;2

Hawie, N., Deschamps, R., Granjeon, D., Nader, F., Gorini, C., Müller, C., . . . Baudin, F. (2015). Multi-scale constraints of sediment source to sink systems in frontier basins: a forward stratigraphic modeling case study of the Levant region. Basin Research, 29. doi:10.1111/bre.12156

Halkjelsvik ME (2012) Exploration models for dry and underfilled traps in the western part of the Hammerfest Basin. MS thesis, University of Bergen, Norway

Hermanrud, C., Venstad, J. M., Cartwright, J., Rennan, L., Hermanrud, K., & Nordgård Bolås, H. M. (2013). Consequences of Water Level Drops for Soft Sediment Deformation and Vertical Fluid Leakage. Mathematical Geosciences, 45(1), 1-30. doi:10.1007/s11004-012-9435-0

Hsü, K., Ryan, W. & Cita, M. Late Miocene Desiccation of the Mediterranean. Nature 242, 240–244 (1973). https://doi.org/10.1038/242240a0

Hsü, K., Montadert, L., Bernouilli, D., Cita, M., Erikson, A., Garrison, R., . . . Wright, R. (1977). History of the Messinian Salinity Crisis. Nature, 267, 399-403. doi:10.1038/267399a0

Hsü, K. J., Montadert, L., Bernoulli, D., Bizon, G., Cita, M. B., Erickson, A. J., . . . Worstell, P. J. (1978). Site 371; South Balearic Basin . *Initial Reports of the Deep Sea Drilling Project, Vol. 42*, p.29-57. doi:10.2973/dsdp.proc.42-1.102.1978

Hsü, K. J., Montadert, L., Bernoulli, D., Bizon, G., Cita, M. B., Erickson, A. J., . . . Worstell, P. J. (1978). Site 372; Menorca Rise . *Initial Reports of the Deep Sea Drilling Project, Vol. 42*, p.59-150. doi:10.2973/dsdp.proc.42-1.103.1978

Iadanza, A., Sampalmieri, G., Cipollari, P., Mola, M., & Cosentino, D. (2013). The "Brecciated Limestones" of Maiella, Italy: Rheological implications of hydrocarbon-charged fluid migration in the Messinian Mediterranean Basin. Palaeogeography, Palaeoclimatology, Palaeoecology, 390, 130-147. doi:https://doi.org/10.1016/j.palaeo.2013.05.033

Iona, Athanasia & Theodorou, Athanasios & Sofianos, Sarantis & Watelet, Sylvain & Troupin, Charles & Beckers, Jean-Marie. (2018). Mediterranean Sea climatic indices: Monitoring long-term variability and climate changes. Earth System Science Data. 10. 1829-1842. 10.5194/essd-10-1829-2018.

Jiménez-Moreno, G., Pérez-Asensio, J. N., Larrasoaña, J. C., Aguirre, J., Civis, J., Rivas-Carballo, M. R., . . . González-Delgado, J. A. (2013). Vegetation, sea-level, and climate changes during the Messinian salinity crisis. GSA Bulletin, 125(3-4), 432-444. doi:10.1130/b30663.1

Jobmann, M., Müller, C., & Schirmer, S. (2015). Remaining Porosity and Permeability of Compacted Crushed Rock Salt Backfill in a HLW Repository: Final Report : DBE Technology Contribution: DBE Technology GmbH.

Johnson, K., 1989. Development of the Wink Sink in west Texas, USA, due to salt dissolution and collapse. Environmental Geology and Water Sciences 14, 81-92, 10.1007/BF01728499.

Johnson, K., 2005. Subsidence hazards due to evaporite dissolution in the United States. Environmental Geology 48, 395-409, 10.1007/s00254-005-1283-5.

Jolivet, L., Augier, R., Robin, C., Suc, J.-P., & Rouchy, J. M. (2006). Lithospheric-scale geodynamic context of the Messinian salinity crisis. Sedimentary Geology, 188-189, 9-33. doi:https://doi.org/10.1016/j.sedgeo.2006.02.004

Jones, S. C. (1997). A Technique for Faster Pulse-Decay Permeability Measurements in Tight Rocks. Society of Petroleum Engineers. doi:10.2118/28450-PA

Juanes, Ruben & Meng, Yue & Primkulov, Bauyrzhan. (2020). Multiphase flow and granular mechanics. Physical Review Fluids. 5. 10.1103/PhysRevFluids.5.110516.

Kaselow, A., Shapiro, S.A., 2004. Stress sensitivity of elastic moduli and electrical resistivity in porous rocks. Journal of Geophysics and Engineering 1, 1.

Kim, Y., & Lee, E. Y. (2018). Numerical analysis of sedimentary compaction: Implications for porosity and layer thickness variation. 54, 631-640. doi:10.14770/jgsk.2018.54.6.631

Kirkham, Christopher & Bertoni, Claudia & Cartwright, Josef & Lensky, Nadav & Sirota, Ido & Rodriguez, Karyna & Hodgson, Neil. (2019). The demise of a 'salt giant' driven by uplift and thermal dissolution. Earth and Planetary Science Letters. EPSL_115933. 10.1016/j.epsl.2019.115933.

Kirkham, Christopher & Cartwright, Joe & James, David & Kearney, Luke. (2022). Episodic venting of extreme subsalt overpressure through a thick evaporitic seal. Marine and Petroleum Geology. 142. 105741. 10.1016/j.marpetgeo.2022.105741.

Klee, G.,Rummel, F. (2007). Gateway LNG Storage Project: Hydraulic / Hydrofrac Testing in Borehole Gateway-1e. MeSy GEO-MeB Systeme report. Final Report Part I: Results of in - situ Tests, Report No. : 09.07A, 86 pp.

Klimchouk, A. (1996). The dissolution and conversion of Gypsum and Anhydrite. International Journal of Speleology, 25. 21-36. doi:10.5038/1827-806X.25.3.2

Klinkenberg, L. J. (1941). The Permeability Of Porous Media To Liquids And Gases. Drilling and Production Practice, pp. 14, American Petroleum Institute, New York, New York.

Krijgsman, W., Hilgen, F. J., Raffi, I., Sierro, F. J., & Wilson, D. S. (1999). Chronology, causes and progression of the Messinian salinity crisis. Nature, 400(6745), 652-655. doi:10.1038/23231

Krijgsman, W., & Meijer, P. T. (2008). Depositional environments of the Mediterranean “Lower Evaporites” of the Messinian salinity crisis: Constraints from quantitative analyses. Marine Geology, 253(3), 73-81. doi:https://doi.org/10.1016/j.margeo.2008.04.010

Kröhn, K.-P., Czaikowski, O., Wieczorek, K., Zhang, C.-L., Moog, H., Friedenberg, L., . . . Schirmer, S. (2017). Mechanical and hydraulic behaviour of compacting crushed salt backfill at low porosities Project REPOPERM Phase 2 (978-3-946607-32-8). Retrieved from Germany: http://inis.iaea.org/search/search.aspx?orig_q=RN:48084640

Kröhn, Klaus-Peter & Zhang, Chun-Liang & Czaikowski, Oliver & Stührenberg, Dieter & Heemann, Ulrich. (2015). The compaction behaviour of salt backfill as a THM-process. 49-60. 10.1201/b18393-8.

Kruck, O., Crotogino, F., Prelicz, R., Rudolph, T., 2013. Assessment of the potential, the actors and relevant business cases for large scale and seasonal storage of renewable electricity by hydrogen underground storage in Europe.

Kumar, Rajeev. (2015). Overpressure Mechanisms in Deep Drilling in Western Offshore India. 424-424. 10.1190/ice2015-2149843.

Lafuerza, S., Sultan, N., Canals, M., Frigola, J., Berne, S., Gwenael, J., . . . Sierro, F. (2009). Overpressure within upper continental slope sediments from CPTU data, Gulf of Lion, NW Mediterranean Sea. International Journal of Earth Sciences (1437-3254) (Springer), 2009-06 , Vol. 98 , N. 4 , P. 751-768, 98. doi:10.1007/s00531-008-0376-2

Lazar, M., Schattner, U., & Reshef, M. (2012). The great escape: An intra-Messinian gas system in the eastern Mediterranean. Geophysical Research Letters, 39(20). doi:10.1029/2012gl053484

Leroux, E., Rabineau, M., Aslanian, D., Gorini, C., Molliex, S., Bache, F., . . . Suc, J.-P. (2017). High-resolution evolution of terrigenous sediment yields in the Provence Basin during the last 6 Ma: relation with climate and tectonics. Basin Research, 29(3), 305-339. doi:10.1111/bre.12178

Lewis, S., & Holness, M. (1996). Equilibrium halite-H2O dihedral angles: High rock-salt permeability in the shallow crust? Geology, 24(5), 431-434. doi:10.1130/0091-7613(1996)024<0431:ehhoda>2.3.co;2

Liner, C. L., & McGilvery, T. A. M. (2019). The art and science of seismic interpretation. Springer eBooks.

Liu, X., Flemings, P (2009). Dynamic response of oceanic hydrates to sea level drop. Geophysical Research Letters, 36. doi:10.1029/2009GL039821

Lofi, J. (2018). Seismic Atlas of the Messinian Salinity Crisis markers in the Mediterranean Sea - Volume 2. Commission for the Geological Map of the World. Société Géologique de France, t.181, pp.1-72, 2018, Mémoires de la Société Géologique de France.

Lomax, H., Pulliam, T.H., Zingg, D.W., (2001). Fundamentals of Computational Fluid Dynamics. Springer-Verlag, New York.

Lozar, F., Violanti, D., Bernardi, E., Dela Pierre, F., & Natalicchio, M. (2018). Identifying the onset of the Messinian salinity crisis: A reassessment of the biochronostratigraphic tools (Piedmont Basin, NW Italy). Newsletters on Stratigraphy, 51, 11-31. doi:10.1127/nos/2017/0354

Lugli, S., Schreiber, B., & Triberti, B. (1999). Giant polygons in the Realmonte Mine (Agrigento, Sicily); evidence for the desiccation of a Messinian halite basin. Journal of Sedimentary Research, 69, 764-771. doi:10.2110/jsr.69.764

Lugli, S & Manzi, V & Roveri, M & Schreiber, B.. (2015). The deep record of the Messinian salinity crisis: Evidence of a non-desiccated Mediterranean Sea. Palaeogeography, Palaeoclimatology, Palaeoecology. 433. 10.1016/j.palaeo.2015.05.017.

Lugli, S & Manzi, V & Roveri, M & Schreiber, B.. (2010). The Primary Lower Gypsum in the Mediterranean: A new facies interpretation for the first stage of the Messinian Salinity Crisis. Palaeogeography, Palaeoclimatology, Palaeoecology. 297. 83-99. 10.1016/j.palaeo.2010.07.017.

Luo, G., Hudec, M. R., Flemings, P. B., & Nikolinakou, M. A. (2017). Deformation, stress, and pore pressure in an evolving suprasalt basin. Journal of Geophysical Research: Solid Earth, 122(7), 5663-5690. doi:https://doi.org/10.1002/2016JB013779

Luo, X. R., W. L. Dong, J. H. Yang, and W. Yang, 2003, Overpressuring mechanisms in the Yinggehai Basin, South China Sea: AAPG Bulletin, v. 87, p. 629– 645.

Macgregor, Duncan. (2018). Physics and History of Biogenic Gas Systems in the Eastern Mediterranean The Importance of PVT Conditions. 10.13140/RG.2.2.14094.25920.

Madof, A. S., Bertoni, C., & Lofi, J. (2019). Discovery of vast fluvial deposits provides evidence for drawdown during the late Miocene Messinian salinity crisis. Geology, 47(2), 171-174.

Maillard, A., Gaullier, V., Vendeville, B. C., & Odonne, F. (2003). Influence of differential compaction above basement steps on salt tectonics in the Ligurian-Provençal Basin, northwest Mediterranean. Marine and Petroleum Geology, 20(1), 13-27. doi:https://doi.org/10.1016/S0264-8172(03)00022-9

Maillard, A., Jolivet, L., Lofi, J., Thinon, I., Couëffé, R., Canva, A., & Dofal, A. (2020). Transfer zones and associated volcanic province in the eastern Valencia Basin: Evidence for a hot rifted margin? Marine and Petroleum Geology, 119, 104419. doi:https://doi.org/10.1016/j.marpetgeo.2020.104419

Manca, B., Burca, M., Giorgetti, A., Coatanoan, C., Garcia, M. J., & Iona, A. (2004). Physical and biochemical averaged vertical profiles in the Mediterranean regions: an important tool to trace the climatology of water masses and to validate incoming data from operational oceanography. Journal of Marine Systems, 48(1), 83-116. doi:https://doi.org/10.1016/j.jmarsys.2003.11.025

Manzi, V., Gennari, R., Hilgen, F., Krijgsman, W., Lugli, S., Roveri, M., & Sierro, F. (2013). Age refinement of the Messinian salinity crisis onset in the Mediterranean. Terra Nova, 25, 1-8. doi:10.1111/ter.12038

Manzi, V., Gennari, R., Lugli, S., Persico, D., Reghizzi, M., Roveri, M., . . . Gvirtzman, Z. (2018). The onset of the Messinian salinity crisis in the deep Eastern Mediterranean basin. Terra Nova, 30(3), 189-198. doi:10.1111/ter.12325

Mariner, P. E., Gardner, W. P., Hammond, G. E., Sevougian, S. D., and Stein, E. R (2015). Application of generic disposal system models. SAND2015-10037R, Sandia National Laboratories, Albuquerque, NM.

Marín-Moreno, H., Minshull, T. A., & Edwards, R. A. (2013). A disequilibrium compaction model constrained by seismic data and application to overpressure generation in The Eastern Black Sea Basin. Basin Research, 25(3), 331-347. doi:10.1111/bre.12001

Marín-Moreno, H., Minshull, T.A., Edwards, R.A. (2013). Inverse modelling and seismic data constraints on overpressure generation by disequilibrium compaction and aquathermal pressuring: application to the Eastern Black Sea Basin. Geophysical Journal International, 194(2), 814-833. doi:10.1093/gji/ggt147

Mauffret, A., Frizon de Lamotte, D., Lallemant, S., Gorini, C., & Maillard, A. (2004). E–W opening of the Algerian Basin (Western Mediterranean). Terra Nova, 16(5), 257-264. doi:10.1111/j.1365-3121.2004.00559.x

Mavko, G., Mukerji, T., & Dvorkin, J. (2009). The Rock Physics Handbook: Tools for Seismic Analysis of Porous Media (2nd ed.). Cambridge: Cambridge University Press. doi:10.1017/CBO9780511626753

Meilijson, A., Hilgen, F., Sepúlveda, J., Steinberg, J., Fairbank, V., Flecker, R., . . . Makovsky, Y. (2019). Chronology with a pinch of salt: Integrated stratigraphy of Messinian evaporites in the deep Eastern Mediterranean reveals long-lasting halite deposition during Atlantic connectivity. Earth-Science Reviews, 194, 374-398. doi:10.1016/j.earscirev.2019.05.011

Metwally, Y. M., & Sondergeld, C. H. (2011). Measuring low permeabilities of gas-sands and shales using a pressure transmission technique. International Journal of Rock Mechanics and Mining Sciences, 48(7), 1135-1144. doi:https://doi.org/10.1016/j.ijrmms.2011.08.004

Mianaekere, V., & Adam, J. (2020). 'Halo-kinematic' sequence stratigraphic analysis adjacent to salt diapirs in the deepwater contractional province, Liguro-Provençal Basin, Western Mediterranean Sea. Marine and Petroleum Geology, 115, 104258. doi:https://doi.org/10.1016/j.marpetgeo.2020.104258

Milsch, H., Priegnitz, M., & Blöcher, G. (2011). Permeability of gypsum samples dehydrated in air. Geophysical Research Letters, 38(18). doi:10.1029/2011gl048797

Mirwald, P. (2008). Experimental study of the dehydration reactions gypsum-bassanite and bassanite-anhydrite at high pressure: Indication of anomalous behavior of H2O at high pressure in the temperature range of 50-300 degrees C. The Journal of chemical physics. 128. 074502. 10.1063/1.2826321.

Mott MacDonald. (2014). Preesall Underground Gas Storage Facility: Geological Summary Report, 2014. 169 pp.

Mourad, M., Déverchère, J., Graindorge, D., Bracène, R., Badji, R., Ouabadi, A., . . . Bendiab, F. (2014). The transition from Alboran to Algerian basins (Western Mediterranean Sea): Chronostratigraphy, deep crustal structure and tectonic evolution at the rear of a narrow slab rollback system. Journal of Geodynamics, 77. doi:10.1016/j.jog.2014.01.003

Mousouliotis, Angelos & Albanakis, K. & Georgakopoulos, Andreas & Papatheodorou, George & Tripsanas, Efthymios & Medvedev, Benjamin. (2020). Pre-salt clastic systems in the Herodotus Basin, SE Mediterranean Sea. Marine and Petroleum Geology. 122. 104691. 10.1016/j.marpetgeo.2020.104691.

Nader, F. H. (2014). The geology of Lebanon (p. 108). Beaconsfield, Bucks: Scientific Press Ltd.

Needham, D.L., Pettingill, H., Christensen, C.J., Ffrench, J., & Karcz, Z. (2017). The Tamar Giant Gas Field: Opening the Subsalt Miocene Gas Play in the Levant Basin, in R.K Merrill and C.A. Sternbach, eds, Giant Fields of the Decade 2000-2010: AAPG Memoir 113, p. 221-256

Neuzil, C. E. (1994). How permeable are clays and shales?, *Water Resour. Res.*, 30(2), 145–150, doi:10.1029/93WR02930.

Neuzil, C. E. (1995). Abnormal pressures as hydrodynamic phenomena. American Journal of Science, 295(6), 742–786.

Nikolinakou, M. A., Flemings, P. B., & Hudec, M. R. (2014). Modeling stress evolution around a rising salt diapir. Marine and Petroleum Geology, 51, 230-238. doi:10.1016/j.marpetgeo.2013.11.021

North, L., Best, A.I., Sothcott, J., MacGregor, L., 2013. Laboratory determination of the full electrical resistivity tensor of heterogeneous carbonate rocks at elevated pressures. Geophysical Prospecting 61, 458-470, https://doi.org/10.1111/j.1365-2478.2012.01113.x.

North, L.J., Best, A.I., 2014. Anomalous electrical resistivity anisotropy in clean reservoir sandstones. Geophysical Prospecting 62, 1315-1326, http://dx.doi.org/10.1111/1365-2478.12183.

Olivet J.L. (1996). La cinématique de la plaque Ibérie.- Bulletin des Centres de Recherches Exploration-Production elf-aquitaine, Pau, vol. 20, p. 131-195.

Osborne, M.J. and Swarbrick, R.E. (1997). Mechanisms for generating overpressure in sedimentary basins: A reevaluation. AAPG Bulletin, 81, 1023-1041.

Pérez-Asensio, J. N., Aguirre, J., Schmiedl, G., & Civis, J. (2012). Messinian paleoenvironmental evolution in the lower Guadalquivir Basin (SW Spain) based on benthic foraminifera. Palaeogeography, Palaeoclimatology, Palaeoecology, 326-328, 135-151. doi:https://doi.org/10.1016/j.palaeo.2012.02.014

Peter, M. (2008). Experimental study of the dehydration reactions gypsum-bassanite and bassanite-anhydrite at high pressure: Indication of anomalous behavior of H2O at high pressure in the temperature range of 50-300 degrees C. The Journal of chemical physics, 128, 074502. doi:10.1063/1.2826321

Pfeifle, T.W., Hurtado, L.D., 1998. Permeability of natural rock salt from the Waste Isolation Pilot Plant (WIPP) during damage evolution and healing, Conference: 3. North American Rock Mechanics Society conference, Cancun (Mexico), 3-5 Jun 1998

Pierre, C., Rouchy, J. M., & Blanc-Valleron, M. M. (2002). Gas hydrate dissociation in the Lorca Basin (SE Spain) during the Mediterranean Messinian salinity crisis. Sedimentary Geology - SEDIMENT GEOL, 147, 247-252. doi:10.1016/S0037-0738(01)00232-9

Popp, T., Kern, H., 1998. Ultrasonic wave velocities, gas permeability and porosity in natural and granular rock salt. Physics and Chemistry of the Earth 23, 373-378, https://doi.org/10.1016/S0079-1946(98)00040-8.

Popp, T., Kern, H., & Schulze, O. (2001). Evolution of dilatancy and permeability in rock salt during hydrostatic compaction and triaxial deformation. Journal of Geophysical Research: Solid Earth, 106(B3), 4061-4078. doi:10.1029/2000jb900381

Proshlyakov, B. (1960). Reservoir properties of rocks as a function of their depth and lithology: Associated Technical Services, Incorporated.

Revil, A., Pezard, P.A., and de Larouzière, F.D. (1999). Fluid overpressures in western Mediterranean sediments, Sites 974–979. In Zahn, R., Comas, M.C., and Klaus, A. (Eds.), Proc. ODP, Sci. Results, 161: College Station, TX (Ocean Drilling Program), 117–128. doi:10.2973/odp.proc.sr.161.274.1999

Riding, R., Braga, J. C., Martín, J. M., & Sánchez-Almazo, I. M. (1998). Mediterranean Messinian Salinity Crisis: constraints from a coeval marginal basin, Sorbas, southeastern Spain. Marine Geology, 146(1), 1-20. doi:https://doi.org/10.1016/S0025-3227(97)00136-9

Robertson, A. H. F., & Dixon, J. E. (1984). Introduction: aspects of the geological evolution of the Eastern Mediterranean. Geological Society, London, Special Publications, 17(1), 1-74. doi:10.1144/gsl.sp.1984.017.01.02

Robertson, A. H. F. (1998). Mesozoic-Tertiary tectonic evolution of the easternmost Mediterranean area: integration of marine and land evidence.

Robinson, A.H., Callow, B., Böttner, C., Yilo, N., Provenzano, G., Falcon-Suarez, I.H., Marín-Moreno, H., Lichtschlag, A., Bayrakci, G., Gehrmann, R., Parkes, L., Roche, B., Saleem, U., Schramm, B., Waage, M., Lavayssière, A., Li, J., Jedari-Eyvazi, F., Sahoo, S., Deusner, C., Kossel, E., Minshull, T.A., Berndt, C., Bull, J.M., Dean, M., James, R.H., Chapman, M., Best, A.I., Bünz, S., Chen, B., Connelly, D.P., Elger, J., Haeckel, M., Henstock, T.J., Karstens, J., Macdonald, C., Matter, J.M., North, L., Reinardy, B., 2021. Multiscale characterisation of chimneys/pipes: Fluid escape structures within sedimentary basins. International Journal of Greenhouse Gas Control 106, 103245, https://doi.org/10.1016/j.ijggc.2020.103245.

Robinson, A., Spadini, G., Cloetingh, S., & Rudat, J. (1995). Stratigraphic evolution of the Black Sea: inferences from basin modelling. Marine and Petroleum Geology, 12(8), 821-835. doi:https://doi.org/10.1016/0264-8172(95)98850-5

Rouchy, J. M., & Caruso, A. (2006). The Messinian salinity crisis in the Mediterranean basin: A reassessment of the data and an integrated scenario. Sedimentary Geology, 188, 35-67.

Roveri, M., Bassetti, M. A., & Ricci Lucchi, F. (2001). The Mediterranean Messinian salinity crisis: an Apennine foredeep perspective. Sedimentary Geology, 140(3), 201-214. doi:https://doi.org/10.1016/S0037-0738(00)00183-4

Roveri, M., Flecker, R., Krijgsman, W., Lofi. (2014). The Messinian Salinity Crisis: Past and future of a great challenge for marine sciences. Marine Geology, 352, 25-58. doi:10.1016/j.margeo.2014.02.002

Rutqvist, J., 2015. Fractured rock stress-permeability relationships from in situ data and effects of temperature and chemical-mechanical couplings. Geofluids 15, 48-66, https://doi.org/10.1111/gfl.12089.

Ryan, W. B. F., Hsü, K. J., Cita, M. B., Dumitrica, P., Lort, J. M., Maync, W., . . . Wezel, F. C. (1973). Valencia Trough; Site 122. Initial reports of the Deep Sea Drilling Project; covering Leg 13 of the cruises of the Drilling Vessel Glomar Challenger, Lisbon, Portugal to Lisbon, Portugal, August-October 1970, 13, 91.

Ryan, WBF et al. (1973): Sites 133 and 134. *In: Ryan, W.B.F.; Hsu, K.J.; et al., Initial Reports of the Deep Sea Drilling Project, 13, Initial Reports of the Deep Sea Drilling Project, 13, U.S. Government Printing Office*, **XIII**, 465-514, https://doi.org/10.2973/dsdp.proc.13.114.1973

Ryan, W. B. (2008). Modeling the magnitude and timing of evaporative drawdown during the Messinian salinity crisis. Stratigraphy, 5(1), 227-243.

Sawyer, A. H., Flemings, P., Elsworth, D., & Kinoshita, M. (2008). Response of submarine hydrologic monitoring instruments to formation pressure changes: Theory and application to Nankai advanced CORKs. Journal of Geophysical Research: Solid Earth, 113(B1). https://doi.org/10.1029/2007JB005132

Schettino, A., & Turco, E. (2006). Plate kinematics of the Western Mediterranean region during the Oligocene and Early Miocene. Geophysical Journal International, 166(3), 1398-1423. doi:10.1111/j.1365-246X.2006.02997.x

Schofield, D., Lewis, M., Smedley, P., Bloomfield, J.P., Boon, D. (2014). *Illustrative components of the geological environment.* Nottingham, UK, British Geological Survey, 34pp. (CR/14/132N) (Unpublished)

Sclater, J. G., & Christie, P. A. F. (1980). Continental stretching: An explanation of the Post-Mid-Cretaceous subsidence of the central North Sea Basin. Journal of Geophysical Research: Solid Earth, 85(B7), 3711-3739. doi:10.1029/JB085iB07p03711

Setzmann, U., and W. Wagner (1991), A new equation of state and tables of thermodynamic properties for methane covering the range from the melting line to 625 K at pressures up to 100 MPa, J. Phys. Chem. Ref. Data, 20(6), 1061–1155, doi:10.1063/1.555898.

Shapiro, S.A., 2003. Elastic piezosensitivity of porous and fractured rocks. Geophysics 68, 482-486, 10.1190/1.1567215.

Shapiro, S.A., Khizhniak, G.P., Plotnikov, V.V., Niemann, R., Ilyushin, P.Y., Galkin, S.V., 2015. Permeability dependency on stiff and compliant porosities: a model and some experimental examples. Journal of Geophysics and Engineering 12, 376-385, 10.1088/1742-2132/12/3/376.

Stefano, L., Manzi, V., Roveri, M., & Schreiber, B. (2010). The Primary Lower Gypsum in the Mediterranean: A new facies interpretation for the first stage of the Messinian

Salinity Crisis. Palaeogeography, Palaeoclimatology, Palaeoecology, 297, 83-99. doi:10.1016/j.palaeo.2010.07.017

Stoeckl, L., Banks, V., Shekhunova, S., Yakovlev, Y., 2020. The hydrogeological situation after salt-mine collapses at Solotvyno, Ukraine. Journal of Hydrology: Regional Studies 30, 100701, https://doi.org/10.1016/j.ejrh.2020.100701.

Stormont, J. C., Daemen, J. J. K., & Desai, C. S. (1992). Prediction of dilation and permeability changes in rock salt. International Journal for Numerical and Analytical Methods in Geomechanics, 16(8), 545-569. doi:10.1002/nag.1610160802

Stormont, J. C. (1997). Conduct and interpretation of gas permeability measurements in rock salt. International Journal of Rock Mechanics and Mining Sciences, 34(3), 303.e301-303.e311. doi:https://doi.org/10.1016/S1365-1609(97)00250-5

Stormont J. C. (2001). Evaluation of Salt Permeability Tests, SMRI Project No.2000-1-SRMI, prepared by Department of Civil Engineering, University of New Mexico, Alb uquerque, NM, for the Solution Mining Research Institute

Swarbrick, R. (2012). Review of pore-pressure prediction challenges in high-temperature areas. The Leading Edge, 31(11), 1288-1294. doi:10.1190/tle31111288.1

Tarkowski, R., Czapowski, G., 2018. Salt domes in Poland – Potential sites for hydrogen storage in caverns. International Journal of Hydrogen Energy 43, 21414-21427, 10.1016/j.ijhydene.2018.09.212.

The International Association for the Properties of Water and Steam., (Release on the IAPWS Formulation 2008 for the Viscosity of Ordinary Water Substances. The International Association for the Properties of Water and Steam, Germany, Berlin, 2008).

Tingay, M., Hillis, R., Swarbrick, R., Morley, C., & Damit, A. (2009). Origin of overpressure and pore-pressure prediction in the Baram province, Brunei. Aapg Bulletin - AAPG BULL, 93, 51-74. doi:10.1306/08080808016

Topper, R., Flecker, R., Meijer, P., & Wortel, M. (2011). A box model of the Late Miocene Mediterranean Sea: Implications from combined 87Sr/86Sr and salinity data. Paleoceanography, 26. doi:10.1029/2010PA002063

Urai, J., Schmatz, J., Klaver, J. (2019). Over-pressured salt solution mining caverns and leakage mechanisms Phase 1: micro-scale processes (Project KEM-17), MaP – Microstructure and Pores GmbH, Aachen, Germany

Vigil, G., Xu, Z., Steinberg, S., & Israelachvili, J. (1994). Interactions of Silica Surfaces. Journal of Colloid and Interface Science, 165(2), 367-385. https://doi.org/10.1006/jcis.1994.1242

Virtus (2014). VIRTUS – Virtuelles Untertagelabor im Steinsalz. Gesellschaft für Anlagen- und Reaktorsicherheit (GRS) mbH, GRS-354 and appendices, ISBN 978-3-944161-34-1. (available at https://www.grs.de/publikation/grs-354).

Walley, C. D. (1998). Some outstanding issues in the geology of Lebanon and their importance in the tectonic evolution of the Levantine region. Tectonophysics, 298(1), 37-62. doi:https://doi.org/10.1016/S0040-1951(98)00177-2

Wardell, N., Camerlenghi, A., Urgeles, R., Geletti, R., Tinivella, U., Giustiniani, M., & Accettella, D. (2014). Seismic evidence for Messinian salt deformation and fluid circulation on the South Balearic margin (Western Mediterranean). Paper presented at the EGU General Assembly Conference Abstracts. https://ui.adsabs.harvard.edu/abs/2014EGUGA..1611078W

Warren, J. K. (2016). *Evaporites: A Geological Compendium*. 786-812. Springer International Publishing.

Wang, K., Davis, E.E., Van der Kamp, G. Theory for the effects of free gas in subsea formations on tidal pore pressure variations and seafloor displacements. *Journal of Geophysical Research* **103**, doi:10.1029/98JB00952 (1998).

Wang, L., Liu, J., Xu, H., Xu, Y., 2018. Research on Confining Pressure Effect on Mesoscopic Damage of Rock Salt Based on CT Scanning, pp. 254-262.

Weisbrod, N., Alon-Mordish, C., Konen, E., Yechieli, Y., 2012. Dynamic dissolution of halite rock during flow of diluted saline solutions. Geophysical Research Letters 39, n/a-n/a, 10.1029/2012gl051306.

White, M., Wilmot, R.., Crawford, M., Smiht, J., Gibert, A., Evans, D., Hough, E., Field, l., Reay, D., Milodowski, A., McHenry, J., Wolf, J. (2018) UK Halite Deposits – Structure, Stratigraphy, Properties and Post- closure Performance, Galson Science, Contractor Report 1735-1.

Zhang, D., Skoczylas, F., Agostini, F., & Jeannin, L. (2020). Experimental Investigation of Gas Transfer Properties and Stress Coupling Effects of Salt Rocks. Rock Mechanics and Rock Engineering, 53(9), 4015-4029. doi:10.1007/s00603-020-02151-x

Zidane, A., Zechner, E., Huggenberger, P., Younes, A., 2014. Simulation of rock salt dissolution and its impact on land subsidence. Hydrology and Earth System Sciences 18, 2177-2189, 10.5194/hess-18-2177-2014.

Zimmerman, R.W., Somerton, W.H., King, M.S., 1986. Compressibility of porous rocks. Journal of Geophysical Research: Solid Earth 91, 12765-12777, https://doi.org/10.1029/JB091iB12p12765.

Zivar, D., Kumar, S., Foroozesh, J., 2020. Underground hydrogen storage: A comprehensive review. International Journal of Hydrogen Energy, https://doi.org/10.1016/j.ijhydene.2020.08.138

.